Summer 8-12-2014

Vibrational Properties of Quinones in Photosynthetic Reaction Centers

Nan Zhao

VIBRATIONAL PROPERTIES OF QUINONES IN PHOTOSYNTHETIC REACTION CENTERS

by

NAN ZHAO

Under the Direction of Dr. Gary Hastings

ABSTRACT

Fourier transform infrared difference spectroscopy (FTIR DS) is widely used to study the structural details of electron transfer cofactors in photosynthetic protein complexes. In photosynthetic proteins quinones play an important role, functioning as a cofactor in light-driven electron transfer.

In photosystem I (PS I) phylloquinone (PhQ) functions as an intermediary in electron transfer. To investigate the properties of PhQ that occupies the, so called, A_1 binding site in PS I, time-resolved step-scan FTIR DS, with 5μs time resolution at 77K has been used. By replacing PhQ in the A_1 binding site with specifically isotope labeled version, information on the vibrational frequencies associated specifically with the quinone in the binding site were obtained,

which could be compared to the vibrational properties of quinone in solution or quinones in other protein binding sites. To further aid in assessing the origin of bands in the spectra, quantum mechanics /molecular mechanics (QM/MM) ONIOM type calculations were undertaken. ONIOM is an acronym for Our own N-layered Integrated molecular Orbital and molecular Mechanics. We find that the phytyl tail of PhQ does not play an important role in the orientation of PhQ in the A_1 binding site. We also find that PhQ, in both neutral and reduced states, is strongly hydrogen bonded.

To test and verify the applicability of our QM/MM approach, ONIOM calculations were also undertaken for ubiquinone and a variety of other quinones incorporated into the, so called, Q_A binding site in purple bacteria photosynthetic reaction centers. The calculated and experimental spectra agree well, demonstrating the utility and applicability of our ONIOM approach. Hydrogen bonding to the carbonyl groups of quinones in the Q_A binding site was shown to be relatively weak, and it was found that hydrogen bonding to neutral ubiquinone in purple bacterial reaction centers can be considered in purely electrostatic terms, contrary to the widely held belief that the hydrogen bonding amino acids should be treated quantum mechanically.

INDEX WORDS: Photosynthesis, Quinone, Time-resolved step-scan Fourier transform infrared (TRSS FTIR) spectroscopy, Density functional theory (DFT), and Quantum mechanics/Molecular mechanics (QM/MM)

VIBRATIONAL PROPERTIES OF QUINONES IN PHOTOSYNTHETIC REACTION CENTERS

by

NAN ZHAO

A Dissertation Submitted in Partial Fulfillment of the Requirements for the Degree of

Doctor of Philosophy

in the College of Arts and Sciences

Georgia State University

2014

VIBRATIONAL PROPERTIES OF QUINONES IN PHOTOSYNTHETIC REACTION CENTERS

by

NAN ZHAO

Committee Chair: Gary Hastings

Committee: Richard H. Miller

Brain D. Thoms

A.G. Unil Perera

Gennady Cymbalyuk

Murad Sarsour

Electronic Version Approved:

Office of Graduate Studies

College of Arts and Sciences

Georgia State University

August 2014

DEDICATION

Dedicated to my loving parents, Guodong Zhao and Xiaoyun Yin

ACKNOWLEDGEMENTS

I would like to express my sincere appreciation to those who have contributed to this dissertation and supported me during this amazing journey.

First of all, great thanks to my Ph.D. advisors, Dr. Gary Hastings for supporting me during these past seven years. I would never have been able to finish my dissertation without his guidance. Accompanied by his criticism and encouragement, I had a great experience in his lab, not only for my academic career but also for my life. Dr. Hastings led me into the realm of science and taught me how to think and work as a real scientist. He is enthusiastic about research and scrupulous about every detail. The blessing, help and guidance given by him time to time shall carry me a long way in the journey of life on which I am about to embark.

Special thanks to my committee members, Dr. Richard H. Miller, Dr. A.G. Unil Perera, Dr. Murad Sarsour, Dr. Gennady Cymbalyuk, and Dr. Brain D. Thoms for their guidance, support and helpful suggestions.

My gratitude also goes to my lab mates, Dr. Ruili Wang, Dr. Hari Lamichhane, Dr. Sreeja Parameswaran, Dr. Jing Guo, Hiroki Makita, Zeynep Topdemir and Venus Saatchi for their support and help.

I would also like to thank the remarkable teachers at Georgia State University, including, but not limited to, Dr. Nikolaus Dietz, Dr. Steven Manson, Dr. Vadym Apalkov, Dr. Mark Stockman, Dr. Stuart A. Allison and Dr. Markus Germann.

Thanks are also due to numerous others in the Physics and Astronomy community: Peter Walker at Physics Shop, Carola Butler, Keneta Brooks, Felicia Watts, Justin Cantrell and all the staff at the Physics and Astronomy office who helped me with administrative dealings.

I could not finish this work without the technology support from the University Academic Technology Services at Georgia State University.

I would like to acknowledge the Molecular Basis of Disease program at Georgia State University for providing me with a research fellowship over the past four years.

I would also like to thank all my friends for their support and encouragements.

I am grateful to Aunt Jenny for her love and kindness during this arduous time of my life.

Finally, I would like to express my ultimate gratitude to my parents for their unconditional love, support, understanding and patience. Their love provides my inspiration and is my driving force.

TABLE OF CONTENTS

LIST OF ABBREVIATIONS

2MNQ- 2-methyl-1,4-napthoquinone
Ala- Alanine
Amber- Assisted model building with energy refinement
Arg- Arginine
ATP- Adenosine triphosphate
B3LYP- Becke, three-parameter, Lee-Yang-Parr exchange-correlation functional
Bchl- Bacteriochlorophyll
Bpheo- Bacteriopheophytin
Chl- Chlorophyll
DFT- Density functional theory
DMF- Dimethylformamide
DMNQ- 2,3-dimethyl-1,4-naphthoquinone
DDS- Double difference spectrum
DQ- Duroquinone, 2,3,5,6-tetramethyl-1,4-benzoquinone
DS- Difference spectrum
DTGS- Deuterated triglycine sulfate
EE- Electronic embedding
ENDOR- Electron nuclear double resonance
EPR- Electron paramagnetic resonance
ESEEM- Electron spin echo envelope modulation
FTIR- Fourier transform infrared
His- Histidine
Ile- Isoleucine
Glu- Glutamic acid
Leu- Leucine
MCT- Mercury cadmium telluride
ME- Mechanical embedding
Met- Methionine
MM- Molecular mechanics
MPA- Mulliken population analysis
MQ_0- 2,3-dimethoxy-5,6-dimethyl-1,4-benzoquinone
$NADP^+$ - Nicotinamide adenine dinucleotide phosphate
NHE- Normal hydrogen electrode
NMR- Nuclear magnetic resonance
NPA- Natural population analysis
ONIOM- Our own N-layered Integrated molecular Orbital and molecular Mechanics
P*- Excited bacteriochlorophyll dimer
P700- chlorophyll dimer
P700*- Excited chlorophyll dimer
PBRC- Purple bacterial reaction center
PCM- Polarizable continuum model
PDB- Protein data bank
PED- Potential energy distribution
Phe- Phenylalanine

PhQ- Phylloquinone
PQ9- Plastoquinone-9
PS I- Photosystem I
PS II- Photosystem II
Q_A- A side quinone
Q_B- B side quinone
QM- Quantum mechanics
Rb. sphaeroides- Rhodobacter sphaeroides
RC- reaction center
Rp. viridis- Rhodopseudomonas viridis
S6803- Synechocystis sp. PCC 6803
Ser- Serine
THF- Tetrahydrofuran
Trp- Tryptophan
UFF- Universal force field
UQ- Ubiquinone
VK- Vitamin K

LIST OF TABLES

LIST OF FIGURES

1 INTRODUCTION

On average, approximately $1.8x10^{17}$ W of solar radiation strikes the earth's surface [1]. At this level, one can calculate that enough solar energy hits the earth in one hour to satisfy the energy needs of mankind for one year [2]. Solar energy clearly has the potential to satisfy mankind's energy needs. Unfortunately, this clean and abundant energy resource is vastly underutilized, partly because of considerable challenges related to conversion, storage and transmission. The quantum efficiency of light conversion during the initial stages of photosynthesis is close to 100%. Such a high efficiency of transformation without destruction or harmful side effects is achieved by fine turning the properties of pigments bound in large protein complexes.

Ultrafast transient absorption spectroscopy, and electron paramagnetic resonance spectroscopy, as well as infrared (IR) spectroscopy have provided much insight into the interaction between cofactor and protein complexes. Fourier transfer infrared (FTIR) spectroscopy, in particular, in combination with isotope labeling, is an established tool to probe molecular bonding interactions of protein-bound pigment cofactors. However, the rich information obtained from experimental spectra is seldom straightforward. To address this problem, computational methods are undertaken to aid in assignment of bands in IR spectra, and their interpretation in terms of chemical or physical effects. A combination of experiment and computation is a potent approach for a deeper understanding of the spectral behavior associated with pigments in protein complexes and their biochemical reactions.

1.1 Photosynthesis

Photosynthesis is an important biological process in which solar energy is converted into chemical energy. The overall photosynthetic process can be divided into two distinct phases, light and dark reactions. Light reaction occurs in the thylakoid membrane and the organization of thylakoid membrane, is shown in Figure 1.1. For oxygenic photosynthesis organisms, such as plants, algae and cyanobacteria, oxygen is released as a byproduct in photosynthesis. The light reaction of oxygenic photosynthesis process occurs in four steps: (1) solar energy harvesting; (2) light-induced redox reactions; (3) oxidation of water; and (4) ATP synthesis and $NADP^+$ reduction. The first step is light harvesting in which solar energy is efficiently collected and transferred to the reaction center (RC). The second step takes place in the RC. The harvested energy is used to drive charge separation which initiates a series of electron transfer reactions and proton translocations across the membrane. Oxidation of water in the third step is also called oxygen evolution. This reaction can be simply described as the split of water molecules into electrons, protons and oxygen molecules. Oxygen is released into the atmosphere as a byproduct. The generated protons form a proton gradient across the membrane, which is the driving force for ATP synthase in the fourth step. Finally, $NADP^+$ is reduced to NADPH by the ferredoxin-$NADP^+$ oxidoreductase. Both ATP and NADPH are very important for the biosynthesis of carbohydrates and other compounds in the dark reaction.

Unlike oxygenic photosynthesis, light energy is trapped and converted to chemical energy without the production of oxygen in anoxygenic photosynthesis. There are several groups of phototrophic bacteria that undergo anoxygenic photosynthesis including, purple bacteria, green sulfur bacteria and heliobacteria.

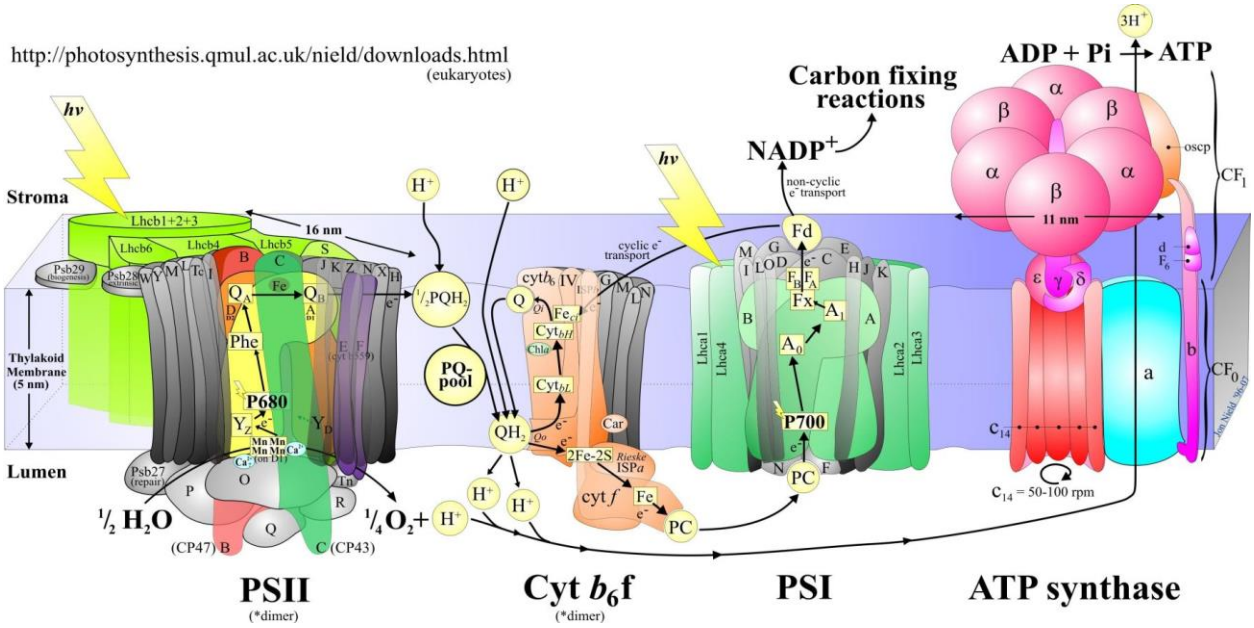

Figure 1.1 Schematic model of the main photosynthetic complexes engaged in oxygenic photosynthesis situated within the higher plant /green algal thylakoid membrane [1].

1.2 Reaction centers of photosystems

In all natural photosynthetic systems, the RC carries out photochemical charge separation and electron transfer. The RCs can be classified into two different types, depending on the nature of terminal electron accepters [3]. Type I RCs contain iron-sulfur clusters as electron acceptors, while type II RCs use quinone as electron acceptors. Photosynthetic organisms may have one or the other of these two RCs. For instance, the green sulfur bacteria, heliobacteria and cyanobacteria have a type I RC. On the other hand, purple bacteria, the green filamentous bacteria, and green-plant have a type II RC.

1.2.1 Structure of photosystem I (PS I) reaction center

For the type I RCs, a crystal structure of thermophilic cyanobacterium *Synechococcus elongatus* PS I at 2.5 Å resolution is available [4]. Isolated cyanobacteria PS I exists as a trimer, which is shown in Figure 1.2a. Each PS I monomer (Figure 1.2b) consists of 12 protein subunits

(PsaA, B, C, D, E, F, I, J, K, L, M and X) and 127 cofactors comprising 96 chlorophylls (Chl), 2 phylloquinones (PhQ), 3 iron-sulfur clusters, 22 carotenoids and 4 lipids.

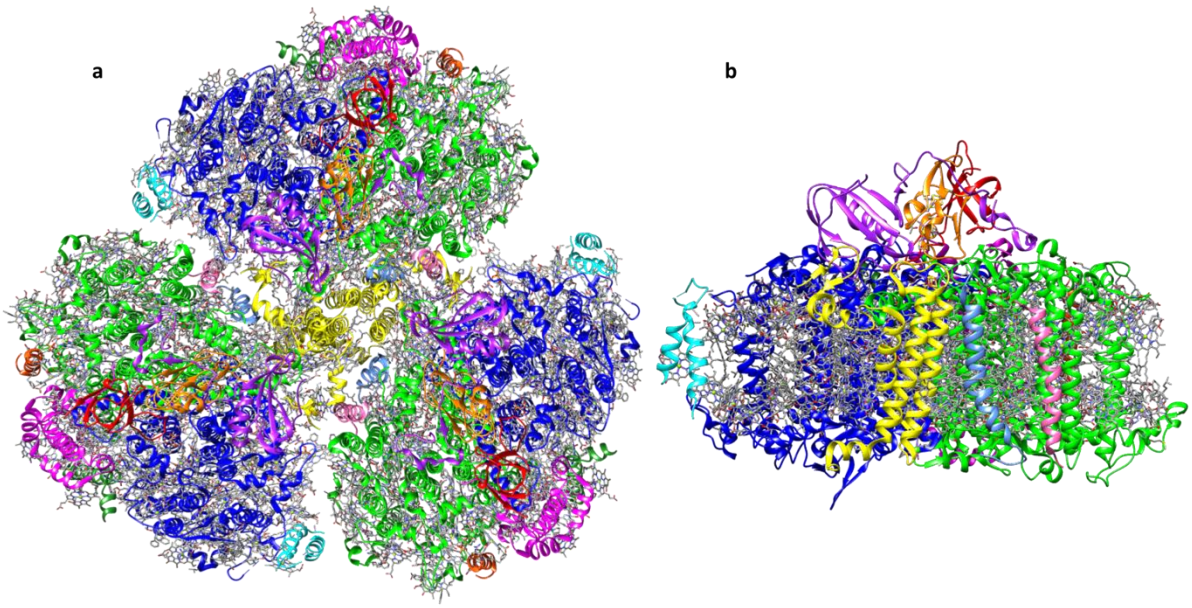

Figure 1.2 Structural model of PS I at 2.5 Å resolution (PDB 1JB0). a. View along the membrane normal form the stromal side. The twelve proteins (PsaA to F, I to M and X) that make up of the PS I complex and the antenna system are shown. b. Side view of the arrangement of all protein in one monomer of PS I (colors as in a).

Subunits PsaA and PsaB are assembled by a pseudo-C_2 axis, and provide ligands for the majority of the electron transfer cofactors. Two iron sulfur clusters, F_A and F_B, which are the terminal electron acceptors, are bound by the subunit PsaC. Subunits PsaD and PsaE stabilize and facilitate the interaction between PsaA/B, PsaC and the electron accepter, which are ferredoxin and flavodoxin [5]. Subunits PsaI, L and M form the contacts between the monomers [6, 7]. Subunits PsaF, J, K and X contribute to the stabilization of the PS I core-antenna system and may also play an important role in forming interactions with the membrane intrinsic peripheral antenna system [8]. In green plants, several additional subunits are not found in cyanobacteria, namely PsaG, H, N and O, and some of these subunits have roles in the docking of light-harvesting complexes [9-12].

Subunits PsaA, B and C, which are related with electron transfer, are shown in Figure 1.3a. The arrangement of the electron transfer cofactors without protein background is shown in Figure 1.3b, and the individual cofactors are labeled with their names.

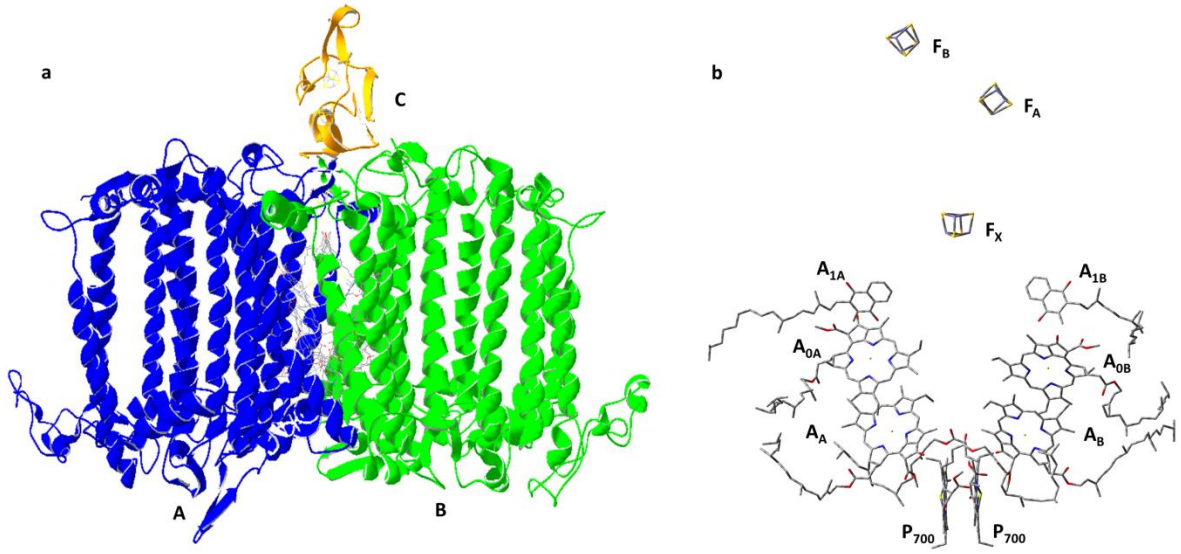

Figure 1.3 Structure of photosynthetic RC from the cyanobacterium *Synechococcus elongatus* (PDB 1JB0)[4]. a. The three-dimensional structure of the RC showing the core subunits and cofactors involved in the electron transfer. b. Arrangement of electron transfer cofactors in PS I without protein background. Subscripts refer to protein subunits PsaA or B to which the cofactors are bound.

1.2.2 Electron transfer pathway in PS I reaction centers

The electron transfer pathway of PS I RCs is formed by six chlorophylls, two phylloquinones and three iron sulfur clusters. The special pair P700 is a dimer of Chls. The remaining cofactors (accessory Chl A_A and A_B; Chl A_{0A} and $A_{0B;}$ PhQ A_{1A} and A_{1B}; iron sulfur clusters F_A and F_B) form two nearly symmetrical branches, which are shown in Figure 1.3b. The inter-cofactor distances are nearly identical in both of the branches. In PS I, both branches of cofactors are involved in the electron transfer [13-15].

Figure 1.4 shows an outline of the light induced electron transfer in PS I. In early studies, the electron transfer across the membrane was considered to begin with the transition of P700 to the excited state P700*. The charge separation occurs between P700* and A_0 with formation of

$P700^+A_0^-$ within 1~3 ps, and the electron is subsequently transferred from A_0^- to A_1 in 30 ps [16, 17]. Forward electron transfer from A_1^- to F_X is characterized by two time constants of 20 ns for A branch and 200 ns for B branch [13, 18]. The fast phase is found to be temperature independent, while the slow phase is decelerated about 100 times at low temperature [19-21].

The charge recombination reactions can be observed when terminal electron acceptors are removed. Typical recombination times are 20-200 ns for $P700^+A_0^-$, 10~250 μs for $P700^+A_1^-$ and about 1 ms for $P700^+F_X^-$, and ~60 ms for $P700^+F_{A/B}^-$ recombination [17].

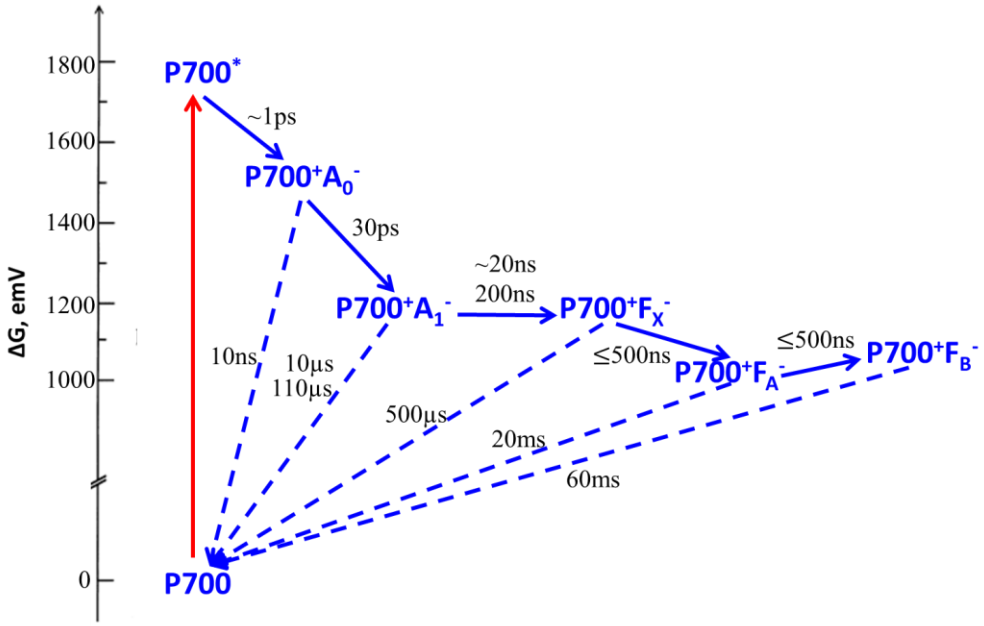

Figure 1.4 Approximation standard free energy levels and kinetics of charge separation in PS I [17]. The stander free energy of the ground state of P700 was arbitrarily set to zero.

According to ultrafast transient absorption spectroscopy[22], the accessory Chl that is located between P700 and A_0 was considered to be the primary electron donor instead of P700 in PS I of cyanobacterium *Chlamydomonas reinhardtii*. The rate constant of the primary charge separation was not affected by mutual arrangements close to P700, while the rate constant of the secondary charge process is changed slightly. However, this hypothesis may be contrary to

recent data obtained by pump-probe femtosecond spectroscopy for PS I [23]. The semi-continuum calculations of PS I cofactors also suggest that accessory Chl as the primary acceptor seems unlikely, because in this case the electron transfer could be thermodynamically unfavorable[24].

1.2.3 Structure of purple bacterial reaction centers

The RCs of purple bacteria are well characterized and have been used to study Photosystem II (PS II) as a structural and functional model. The crystal structure of the purple bacteria RC from *Rhodobacter (Rb.) sphaeroides* has been determined at 2.2 Å resolution [25]. Compared with the PS I RCs, the RC of *Rb. sphaeroides* is much smaller, and includes only three protein subunits (L, H and M), which bind bacteriochlorophylls (BChl), two bacteriopheophytins (BPheo), two ubiquinone molecules, one nonheme iron atom lying between two quinones and one carotenoid. The L and M subunits are nearly symmetrical with respect to the axis perpendicular to the membrane plane. The L and M subunits form the core structure which binds the electron transfer cofactors. The H subunit forms a globular domain that attaches to the L and M subunits. The crystal structure reveals that the cofactors are arranged into two symmetrical branches (A and B). Although the two pigment branches are structurally symmetrical, they are functionally asymmetrical.

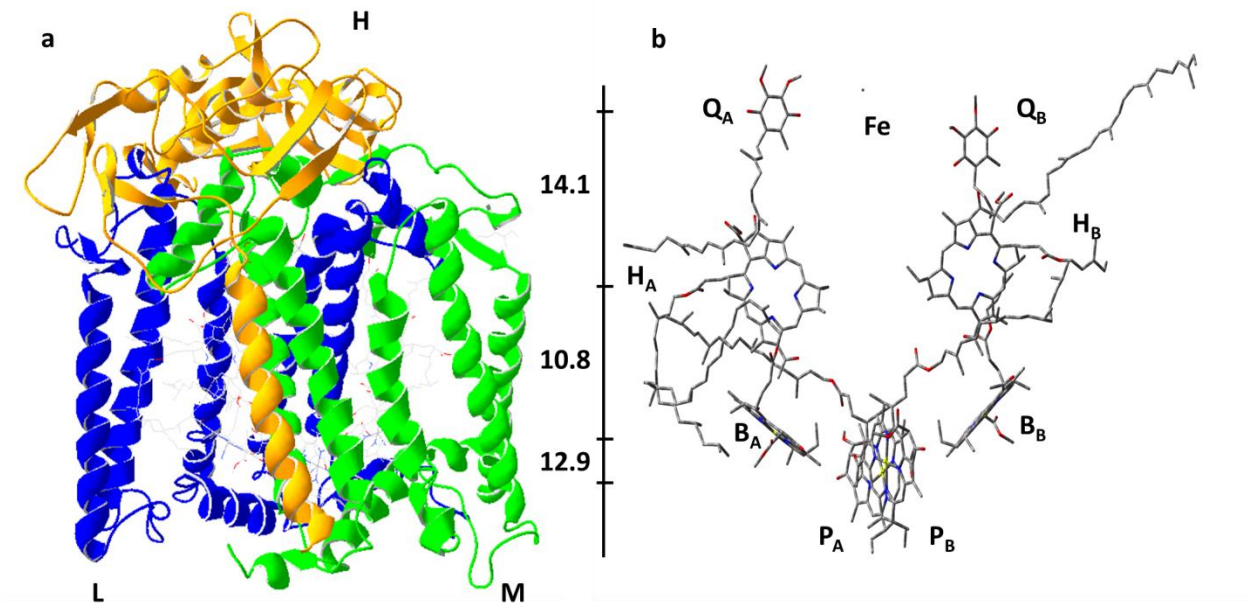

Figure 1.5 Structure of photosynthetic RC of *Rb*. *sphaeroides*. a. The three-dimensional structure of *Rb*. *sphaeroides* RC showing the core subunits and cofactors involved in the electron transfer. The RC of *Rb*. *sphaeroides* consists of three protein subunits (L, M and H). b. Arrangement of electron transfer cofactors in *Rb*. *sphaeroides* without protein background. Distances between cofactors are shown in Å.

1.2.4 Electron transfer pathway in reaction center of purple bacteria

In the RC of *Rb*. *sphaeroides*, electron transfer occurs almost exclusively along the A branch, and B branch only functions in the final electron transfer step. The Electron transfer scheme in the RC of *Rb*. *sphaeroides* is shown in Figure 1.6. As a result of light absorption, electron transfer begins with the transition of a dimer of BChl molecules P to the excited state P*. This exited state P* decays in 3 ps and an electron is transferred to a nearby BChl on the A branch, termed B_A, generating a $P^+B_A^-$ state within the RC [26]. Next, an electron transferred from B_A^- radical anion reduces a nearby BPheo molecule within a single picosecond, generating a $P^+H_A^-$ state [27, 28]. The $P^+H_A^-$ state is relatively long-lived compared to P* and $P^+B_A^-$, lasting~200ps before an electron transferred from the H_A anion to a nearby quinone Q_A [28]. Further electron transfer from the primary quinone Q_A to the secondary quinone Q_B occurs in the time scale of tens of microseconds and slows with decreasing temperature [29]. Subsequently,

the secondary electron transferred from P* leads double reduction of Q_B, converting Q_B from a semiquinone (Q_B^-) to a quinol (Q_B^{2-}). The quinol leaves the RC and is replaced by another quinone from the intramembranous pool [30, 31]. The P^+ state is reduced with either exogenous cytochrome of c-type in *Rb*. *sphaeroides* [32]. The cofactors in the RC of *Rp*. *viridis* are different from those in *Rb*. *sphaeroides. Rp*. *viridis* contains BChla and BPheoa molecules but *Rb*. *sphaeroides* contains BChlb and BPheob molecules. Both Q_A and Q_B in *Rb. sphaeroides* are ubiquinones (UQ), while Q_A in *Rp. viridis* is menaquinone and Q_B is UQ[33].

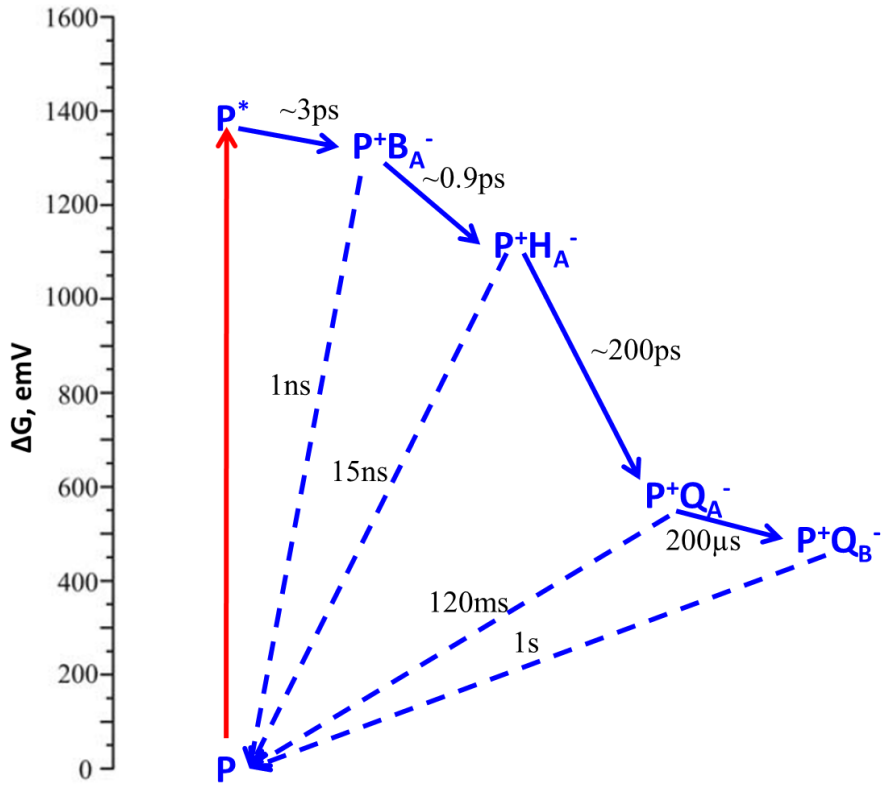

Figure 1.6 Approximation standard free energy levels and kinetics of charge separation in *Rb*. *sphaeroides* [33]

1.3 Function of quinones in electron transfer pathways

Quinones involved in photosynthetic reactions include plastoquinone in PS II; UQ and menaquinone in purple bacteria; and PhQ in PS I. All quinones can undergo one-electron reduction to form a semiquinone species.

Here, we focus on PhQ in PS I and UQ in purple bacteria. In PS I, the secondary electron acceptor is PhQ, which is an analog of naphthoquinone with a phytyl and a methyl substituent. UQ is a substituted benzoquinone with a long side chain. As shown in Figure 1.7, both quinones have a methyl group and an unsaturated hydrophobic tail as ring substituents at adjacent positions between the two C=O groups. However, the interactions between quinones and protein in different systems, such as hydrogen bonding and π stacking, are different. Questions related to how the protein-cofactor interactions control the similar functional properties of the quinone in the two types of RCs are largely unanswered.

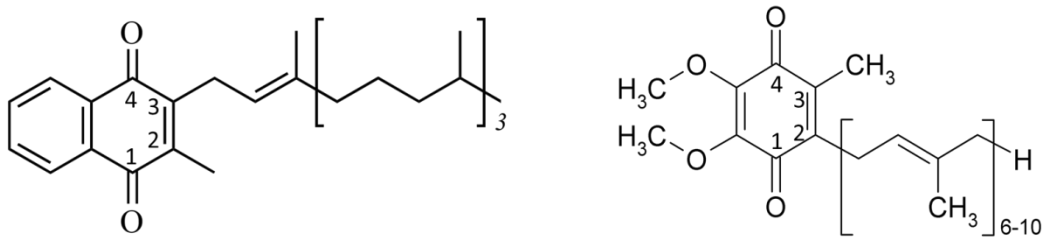

Figure 1.7 Structures and number schemes of PhQ and UQ.

1.3.1 Phylloquinone

As early as 1941, Dam and coworkers discovered PhQ in higher plants. Until 1986, PhQ was identified as an intermediary electron carrier in the acceptor chain of PS I by Malkin [34]. Subsequently, Thurnauer and coworkers used time-resolved electron paramagnetic resonance (EPR) to identify that PhQ acts as the secondary electron acceptor in the PS I electron transfer chain [35]. PhQ in the PS I RC has an unusually low midpoint potential of ~ -800mV [36], which

is ~350 mV more negative than in aprotic solvent [37]. As can been seen in the X-ray structure of the A_{1A} binding site (Figure 1.8), the carbonyl oxygen at C_4 is H bonded to the backbone nitrogen of LeuA722, and the head group of quinone is π-stacked with TrpA697 [4]. The A_{1B} and A_{1A} binding sites are similar. The role of hydrogen bond has been investigated using point mutations to selectively alter residue LeuA722. It has shown that the change in the H bond causes a shift of the quinone midpoint potential, which affects the rate of forward electron transfer [38-40]. The π-π interaction between PhQ and TrpA697 was also monitored by mutagenesis [41, 42]. Partial or total removal the π-stacked Trp residue can change the energy difference between A_1 and F_X to affect the forward electron transfer [43, 44]. Electronic structure calculations of the phyllosemiquinone (PhQ^-) radical in the A_{1A} binding site of PS I indicate that the TrpA697 and PheA689 affect the spin density distribution of PhQ^- [45].

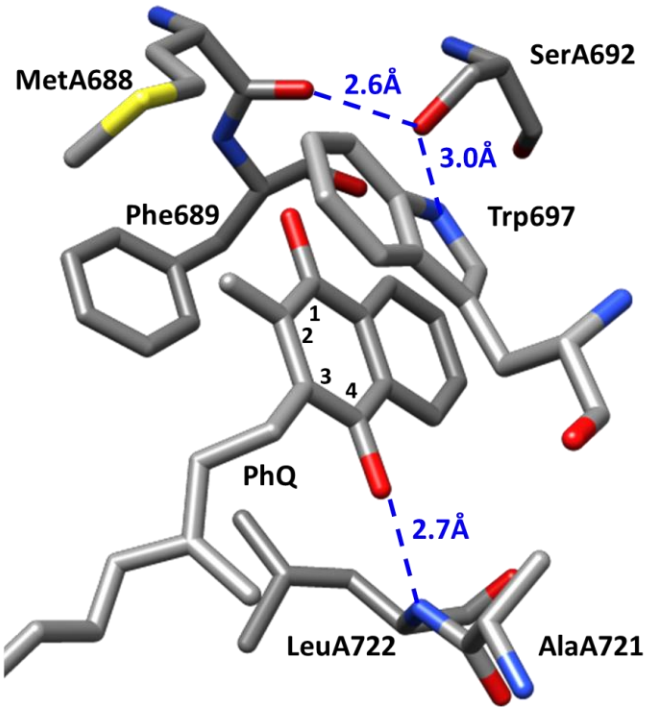

Figure 1.8 The A_{1A} binding site in PS I RC from the 2.5Å X-ray crystal structure of T. *elongatus*. Figure was contracted by using the program Chimera. The H-bonds from MetA688 to SerA692, SerA692 to TrpA697 and from LeuA722 to PhQ are shown and the distances are labeled.

1.3.2 Ubiquinone

In purple bacteria RCs from *Rb*. *sphaeroides* UQ occupies both the Q_A and Q_B binding sites. In spite of this, the functional roles of UQ in both sites are quite different. Q_A is reduced only to semiquinone but Q_B can accept two electrons and can eventually form quinol. Q_A, which has a sufficiently long lifetime, is considered to be the stable primary electron accepter. X-ray crystal structures of the RCs from *Rb*. *sphaeroides* [25] show that C_1=O carbonyl group is hydrogen bonded (H-bonded) to the backbone NH group of AlaM260, while the C_4=O carbonyl group is H bonded to the side chain of HisM219 (Figure 1.9). HisM129 is also a ligand to the nonheme iron, Fe^{2+}. Light induced Q_A^-/Q_A Fourier transform infrared (FTIR) difference spectra obtained for *Rb*. *sphaeroides* with a specifically isotope labeled quinone incorporated into Q_A site suggest that the H bond between C_4=O group and HisM219 is much stronger than the hydrogen bond between C_1=O group and AlaM260 [46, 47]. However, recent ONIOM calculated spectra that agree with FTIR experiments do not predict that one of the carbonyl groups of UQ^- in Q_A site is very strongly H-bonded [48].

EPR studies indicate that hydrogen bonds of Q_A^- are asymmetric and affect the spin density distribution and electronic structure of the quinone radical [49, 50]. However, to study the structure and properties of Q_A^- radicals using EPR, electron nuclear double resonance (ENDOR) or electron spin echo envelop modulation (ESEEM) the ferromagnetic Fe^{2+} ion must be removed and replaced with another bivalent metal such as Zn^{2+}, since the paramagnetic properties of iron strongly cause a large shift and broadening of the EPR spectrum of the acceptor species [51]. All EPR spectra and kinetic properties of Zn-substituted RC are the same as wild type RC [52, 53]. Recent FTIR work in our lab supports this hypothesis.

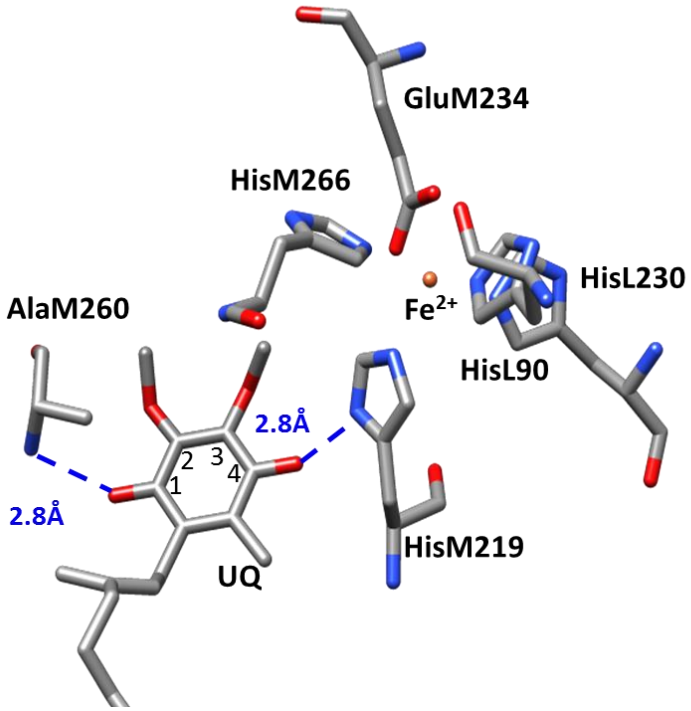

Figure 1.9 The Q_A binding site in purple bacteria RC from the 2.2Å X-ray crystal structure of Rb. *sphaeroides*. Figure was contracted by using the program Chimera. The H-bonds from AlaM260to UQ and from HisM219 to UQ is shown and the distances are also labeled.

1.4 Infrared spectroscopy

IR spectroscopy is a useful method for structure determination of small molecules, as well as large biological systems. IR spectra offer insight into much information, such as chemical structure of the vibrating group, bond and angle parameters, hydrogen bonding and electric field.

1.4.1 Advantages of infrared spectroscopy

In studies of biological systems, IR spectroscopy offers some advantages compared to other techniques. Firstly, IR spectroscopy can be used to determine positions of hydrogen atoms, van der Waals force, H bonding and electrostatic intermolecular interactions which cannot be resolved in crystal structures of biological system. Secondly, samples used for IR spectroscopy may be solid, liquid, powder or polymers. Thirdly, unlike nuclear magnetic resonance (NMR)

spectroscopy, IR spectroscopy can be used to study not only small biomolecules, but also large complex biological system. Fourthly, IR spectroscopy can provide structural data and molecular properties of intermediate species during the protein reaction when difference spectroscopy is used.

1.4.2 Theory of infrared absorption

The physical basis of IR light absorption is very similar to light absorption in the ultraviolet-visible range which causes electronic transitions. The energy differences between two vibrational energy levels are in the order of 0.5 and 0.001eV, corresponding to wavelength range from 2.5μm to 1mm. Molecular vibrational transition can be excited by either the absorption of IR light (IR spectra) or the inelastic scattering of photons (Raman spectra). Vibrations that modulate molecular dipole moment change can be observed in IR spectra, whereas vibrations that modulate polarizability change appear in Raman spectra.

1.4.2.1 Molecular vibration

A molecule of N atoms has total of 3N degrees of freedom, of which three correspond to transitional degrees of freedom and two or three correspond to rotational degrees of freedom. The remaining 3N-6 or 3N-5 degrees of freedom correspond to the vibrations of a non-linear molecule and a linear molecule, respectively, which are so-called normal modes. In each normal mode, all atoms of a molecule are vibrating in phase and have the same frequency. The frequency of this periodic motion is known as vibrational frequency.

Molecules can be considered as an array of point masses that are connected with each other by elastic springs representing the intramolecular interactions between the atoms. For the simplest case of a diatomic molecule, the vibrational frequency $\tilde{\upsilon}$ can be calculated using the equation:

$$\tilde{\upsilon} = \frac{1}{2\pi c}\sqrt{\frac{k}{\mu}}$$

Where $\tilde{\upsilon}$ is the vibrational frequency in wavenumber units; *c* is the speed of light; *k* is force constant; and μ is reduced mass.

The reduced mass is used for simplifying calculations by combining the individual atomic mass. For a diatomic molecule, the reduced mass is defined by:

$$\frac{1}{\mu} = \frac{1}{m_1} + \frac{1}{m_2}$$

Where μ is the reduced mass, and m_1 and m_2 are the masses of the two atoms in the diatomic molecule.

Generally, force constant of bond, mass of atoms and molecular geometry determine vibrational frequencies and relative motion of molecule. Force constants do not only depend on the chemical bonds connecting the individual atoms but also result from the non-bonding intermolecular interactions. With the increasing size of molecules, the normal mode frequencies become more and more complicated. The frequencies as well as IR intensities of vibrations are characteristic of particular bond or group [54].

1.4.2.2 Intensity of vibrational bands

The normal mode associated with a change in dipole moment is active in IR spectra. The IR intensity of active normal mode follows the Beer-Lambert law:

$$\mathrm{A} = \log\left(\frac{I_0}{I}\right) = \varepsilon c l$$

Where A is absorbance; I_0 is the intensity of incident radiation; *I* is the intensity after passing through the sample; ε is the molar extinction coefficient or absorptivity; *c* is the concentration; and *l* is the path length.

The molar extinction coefficient ε of normal mode is related to the change of dipole moment. For a given concentration and path length, the larger the dipole moment change, then the more intense the absorption band will be [55].

1.4.3 Fourier Transform infrared spectroscopy

The Fourier transfer method was introduced to IR spectroscopy in the 1960s, and now FTIR is widely applied in the research. FTIR spectroscopy has several significant advantages over other IR spectroscopy such as high signal to noise ratio, high speed and wavenumber precision.

1.4.3.1 Interferometer and interferogram

The heart of an FTIR spectrometer is a Michelson interferometer shown in Figure 1.10. It consists of a beam splitter and two plane mirrors oriented perpendicularly to each other. One of the mirrors is fixed and the other one is movable. The beam from IR source is divided into two parts by a beam splitter. Half of the incoming beam is reflected by the beam splitter and then reflected by the fixed mirror, while the other half of the incoming beam passes the beam splitter and is reflected by the movable mirror. The beams reflected by two mirrors are recombined via the beam splitter. 50% of the combined beam is reflected towards the detector. The moving mirror produces an optical path difference between the two arms of the interferometer. When the two beams recombine, they interfere constructively or destructively depending on the optical path difference. The helium neon laser is applied to measure the optical path difference and align accessories. The spectral resolution of FTIR spectroscopy is limited by optical path difference.

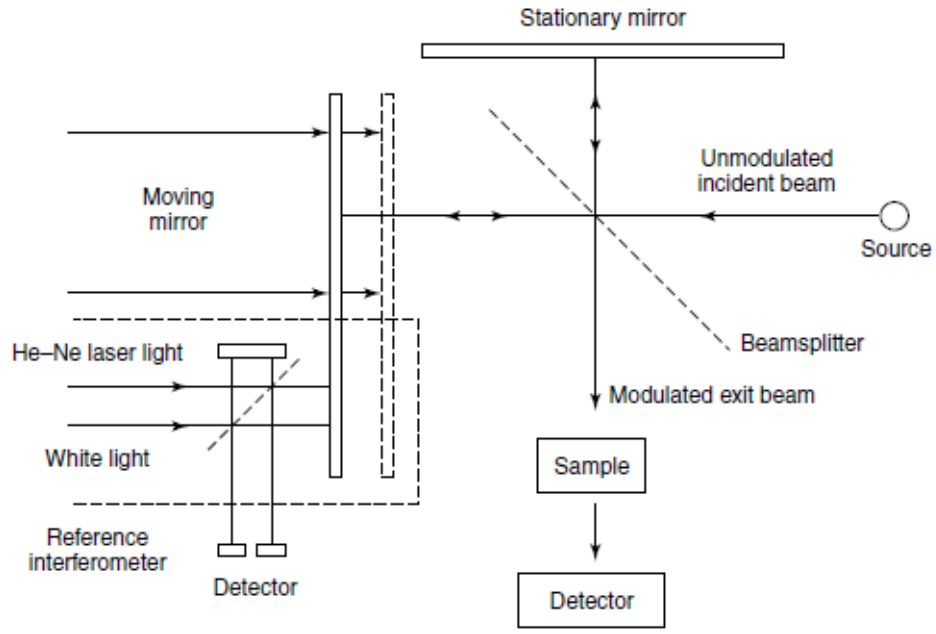

Figure 1.10 Schematic of a Michelson interferometer [56].

A plot of light intensity versus optical path difference is called an interferogram. The resultant interference pattern obtained by IR spectroscopy is shown in Figure 1.11. For polychromatic radiation, the interferogram is a sum of monochromatic waves. The intensity of interferogram falling in the detector, I (δ), is

$$I(\delta) = \int_0^{+\infty} A(\bar{\nu}) \cos(2\pi\bar{\nu}\delta)\, d\bar{\nu}$$

Where δ is the path difference between two beams, $\bar{\nu}$ is the wavenumber, and A is the spectral power density.

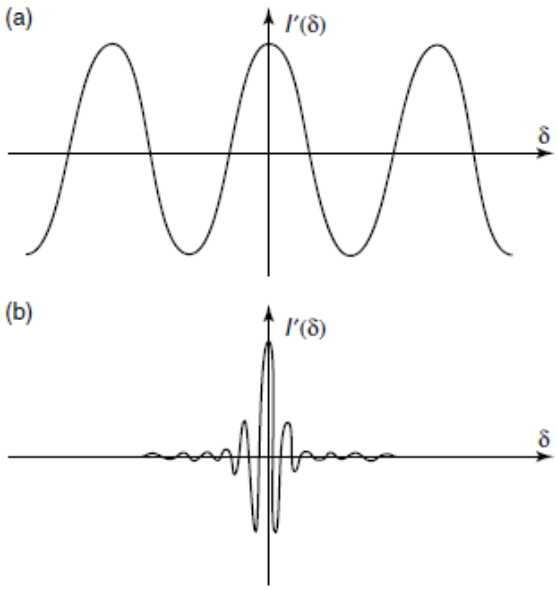

Figure 1.11 Interferograms obtained for (a) source of monochromatic radiation and (b) a source of polychromatic radiation [56].

Fourier transformation mathematic method is applied to transform the digitized information on the interferogram into spectrum. The intensity of light can be represented as a function of wavenumber as follows:

$$A(\bar{\nu}) = \int_{-\infty}^{+\infty} I(\delta)\cos(2\pi\bar{\nu}\delta)\, d\delta$$

$A(\bar{\nu})$ is the intensity of the light detected as a function of wavelength, and is called a single beam spectrum. Figure 1.12 shows a typical single beam spectrum collected on our FTIR spectrometer.

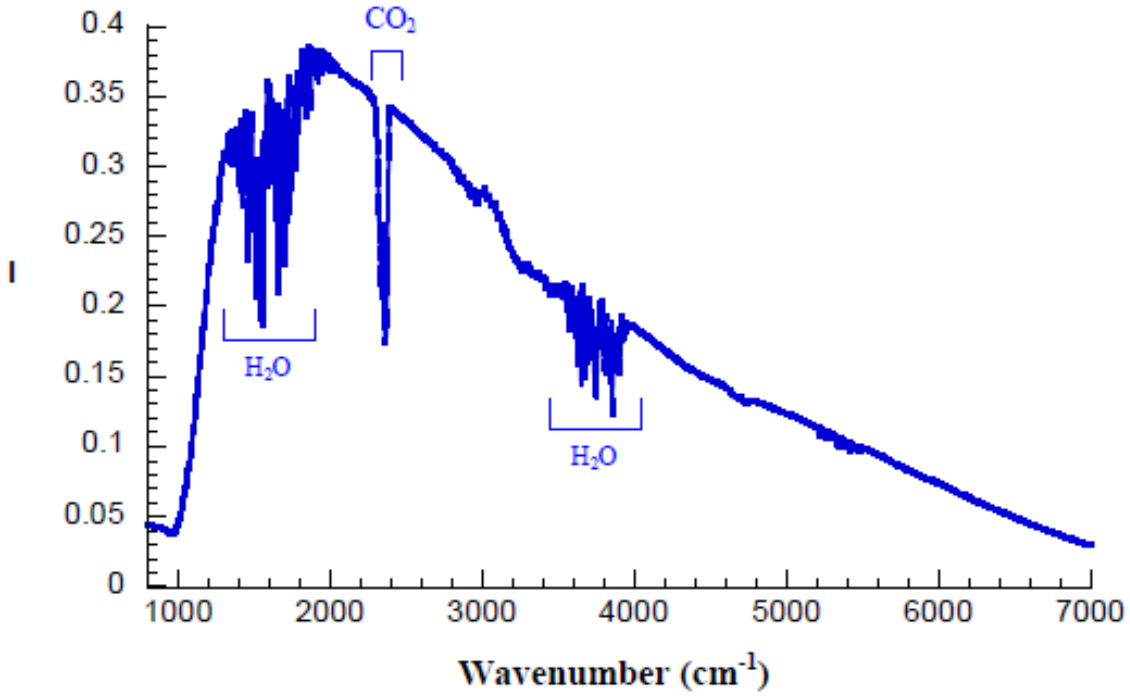

Figure 1.12 A typical single beam spectrum obtained using our FTIR spectrometer. The spectrometer was open to the atmosphere, without purging with nitrogen gas. The single beam spectrum is the Fourier transform of the interferogram. Notice the bands due to water vapor centered near 3600 and 1600 cm^{-1}, and the bands due to CO_2 at ~2400 cm^{-1}[57]

The mathematical process of Fourier transformation assumes infinite boundaries, while in practice the transformation carries out an integration stage over a finite displacement; therefore, apodization is required before Fourier transformation. In addition, phase correction is also required and this correction procedure ensures that the sample intervals are the same on each side of the first interval and should correspond to the path difference of zero [58].

1.4.3.2 Source and Detector

Different measurements require different light sources. Commonly, a high pressure mercury lamp can be used as a light source in the far-IR region. A Globar or Nernst source is used for the mid-IR region, and tungsten halogen lamps are used for the near-IR region.

There are two classes of detectors applied for the mid-IR region: thermal and photo detectors. Pyroelectric detectors such as deuterated triglycine sulfate (DTGS) are thermal detectors which are operated at room temperature in FTIR spectroscopy. The IR radiation absorbed by pyroelectric detector causes an increase in temperature, and induces changes to the surface density. The changes in the surface charge can be detected by the subsequent preamplifier. For more sensitive and faster work, a photon detector such as mercury cadmium telluride (MCT) can be used, but these have to be cooled to liquid nitrogen temperature. The principle of photon detectors is based on change of the conductivity caused by the absorption of IR photon. The increase of conductivity is monitored by the subsequent preamplifier as an increase in current flowing through detectors if a constant voltage is applied [59].

1.4.3.3 Time-resolved step-scan Fourier Transform infrared spectroscopy

In the step-scan technique, the movable mirror is held in a fixed position and the reaction is triggered by a laser flash. At this position, a time-resolved measurement is performed and the time-dependent change of IR intensity after the flash is recorded by the detector. Then the mirror moves to the next position and the time-resolved experiment repeats. After a series of measurements at different mirror positions, the interferogram at each time slice of the time scale can be obtained by combining all the data.

The time resolution of this technique is limited by the response time of the detector and the electronics (amplifier and transient recorder). Step-scan techniques require that the reaction of interest can be repeated many times within the same sample.

1.4.4 Application of infrared spectroscopy on biological system

The size of biological systems studied by IR spectroscopy can vary substantially. The larger size of the biological system, the more complex a spectrum becomes. As the spectrum

becomes more complex, it becomes more difficult to determine which peaks are from which molecules. Figure 1.13 shows an IR absorption spectrum for trimeric PS I particles from *Synechocystis sp. PCC 6803* (*S6803*), and only several broad bands could be observed. Because all the biomolecules in this sample absorb IR radiation, much information is hidden under the broad, featureless absorption bands. The overlapping bands in the absorption spectrum of proteins limit the information that can be obtained from an absorption spectrum. To solve this problem, difference spectroscopy (DS) is required. For example, the light-induced IR DS of photosynthetic RC can be calculated from spectra recorded before and after illumination. The DS only display contributions from those groups undergoing molecular change during the illumination, and all bands that remain unchanged cancel each other out.

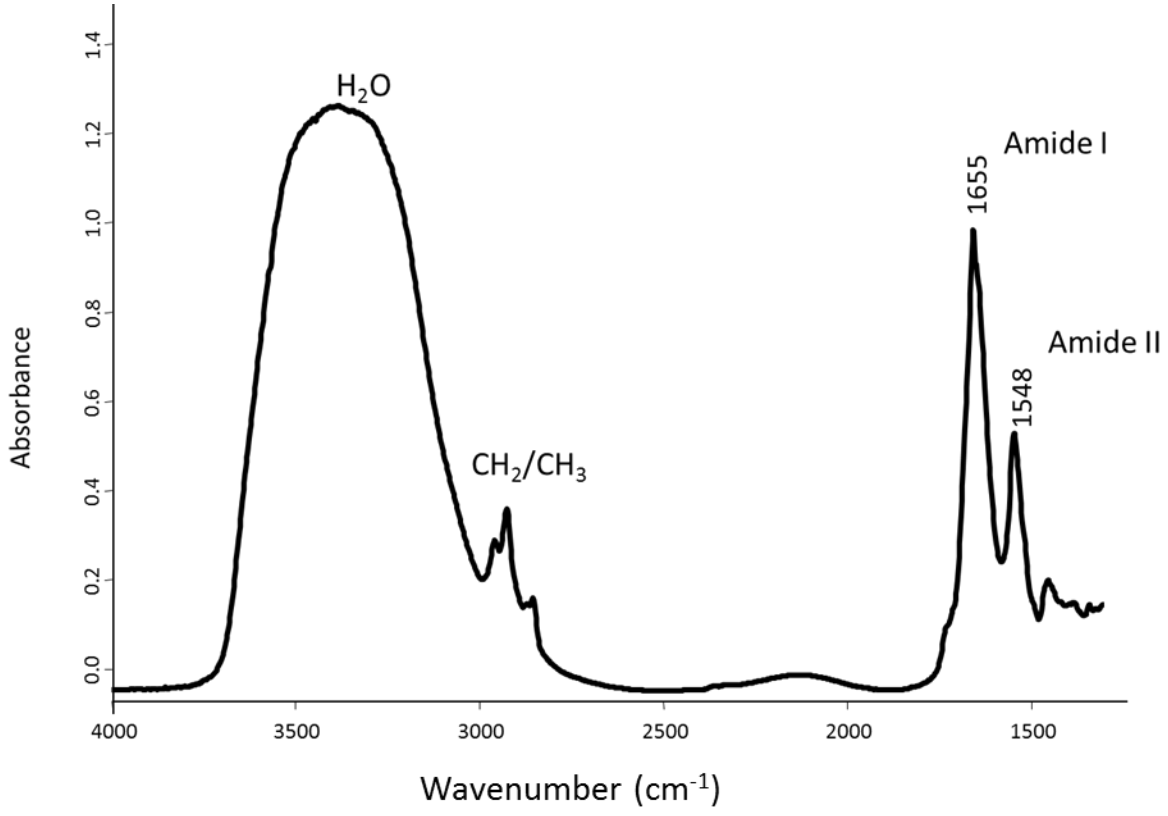

Figure 1.13 IR absorption spectrum of PS I particles from *S6803* in aqueous solution.

Based on DS, site-directed mutagenesis and isotopic labeling of ligands, cofactors and amino acids can be used to assign different signals to individual molecular groups.

Site-directed mutagenesis is a very powerful approach in the studies of biological systems by IR spectroscopy. Due to the interaction between a specific amino acid and target molecule an IR signal is modified when this amino acid has been selectively replaced. Then the modified IR signal should be caused by the interaction between a specific amino acid and target molecule.

Isotopic labeling is also an indispensable tool in IR spectroscopy for assigning bands to specific groups in a large protein. Due to mass effects on vibrational frequencies, IR absorption bands of a labeled group are shifted with respect to those of the unlabeled groups and can be identified in the spectrum. Although isotope labeling can avoid perturbation of the protein structure, the costs of isotope labeling can be very high.

1.5 Computational methods for spectral analysis

Information on molecular structural can be obtained by a variety of spectroscopies techniques. Extraction of information is seldom straightforward. Many effects can alter spectra, and the role of specific effects is not easy to separate and evaluate. To distinguish them from other contributions in the experiments, specific pigments or amino acids should be labeled or mutated without changing other parts.

Computational spectroscopy is a very useful tool for analyzing experimental spectra in terms of chemical or physical effects. The interaction between protein and pigments could be effectively switched on and off computationally in order to analyze their role on the overall observation. A combination of experiments and calculations provide a deeper understanding of the spectral behavior associated with complex biological systems and processes. For instance, H bonding lowers the frequency of stretching vibrations, since it weakens the restoring force [59].

The strength of a H bond is difficult to control in experiments, but in calculations it is could easy to change amino acids to make H bonds stronger or weaker.

ONIOM is an acronym for Our own N-layered Integrated molecular Orbital and molecular Mechanics. ONIOM methods are applied to a large system where two or three layers within the structure that is treated at different levels of accuracy [60, 61]. In a 2-layer ONIOM calculation, the model system which includes active portion is treated with the most accurate method i.e. quantum mechanics (QM), while real system which consists of the entire molecule are treated with inexpensive method, i.e. molecular mechanics (MM). QM is able to describe the changes in the electronic structure of a system undergoing a chemical or biological reaction. However, due to the very demanding computational cost, the application of QM is still limited to a relatively small system. MM has been widely used for large and complex organic and biological systems in molecular dynamics, but is unable to describe bond forming or breaking.

Figure 1.14 illustrates 2-layer ONIOM assignments for modeling the Q_A binding site in *Rb*. *sphaeroides* RCs. In this case, the real system (Figure 1.14c) was defined as 49 amino acids, 7 water and a non-heme iron atom within the UQ-centered spheres of 10 Å radius, and the model system (Figure 1.14d) includes the UQ, AlaM260 and HisM219 which are H-bonded to UQ, a non-heme iron atom and its ligands. The wireframe and ball-and-stick correspond to the real and model system in Figure 1.14b, respectively. The model system is performed using density functional theory (DFT) which is a promising QM method with an excellent compromise between accuracy and computational cost, while the real system is treated with MM for geometry optimization. DFT with B3LYP function is applied to model system because it is widely used for the calculation of vibrational frequencies and found to reproduce experimental data in a satisfactory manner when using a standard 6-31G* basis set [62].

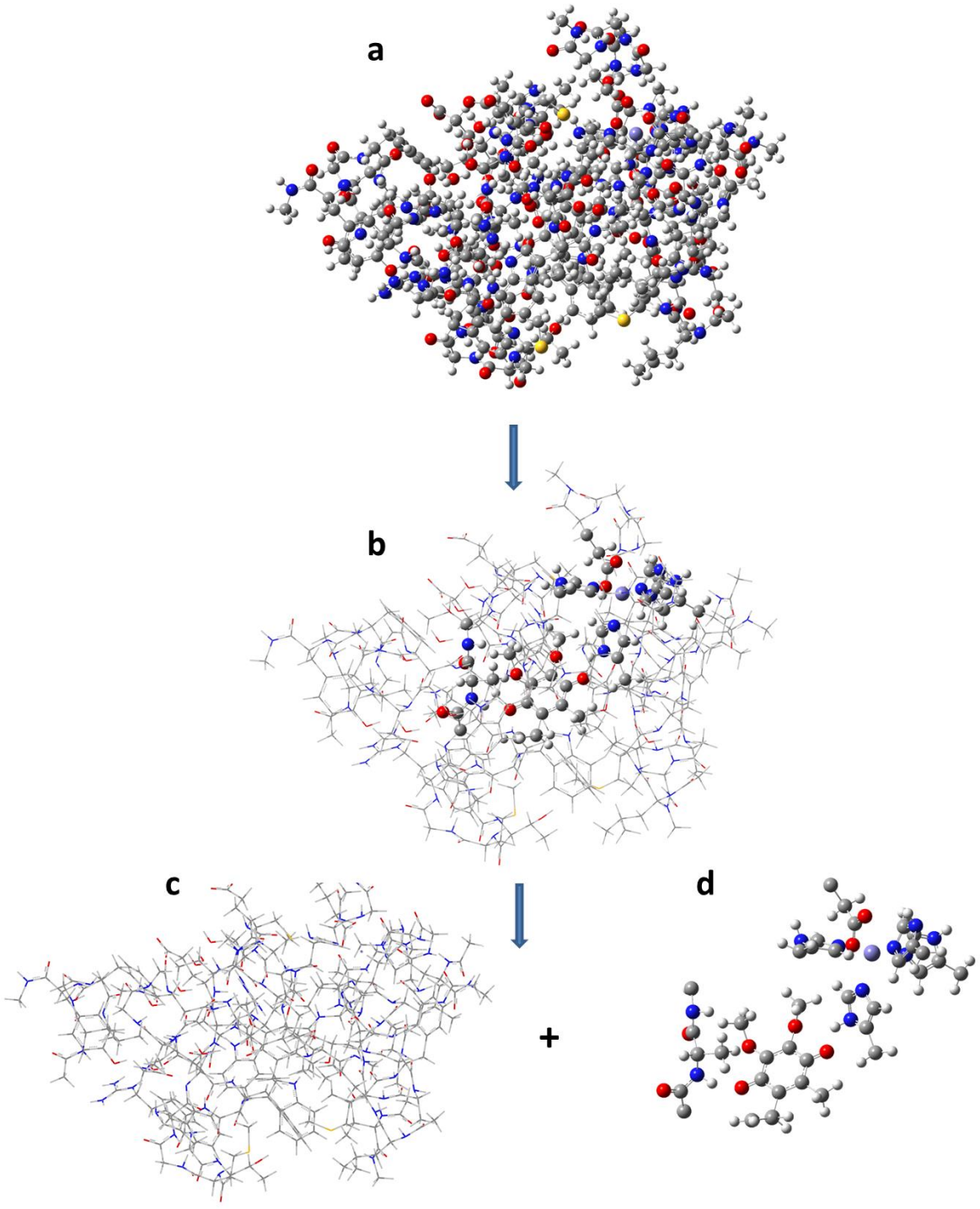

Figure 1.14 ONIOM layer definitions for modeling Q_A binding site in Rb. *sphaeroides* RC. (a) 10Å sphere of Q_A binding site prepared for ONIOM calculation (b) ONIOM model (c) real system (d) model system

1.6 Thesis overview

Chapter 1provided fundamental information on structures and functions of PS I and purple bacteria RCs, with particular attention paid to quinones in photosynthetic RCs. An overview of IR spectroscopy and ONIOM type QM/MM calculations are also described.

In Chapter 2, we present the recent time-resolved step-scan (TRSS) FTIR studies of 2-methyl-1,4-napthoquinone (2MNQ) incorporated into A_1 binding site of PS I particles from *men*B mutants. To further aid in assessing bands in the spectra, DFT based calculation and ONIOM type QM/MM calculations are undertaken. By comparing calculated spectra to the corresponding experimental spectra, the vibrational modes associated specifically with quinone in the binding site are identified. The impact of the phytyl tail on the orientation of PhQ in the A_1 binding site is discussed.

Isotope labeling was used for further band assignments of the A_1^-/A_1 FTIR DS in Chapter 3. We have shown isotope edited TRSS FTIR DS obtained using PS I particles from fully ^{13}C labeled *men*B mutants reconstituted with PhQ and from fully ^{13}C labeled wild type at 77K. DFT based calculations and QM/MM ONIOM type calculations are undertaken to calculate vibrational frequency shifts of PhQ in the A_1 binding site, upon ^{13}C and ^{18}O labeling.

To test and verify the applicability of our QM/MM approach, ONIOM calculations are also undertaken for UQ in purple bacteria photosynthetic RCs. Chapter 4 presents the ONIOM calculations of the vibrational properties of neutral UQ in the Q_A binding site. In these calculations we have treated the hydrogen bonding amino acids either quantum mechanically or molecular mechanically. Isotope edited Q_A^-/Q_A FTIR DS are obtained using different models and methods. The nature of H-bonding to the neutral UQ is discussed. This work has been published recently [63].

In Chapter 5, we use ONIOM methods to calculate isotope edited FTIR DS for RCs with a variety of unlabeled and ^{18}O labeled foreign quinones incorporated into the Q_A binding site. Isotope edited spectra were calculated for RCs with 2,3-dimethoxy-5,6-dimethyl-1,4-benzoquinone, 2,3,5,6-tetramethyl-1,4-benzoquinone, and 2,3-dimethyl-l,4-naphthoquinone incorporated, and compared to corresponding experimental spectra. The normal modes that contribute to the bands in the calculated spectra, their composition, frequency and intensity, and how these quantities are modified upon ^{18}O labeling, are presented. This work has been also published recently [64].

2 TIME-RESOLVED FTIR SPECTROSCOPIC STUDIES OF PHOTOSYSTEM I PARTICLES WITH FOREIGN QUINONES INCORPORATED INTO THE A_1 BINDING SITE

Abstract

Low temperature, time-resolved step-scan FTIR difference spectroscopy (DS) with 5 μs resolution was used to produce A_1^-/A_1 FTIR DS for PS I particles with phylloquinone (PhQ) (2-methyl, 3-phytyl, 1, 4-naphthoquinone) or vitamin K_3 (2-methyl, 1, 4-naphthoquinone (2MNQ)), incorporated into the A_1 binding site.

The time-resolved spectra suggest that 2MNQ and PhQ, in both the neutral and reduced states are similarly hydrogen (H) bonded. To aid in spectral assessment, we have undertaken density functional theory based, ONIOM type QM/MM calculations for PhQ and 2MNQ in the A_1 binding site. The ONIOM calculated spectra agree well with the experimental spectra. Calculations for quinones in the gas phase do not adequately model the experimental spectra. The ONIOM calculations confirm that, both PhQ and 2MNQ, in both the neutral and reduced states, are strongly H-bonded to a backbone NH group of Leu, and the phytyl tail of PhQ has no significantly effect on the orientation of quinone head in the A_1 binding site.

2.1 Introduction

Solar energy is captured and converted in photosynthetic oxygen evolving organisms by two photosystems, referred to photosystem I (PS I) and photosystem II (PS II). The PS I reaction center (RC) consists of 12 or more protein subunits, carrying out photochemical charge separation and electron transport across the thylakoid membrane. The majority of the electron transfer cofactors are located on PsaA and PsaB subunits. These cofactors form two almost

identical branches for electron transfer, which are connected by a pseudo C2 axis and simply called A and B braches (Figure 2.1). Both branches are active in electron transfer [13].

The arrangement of electron transfer cofactors in the PS I complex is depicted in Figure 2.1. The initial light induced charge separation has historically been considered to occur from the excited state of P700 dimeric Chla species). The primary electron acceptor A_0 (a Chla molecule) receives an electron from P700* rapidly, and then transfers it to A_1 within ~30 ps [17]. In PS I, phylloquinone (PhQ) occupies the A_1 binding site [65], the structure of which is shown in Figure 2.3. To further stabilize the charge separated state, the electron is transferred from A_1^- to F_X, and then to F_A/ F_B. F_X, F_A and F_B are iron sulfur clusters [66]. Forward electron transfer from A_1^- to F_X exhibits biphasic kinetics with lifetime of ~200 ns for PhQ^- in the A branch and ~20 ns for PhQ^- in the B branch at room temperature [67]. At 77K, the yield of forward electron transfer to the iron sulfur clusters decreases, and the $P700^+A_1^-$ state forms and recombines with a time constant of 245µs in the cyanobacterial PS I particles [20].

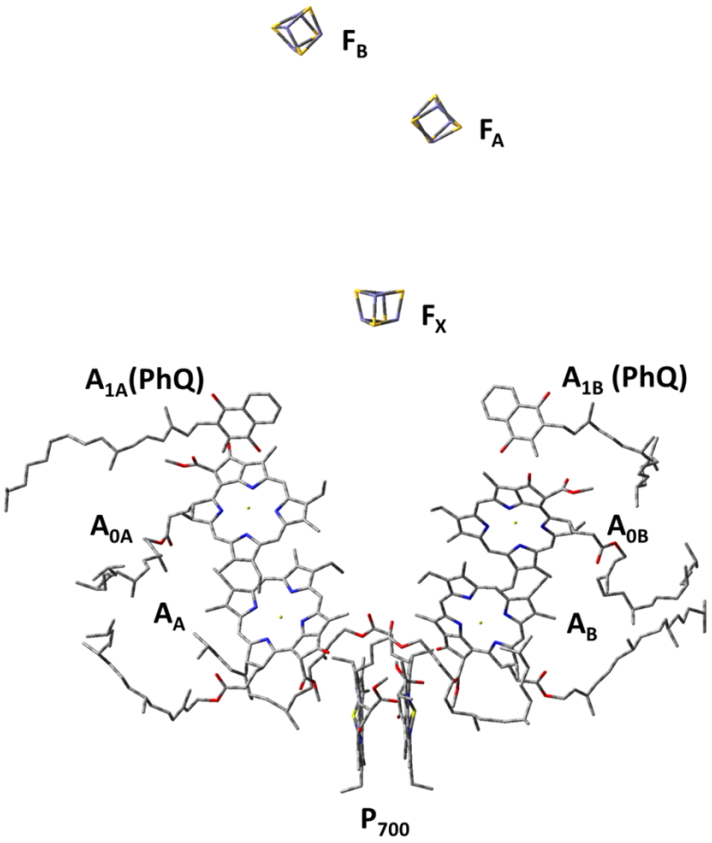

Figure 2.1 Arrangement of the two branches of electron transfer cofactors in PS I. Subscript A refers to protein subunits PsaB, while subscript B refers to protein subunits PsaA. Figure 2.1 is generated using the 2.5 Å X-ray crystal structure of trimeric PS I particles from the cyanobacterium *Synechococcus elongatus* (PDB 1JB0) [4].

The PhQ molecule occupying the A_1 binding site has a midpoint potential closed to -800 mV [68], and this makes it one of the most reducing quinones in biology. This unprecedented redox potential is in part a result of interactions of PhQ with the surrounding protein environment. A detailed view of the A_1 binding pocket is shown in Figure 2.2. The indole ring of TrpA697 (*Synechococcus elongatus* numbering) is π-stacked with the PhQ ring plane. The hydroxyl side chain of SerA692 could be hydrogen (H) bonded to the backbone oxygen atom of MetA688. The indole NH group of TrpA697 may also be H-bonded to the hydroxyl oxygen atom of SerA692. The crystal structure suggests that the C_1=O group of PhQ is not H-bonded, whereas the C_4=O group is H-bonded to the backbone NH group of LeuA722. Electron

paramagnetic resonance **(**EPR) and electron nuclear double resonance (ENDOR) studies on photo-accumulated A_1^- radicals and on spin correlated $P700^+A_1^-$ radical pairs, have shown an asymmetric spin density distribution on the PhQ ring [69-74], indicating a single H-bond to PhQ^- in the A_1 binding site.

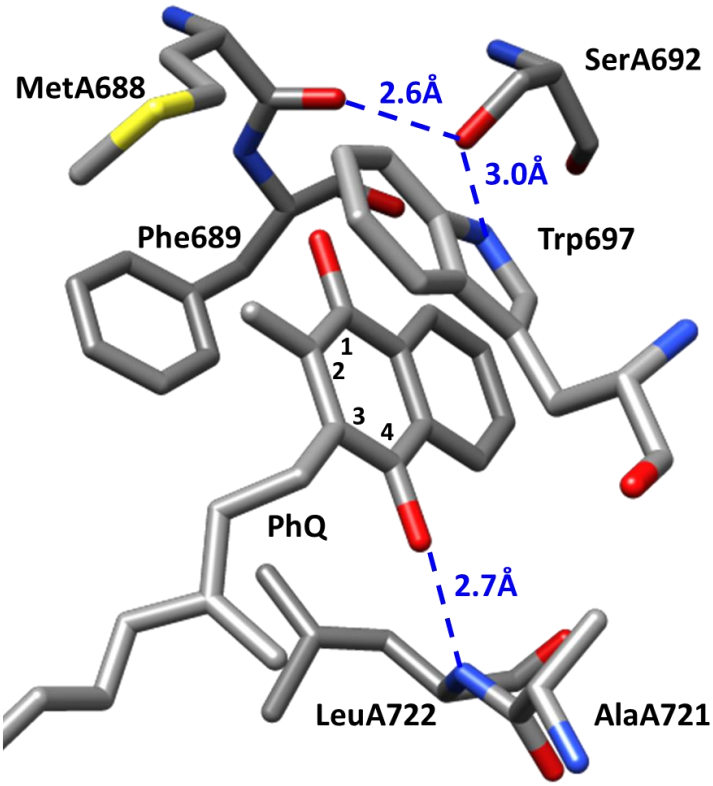

Figure 2.2 View of PhQ in the A_{1A} binding site. Possible H-bonding interactions of the PhQ carbonyl groups with the protein are shown (*dotted*). Nitrogen/oxygen/sulfur/carbon atoms are blue/red/yellow/grey, respectively.

Foreign quinones such as naphthoquinone analogues, anthraquinones, and benzoquinones (BQ) could be incorporated into the A_1 binding site after extraction of native PhQ with organic solvent [75, 76]. The A_1 binding site appears versatile enough to accept a variety of substituted quinones, but only a very limited number of quinones were able to restore forward electron transfer to the iron sulfur clusters. Biggins and his coworkers found that the 3-phytyl or 3-alkyl

tail of naphthoquinone was required to promote electron transfer to F_X though the hydrophobic interaction [75]. However, EPR studies have showed that the saturated alkyl tail of naphthoquinone analogues occupied the position of PhQ methyl group, instead of phytyl chain in the A_1 binding site [77].

Later, genes involved in the biosynthetic pathway of PhQ were identified in *Synechocystis* sp. PCC 6803 (*S6803*) [78]. In *men*B mutant strain of *S6803*, the *men*B gene is inactive and the biosynthetic pathway of PhQ is blocked. In the absence of PhQ, plastoquinone-9 (PQ9) has been shown to occupy the A_1 site, where it functions as an efficient cofactor in electron transfer from A_0 to the iron sulfur clusters [78-80]. PQ9 is a BQ analogue, which is shown in Figure 2.3. Compared to PhQ, the tail of PQ9 is much longer and less saturated, but electron spin echo envelope modulation (ESEEM) experiments have shown that the distance between $P700^+$ and $PQ9^-$ is identical to the distance between $P700^+$ and PhQ^-. In addition, the orientation of $PQ9^-$ head group was found to be the same as PhQ^-, indicating that the phytyl tail of PhQ does not affect the orientation of the quinone in the PS I [81]. On the other hand, EPR studies have shown that 2-methyl-1, 4-naphthoquinone (2MNQ) is positioned and oriented identically to the native PhQ in the A_1 binding site, suggesting that the long tail of PhQ does not play a major role in orienting quinone in PS I [69, 72, 73]. 2MNQ is a PhQ analogue that lacks a phytyl tail (Figure 2.3).

To study molecular properties of quinones in A_1 binding site of PS I, time-resolved step-scan (TRSS) FTIR difference spectroscopy (DS) has been used to produce A_1^-/A_1FTIR DS for PS I particles [82-87]. Density functional theory (DFT) was used to calculate the vibrational properties of PhQ and PhQ^- in the gas phase, and the band assignments for the A_1^-/A_1FTIR DS have been proposed. Moving on from this work, DFT based vibrational frequency calculations

were undertaken for PhQ/PhQ$^-$ with the C_4=O group H-bonded to the backbone NH group of a Leu residue. These calculations predicted that the two C=O modes are separated for PhQ and coupled for PhQ$^-$, suggesting that asymmetric H-bond weakens upon PhQ$^-$ formation [82, 87].

Pulsed EPR and ENDOR techniques applied to PS I suggest that PhQ$^-$ and 2MNQ$^-$ are H-boned to NH group of Leu residue in very similar ways. The length of the asymmetric H-bond was simulated to be 1.64 Å using the point-dipole approximation, which corresponds to a relatively short and strong H-bond [69].

Time-resolved (TR) optical DS and transient EPR spectroscopy show that the replacement of the π-stacked Trp residue with Phe or Ala affects the rate of forward electron transfer from A_1^- to Fx [41, 42] . Theoretical studies also show that hyperfine coupling constants of PhQ$^-$ in the A_{1A} site are sensitive to interactions with neighboring groups, especially TrpA697 and PheA689 [45]. However, in previous studies, only the H-bond between Leu residue and the C_4=O group of quinone was considered in the DFT calculations, and all other quinone-protein interactions were ignored.

Here we describe TR FTIR spectroscopic studies using *men*B PS I particles with PhQ and 2MNQ incorporated into the A_1 binding site. The A_1^-/A_1 FTIR DS obtained using PS I particles with PhQ/2MNQ incorporated were produced, suggesting that PhQ and 2MNQ are H-bonded to NH group of Leu residue in very similar ways. This result indicates that the phytyl tail of PhQ does not affect the H-bond between quinone and NH group of Leu.

We also perform ONIOM type QM/MM calculations on quinone in the A_1 binding site [60, 61]. ONIOM is an acronym for our Own N-layered Integrated molecular Orbital and molecular Mechanics package. In ONIOM calculations, H-bonding and π-stacked interactions for the quinones with protein residues side chains are treated quantum mechanically, and all

other intermolecular interactions are treated molecular mechanically (UFF [88]). Following geometry optimization of quinone in the A_1 binding site using ONIOM methods, the vibrational properties of quinone were calculated using DFT methods. The calculated vibrational modes based on ONIOM methods are very different from that obtained using DFT calculations for only PhQ (or PhQ and Leu residue) in the gas phase.

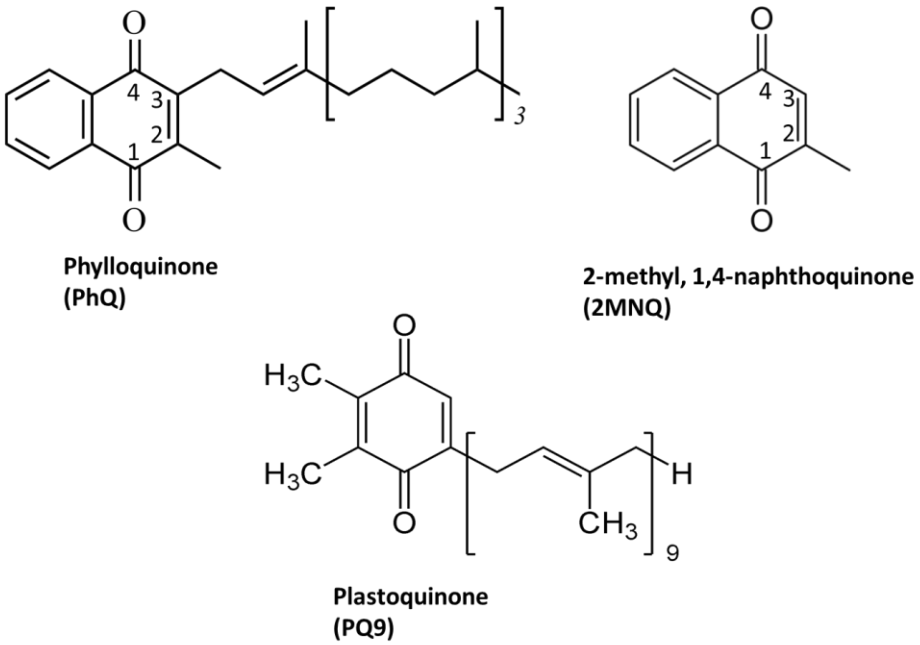

Figure 2.3 Quinone structure and numbering scheme.

2.2 Materials and Methods

2.2.1 Preparation of PS I particles

Trimeric PS I particles were isolated from *menB* mutants following the procedures described previously [78], and stored in 25 mM Tris buffer (pH 8.3) with 0.04% *n*-Dodecyl β-D-Maltoside (β-DM).

2.2.2 Incorporation of quinone into the A_1 binding site

To incorporate quinones into the A_1 binding site, PSI particles are incubated in the presence of a large molar excess of the quinone of interest. Quinones were dissolved in ethanol

and added to a suspension of PS I particles to attain the ratio of ~1000 quinones per RC. This procedure was undertaken in such a way that the volume of ethanol in the mixture never exceeds 2% of the total volume. The PS I particle/quinone mixture was incubated at 4 °C in dark for ~24 hours with stirring.

2.2.3 FTIR absorption spectra of quinones

PhQ and 2MNQ were dissolved in tetrahydrofuran (THF). The thickness of the sample was adjusted using spacers so that the optical density of the main quinone band (at 1662/1666 cm^{-1}) is ~ 0.6. An IR spectrum of pure THF was used to interactively subtract the well-known THF bands present in the quinone/THF spectrum.

2.2.4 Photo-accumulated FTIR difference spectroscopy

Before TR FTIR measurements were undertaken, light-induced $P700^{+}$/P700 FTIR DS were recorded at 77K. PS I particles were washed by 50mM Tris buffer with 0.04% β-DM detergent, then ultra-centrifuged to produce a soft pellet, which was then squeezed between two circular 1 inch diameter CaF_2 windows. The sample thickness (spacing between the two windows) was adjusted so that the peak of the amide I band (at ~1654 cm^{-1}) had an optical density less than 1.0.

For light-induced photo-accumulation measurements, a 20 mW, Helium-neon laser was used for light excitation. The light-dark spectra were constructed as described by previously [89].

2.2.5 Microsecond time-resolved step-scan FTIR difference spectroscopy at 77K

TRSS FTIR experiments with 5 μs time resolution, at 77 K, were undertaken as described previously and $P700^{+}A_1^{-}$/$P700A_1$ FTIR DS were recorded [82]. Data were collected in the 1950-

1100 cm^{-1} region at 4 cm^{-1} spectral resolution. Long pass filters were used to block light above 1950 cm^{-1}, and the CaF_2 windows themselves blocked light below 1100 cm^{-1}.

2.2.6 Estimating the noise level in double difference spectra

TR and photo-accumulated FTIR DS were scaled using a min-max algorithm in which the minimum/maximum y-value was set to 0.0/2.0. For each PS I sample, the TR and photo-accumulated measurements were repeated several times and then averaged, respectively. The standard deviation of the average spectra was taken as the most appropriate measure of experimental variability (noise level).

A_1^-/A_1 FTIR DS were produced by subtracting $P700^+/P700$ FTIR DS from $P700^+A_1^-/P700A_1$ FTIR DS. The error associated with A_1^-/A_1 FTIR DS of PS I particles with PhQ or 2MNQ incorporated into A_1 binding site was calculated using equation (1)

$$\delta f = \sqrt{\delta A^2 + b^2 * \delta B^2} \qquad (1)$$

Where δf is the error associated with A_1^-/A_1 FTIR DS; δA is the standard deviation of the average spectra of $P700^+A_1^-/P700$ A_1 FTIR DS obtained from TR measurements; δB is the standard deviation of the average spectra of $P700^+/P700$ FTIR DS obtained from photo-accumulated measurements; and b is the scaling factor used to normalize the difference bands in $P700^+/P700$ FTIR DS.

The total error for the (2MNQ-PhQ) A_1^-/A_1 FTIR DDS was calculated using the equation (2)

$$\delta f = \sqrt{\delta A^2 + \delta B^2} \qquad (2)$$

Where δf is the total error for the (2MNQ-PhQ) A_1^-/A_1 FTIR DDS; and δA and δB are the error associated with the A_1^-/A_1 FTIR DS obtained from PS I particles with PhQ and 2MNQ incorporated, respectively.

The total error for the (2MNQ-PhQ) A_1^-/A_1 FTIR DDS is shifted and centered on zero before being used to construct error bars, which shows the intensity variation of difference bands over the spectra range.

2.2.7 DFT based vibrational frequency calculations

Models used in DFT calculations were constructed starting from the PS I X-ray crystal structure (PDB entry 1JB0) [4]. The PhQ species in the A_{1A} binding site was used, where the phytyl tail was truncated to a simpler CH_2CHCH_2 unit. Hydrogen atoms were added using Gaussview 4. For DFT calculations the B3LYP functional was used in combination with the 6-31G+ (d) basis set.

In initial DFT calculations two simple molecular models were considered. The first (Model 1) consists only of a PhQ or 2MNQ molecule. Model 1 for PhQ in the gas phase was studied previously [90], and included 28 atoms. The optimized geometry of Model 1 for PhQ in the gas phase is shown in Figure 2.4A.

To account for the asymmetric H-bonding, a second molecular model (Model 2) was considered, and is shown in Figure 2.4B. In Model 2, PhQ and LeuA722 were included, along with part of AlaA721. The side chain of LeuA722 was truncated to a methyl group, while the NH_2 and CH_3 groups of AlaA721 were replaced by hydrogen atoms. For 2MNQ, the tail at C_3 was simply replaced by a hydrogen atom. DFT calculations were undertaken for both neutral and reduced PhQ/2MNQ. The geometry optimized structures (Figure 2.4) were then used as inputs for DFT based vibrational frequency calculations. All calculations were undertaken using Gaussian03 [91].

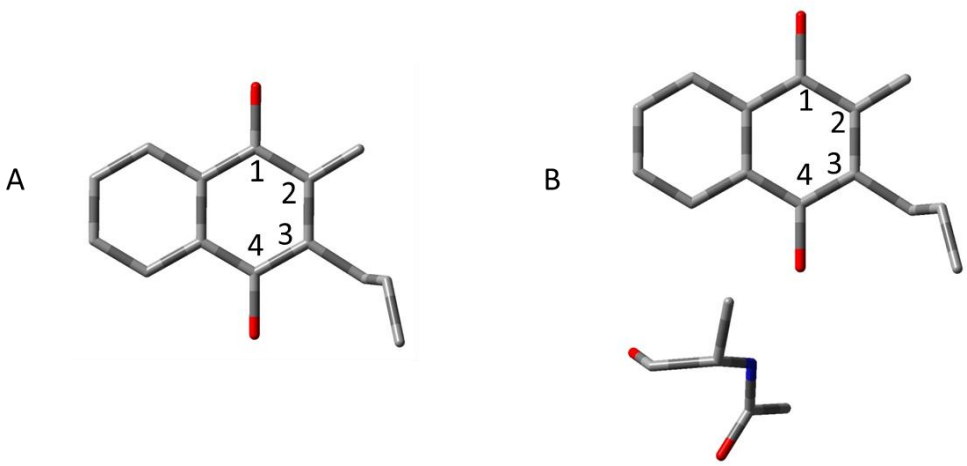

Figure 2.4 Structure of DFT calculation for (A) PhQ and (B) PhQ in the presence of a truncated leucine residue.

2.2.8 ONIOM type QM/MM based vibrational frequency calculations

Models 1 and 2 do not consider the larger protein environment surrounding the quinone of interest. To account for this environment, ONIOM type QM/MM calculations were undertaken. The molecular model used in ONIOM calculations (Model 3) was constructed starting from the PS I crystal structure [4], which consisted of PhQ or 2MNQ, and amino acid residues PheA685-LeuA700 and ArgA720-IleA725. Quinone and important bonding amino acids (LeuA722, TrpA697, PheA689, SerA692, and MetA688) were treated using QM method [DFT using B3LYP/6-31G(d)], and the remaining atoms were treated using MM methods (UFF method [88]).

The phytyl tail of PhQ was again truncated to CH_2CHCH_2. The QM layer of Model 3 is shown in Figure 2.5A. Linking between the QM and MM layers was achieved using the hydrogen link atom approach. Charges for the MM layer were generated using the qEq method, and electrostatic embedding was employed. For geometry optimization of ONIOM calculations all heavy atoms (non-hydrogen atoms) except those of PhQ (or 2MNQ) are constrained. Such a procedure is similar to that used in ONIOM calculations for PhQ EPR parameters [45].

As outlined above, for 2MNQ in the A_1 binding site, the phytyl tail of PhQ at C_3 is replaced by a hydrogen atom. ONIOM calculations were also undertaken for reduced PhQ and 2MNQ by simply specifying the total charge of the QM layer as -1. From a consideration of calculated atomic charge (from Mullikan population analysis) it is found that nearly all of the negative charge is distributed over the atoms of the quinone.

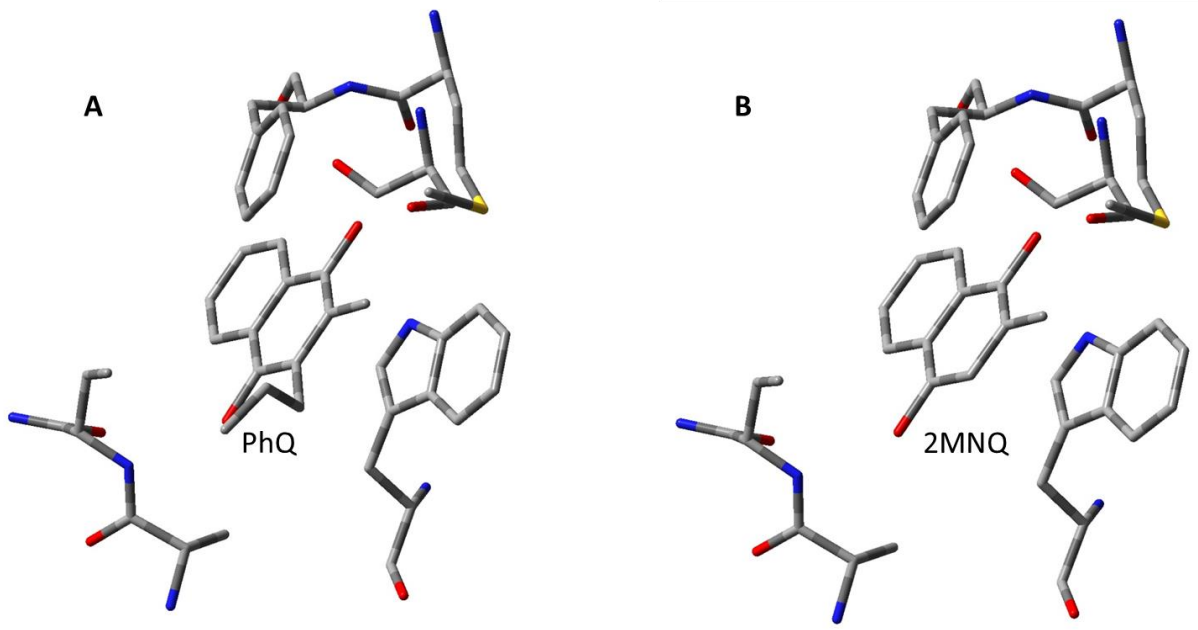

Figure 2.5 QM layer of ONIOM calculations for (A) PhQ and (B) 2MNQ in the A_1 binding site.

Following geometry optimization, linking between the QM and MM layers were replaced by hydrogen atoms. These hydrogen atoms and the entire QM layer were optimized using the B3LYP functional with 6-31G (d) basis set, and all the atoms in the QM layer were fixed except the hydrogen atoms newly added.

After optimizing the hydrogen atoms newly added to QM layer, the entire QM layer was then used in DFT vibrational frequency calculations using the B3LYP functional and the 6-31G (d) basis set. This led to a very large number of vibrational frequencies for the surrounding

amino acids, but these frequencies essentially cancelled when (2MNQ – PhQ) double difference spectra (DDS) were calculated.

Assignment of calculated vibrational frequencies to molecular groups is undertaken by visual identification of the molecular groups that most prominently contribute to the vibration. This visual identification is carried out using GaussView 4, in which the atomic motions associated with each of the vibrational modes can be animated.

2.3 Results and Discussions

2.3.1 Absorption spectra of quinones in tetrahydrofuran

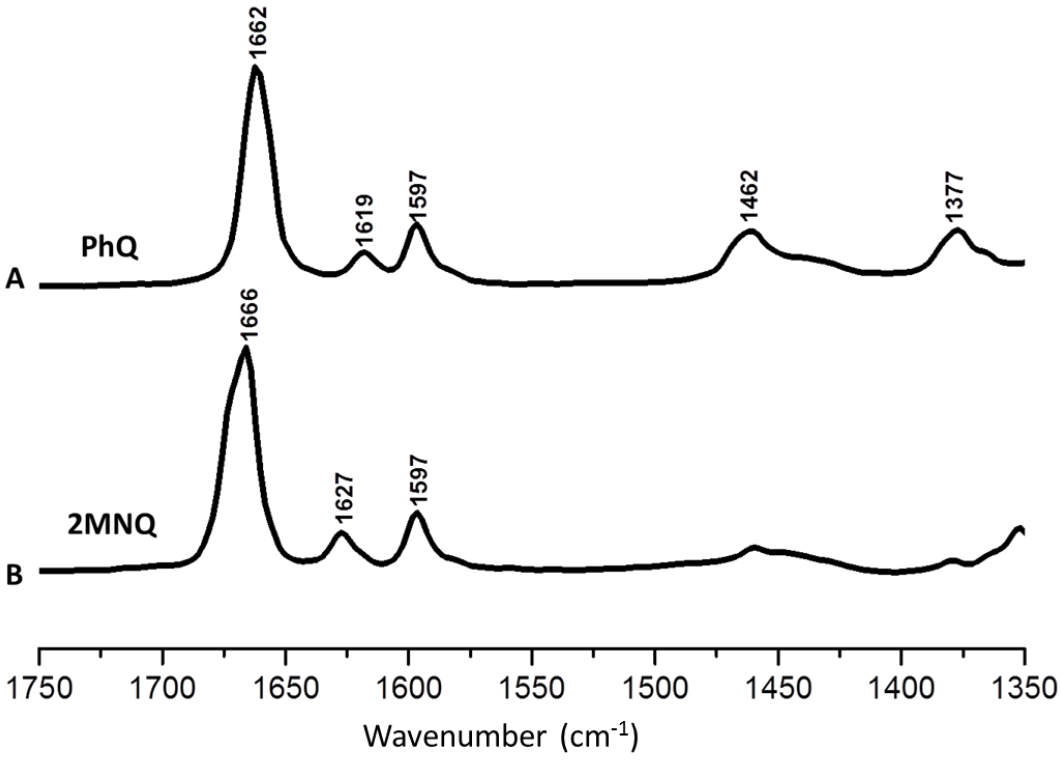

Figure 2.6 FTIR absorption spectra for (A) PhQ and (B) 2MNQ in tetrahydrofuran (THF). The spectra were scaled so that the intensities of the bonds at 1662 and 1666 cm^{-1} are similar.

Figure 2.6 shows FTIR absorption spectra obtained for PhQ and 2MNQ in THF. For PhQ, the bands at 1462 and 1377 cm^{-1} are assigned to δCH_2 and δCH_3 modes of the phytyl chain [90]. In agreement with this prediction, these two bands disappear in the 2MNQ spectrum. A band is observed at 1597 cm^{-1} in both the PhQ and 2MNQ spectra. This band is due to C=C stretching of the aromatic part of the naphthoquinone ring [90].

The band at 1619 cm^{-1} in the PhQ spectrum is due to C=C stretching of the quinonic part of the naphthoquinone ring [90] and upshifts 8 cm^{-1} to 1627 cm^{-1} for 2MNQ. For PhQ, in THF the antisymmetric C=O stretching of both carbonyl groups occurs at 1662 cm^{-1} [90]. Replacement of the phytyl tail at C_3 with a hydrogen atom (2MNQ) leads to a 4 cm^{-1} upshift in frequency of the antisymmetric coupled C=O mode.

2.3.2 Geometry

Key bonding distances and angles obtained from the geometry optimization of Models 1-3 are given in Table 2.1 and Table 2.2, for PhQ and 2MNQ, respectively.

As expected, the C_4=O bond length is calculated to be greater than the C_1=O bond length, when the C_4=O carbonyl group is H-bonded. This is true for both neutral and reduced states of PhQ or 2MNQ.

Compared to PhQ, the H-bond length of PhQ^- is decreased by up to ~0.2Å and 0.19 Å for Model 2 and 3, respectively. The H-bond length between PhQ^- and Leu residue calculated by DFT method in Model 2 is ~1.8 Å, which is longer than the previous studies [69]. In Model 3 the H-bond length between PhQ^- and Leu residue calculated by ONIOM method is just ~1.64 Å, which agrees with the previous ONIOM calculations [45] and simulations using point-dipole approximation [69].

For the ONIOM models (Model 3) of both PhQ and PhQ^-, the C_3-C_4-O-N dihedral angle and the C_4-O-N angle are similar to that found in X-ray crystal structure (Table 2.1). For Model 2, these angles corresponding to PhQ^- are also similar to those found in X-ray crystal structure, suggesting that the orientation of PhQ^- is mainly constrained by the antisymmetric H-bond between Leu residue and PhQ^-. However, for neutral PhQ the C_3-C_4-O-N dihedral angle changed ~304^o in Model 2, compared to X-ray crystal structure, suggesting that the protein environment constrains the orientation of the neutral quinone ring relative to Leu residue. Therefore, the DFT calculations of Model 2 do not accurately describe the geometry of quinone in the A_1 binding site. The geometry optimization of models that contain 2MNQ is very similar to those of models including PhQ.

Table 2.1 Comparison of the geometries of neutral and reduced PhQ in different models

		PhQ			PhQ^-		
PhQ	X-ray [4]	Model 1	Model 2	Model 3	Model 1	Model 2	Model 3
C_1=O	1.416	1.229	1.229	1.226	1.269	1.265	1.263
C_4=O	1.424	1.229	1.234	1.242	1.268	1.279	1.287
Bond length LeuNH-O			2.053	1.834		1.803	1.648
Bond length LeuN-O	2.694		3.069	2.817		2.826	2.658
Angle LeuN-C_4-O	146		155	137		143	134
Dihedral angel LeuN-C_4-O-C_3	143		-161	111		118	115

Table 2.2 Comparison of the geometries of neutral and reduced 2MNQ in different models

	2MNQ			$2MNQ^-$		
2MNQ	Model 1	Model 2	Model 3	Model 1	Model 2	Model 3
C_1=O	1.227	1.227	1.225	1.269	1.265	1.262
C_4=O	1.229	1.235	1.243	1.268	1.279	1.287
Bond length LeuNH-O		2.048	1.810		1.805	1.628
Bond length LeuN-O		3.064	2.800		2.829	2.645
Angle LeuN-C_4-O		159	139		139	135
Dihedral angel LeuN-C_4-O-C_3		-167	112		113	117

2.3.3 Calculated vibrational mode frequencies

The asymmetric H-bonding to the backbone NH group of the Leu has a significant effect on the calculated vibration frequency of the C_4=O carbonyl group. Table 2.3 shows how the vibrational frequencies of PhQ and 2MNQ change on going from the isolated to the H-bonded species. The vibrational frequencies of the H-bonded C_4=O mode of PhQ and 2MNQ, downshift 21 cm^{-1} and 17 cm^{-1}, relative to the C_1=O vibration, in Model 2, respectively. The vibrational frequency of the C_1=O mode is hardly changed by the H-bonding to C_4=O. For calculated spectra of PhQ in Model 1 and 2, the stretching of the C_1=O mode occurs at 1662 cm^{-1}. Replacement of the tail at the 3-position with a hydrogen atom (2MNQ) leads to a 7 cm^{-1} upshift of the C_1=O mode frequency.

In Model 3, the 6-31G (d) basis set was applied to the QM layer to reduce computational cost. The vibrational frequency of C_1=O mode of PhQ occurs 1739 cm^{-1}(unscaled), which is slightly lower than DFT calculation of Model 1 and 2 (1741cm^{-1} unscaled) obtained using the 6-31G (d). The ONIOM calculated spectra of PhQ and 2MNQ are scaled by 0.952 to compare with experiment data. After scaled, vibrational frequencies of the C_1=O mode of PhQ and 2MNQ appear at 1656 and 1663 cm^{-1}, which are similar to the vibrational frequencies for PhQ and 2MNQ in THF (Figure 2.6). In the ONIOM calculations of PhQ, the C_4=O stretching is coupled with the C_2=C_3 stretching. The coupled vibrations occur at 1596 and 1584 cm^{-1}, respectively. The large downshift of the H-bonded C_4=O mode indicates a strong H-bond. In the ONIOM calculations of 2MNQ, the symmetrical and antisymmetrical coupling of C_4=O and C_2=C_3 stretching appear at 1618 and 1589 cm^{-1}, respectively.

Table 2.3 Calculated vibrational frequencies with their assignments for neutral PhQ and 2MNQ. The calculated vibrational frequencies are scaled by 0.965 for Model 1 and 2, and 0.952 for Model 3.

Model 1				Model 2				Model 3			
PhQ	2MNQ			PhQ	2MNQ			PhQ	2MNQ		
1662	1669	-7	$C=O_{as}$	1662	1669	-7	$C_1=O$	1656	1663	-7	$C_1=O$
				1641	1652	-11	$C_4=O$	1596	1618	-22	$C_4=O$, $C_2=C_{3\ s}$
1608	1625	-17	$C_2=C_3$	1608	1622	-14	$C_2=C_3$	1584	1589	-5	$C_4=O$, $C_2=C_{3\ as}$
1583	1583	0	$C=C_a$	1578	1578	0	$C=C_a$				

The subscripts **a** and **q** refer to the aromatic and quinonic part of the naphthoquinone ring; **as** refers to antisymmetric; and **s** refers to symmetric.

Table 2.4 shows the calculated vibrational frequencies for PhQ^- and $2MNQ^-$ obtained using ONIOM calculations. In Model 1, the most intense band appears at 1493 cm^{-1} and is due to the antisymmetric stretching of both C=O groups of PhQ^-, with corresponding mode of $2MNQ^-$ at 1502 cm^{-1}. The band near 1439 cm^{-1} is mainly due to C-C stretching of both aromatic and quinonic rings of PhQ^-, coupling to C-H bending of the aromatic part of the PhQ^- ring. This mode involves very little C-O stretching and downshifts to 1435 cm^{-1} when the phytyl tail of PhQ is replaced by a hydrogen atom.

In the presence of a Leu residue (Model 2), the band at 1495 cm^{-1} is due to the antisymmetric stretching of both C=O groups of PhQ^-, which upshifts 10 cm^{-1} to 1505 cm^{-1} for $2MNQ^-$. Unlike the situation found for neutral quinone, the two C=O modes of PhQ^- or $2MNQ^-$ are coupled. The band at 1433 cm^{-1} is due to the C-C stretching of both aromatic and quinonic rings of PhQ^-, and corresponds to the band at 1438 cm^{-1} of $2MNQ^-$.

In Model 3, the stretching of $C_1=O$ mode of PhQ^- and $2MNQ^-$ occur at 1496 and 1510 cm^{-1}, respectively. The C-H scissoring of the C_2-methyl group occurs at 1469 $cm^{-1}$for PhQ^-, and corresponds to the band at 1477 cm^{-1} for $2MNQ^-$. The band at 1409 cm^{-1} is due to the stretching of $C_4=O$ mode of PhQ^-, coupling with C-C stretching of the aromatic ring of the PhQ^-. The C-H bending of the truncated tail of PhQ^- also contributes to the band at 1409 cm^{-1}. Similarly, the

band at 1418 cm^{-1} is mainly due to the stretching of C_4=O group of $2MNQ^-$, coupling with C-C stretching of the aromatic part of the $2MNQ^-$.

Table 2.4 Calculated vibrational frequencies with their assignments for the PhQ^- and $2MNQ^-$. The calculated vibrational frequencies are scaled by 0.973 for Model 1 and 2, and 0.960 for Model 3.

Model 1				Model 2				Model 3			
PhQ^-	$2MNQ^-$			PhQ^-	$2MNQ^-$			PhQ^-	$2MNQ^-$		
1517	1526	-9	$C=O_s$	1515	1529	-14	$C=O_s$	1496	1510	-14	C_1=O
1493	1502	-9	$C=O_{as}$	1495	1505	-10	$C=O_{as}$	1469	1477	-8	C_4=O,C-C
1439	1435	4	$C=C_a$, $C=C_q$	1477	1482	-5	C-H	1409	1418	-9	C_4=O,C-C
				1433	1438	-5	$C=C_a$, $C=C_q$				

The subscripts **a** and **q** refer to the aromatic and quinonic part of the naphthoquinone ring; **as** refers to asymmetric; and **s** refers to symmetric.

2.3.4 A_1^-/A_1 FTIR difference spectra

Prior to TR measurements, $P700^+$/P700 FTIR DS were first obtained from static photo-accumulation experiments (at 77K). $P700^+A_1^-$/$P700A_1$ FTIR DS were obtained from TR measurements at 77K. $P700^+$/P700 FTIR DS were scaled so that the amplitude of 1716(+)/1698(-) cm^{-1} difference bands were similar. The spectrum that results from the subtraction of $P700^+$/P700 FTIR DS from $P700^+A_1^-$ /$P700A_1$ FTIR DS is named as A_1^- /A_1 FTIR DS.

Figure 2.7 shows FTIR DS obtained at 77 K for *men*B PS I particles with 2MNQ (A) or PhQ (B) incorporated. Spectrum 1 is a TR $P700^+A_1^-$/$P700A_1$ FTIR DS, while spectrum 3 is a static photo-accumulated $P700^+$/P700 FTIR DS. Spectrum 5 is an A_1^-/A_1 FTIR DS that results from subtracting the $P700^+A_1^-$/$P700A_1$ FTIR DS from the $P700^+$/P700 FTIR DS. The standard deviations associated with the average of spectra obtained from TR and static photo-accumulated measurements are spectrum 2 and 4, respectively. Spectrum 6 was calculated using spectrum 2 and 4 with equation 1. The scaled factor, *b*, is 1/1.17 for static photo-accumulated $P700^+$/P700 FTIR DS obtained using PS I particles with 2MNQ/PhQ incorporated. Figure 2.7C displays the result of subtracting the A_1^-/A_1 FTIR DS for PS I with PhQ incorporated from the corresponding

spectrum obtained using PS I with 2MNQ incorporated. This latter spectrum will be referred to a (2MNQ-PhQ) A_1^-/A_1 FTIR DDS. The bands in the (2MNQ-PhQ) A_1^-/A_1 FTIR DDS should be primarily associated with vibrational modes of quinones in the A_1 binding site, with major contributions from protein modes being subtracted. Error bars in Figure 2.7C present an estimate of noise using equation 2. Difference bands at 1663(+)/1656(-), 1504(+)/1494(-), and 1427(+)/1415(-) cm^{-1} are above the noise associated with the (2MNQ-PhQ) A_1^-/A_1 FTIR DS.

The amplitude of a difference band at 1504(+)/1494(-) cm^{-1} is ~$3x10^{-4}$ (in OD units) which is three time bigger than the noise level. The amplitude of a difference band at 1427(+)/1415(-) cm^{-1} is ~$2x10^{-4}$ and the noise level is close to 10^{-5}. The difference band at 1663(+)/1656(-) cm^{-1} is observed in the neutral quinone region, albeit at a slightly lower signal to noise ratio.

By directly subtracting TR $P700^+A_1/P700A_1$ spectra of PS I particles from *men*B mutants with PhQ or 2MNQ incorporated into the A_1 binding site, a (2MNQ-PhQ) FTIR DDS can also be obtained. A comparison of the FTIR DDS obtained using both approaches is shown in Figure 2.8. The DDS obtained by two approaches are somewhat similar. Differences are due to differences in that $P700^+/P700$ FTIR DS obtained using PS I with PhQ or 2MNQ incorporated into the A_1 binding site.

In Figure 2.7C, the 1756(+)/1749(-) cm^{-1} difference band in the A_1^-/A_1 FTIR DS was previously assigned to a 13^3 ester carbonyl group of chlorophyll *a* species, most likely the A_0 chlorophyll *a* molecule that is in close proximity to A_1 [82]. The difference band at 1756cm^{-1}/1749 cm^{-1} appears in the (2MNQ-PhQ) FTIR DDS obtained by both approaches (Figure 2.8), which suggests that the long-range electrostatic interaction between A_0 and A_1 is effected by the phytyl tail of PhQ. The isotope-induced shift of the difference band features at 1674-1677(+) and

1666(-) cm^{-1} indicate that these bands are due to amide I protein vibrations [82]. The observed amide modes in the DDS suggest alteration of the protein backbone (possibly in the vicinity of A_1, but also possibly near P700) upon quinone reduction.

The TRSS FTIR DS for *men*B PS I particles with PhQ or 2MNQ incorporated is similar to that obtained using regular wild-type PS I particles, indicating that PhQ or 2MNQ is incorporated into nearly all of the *men*B PS I RCs [83].

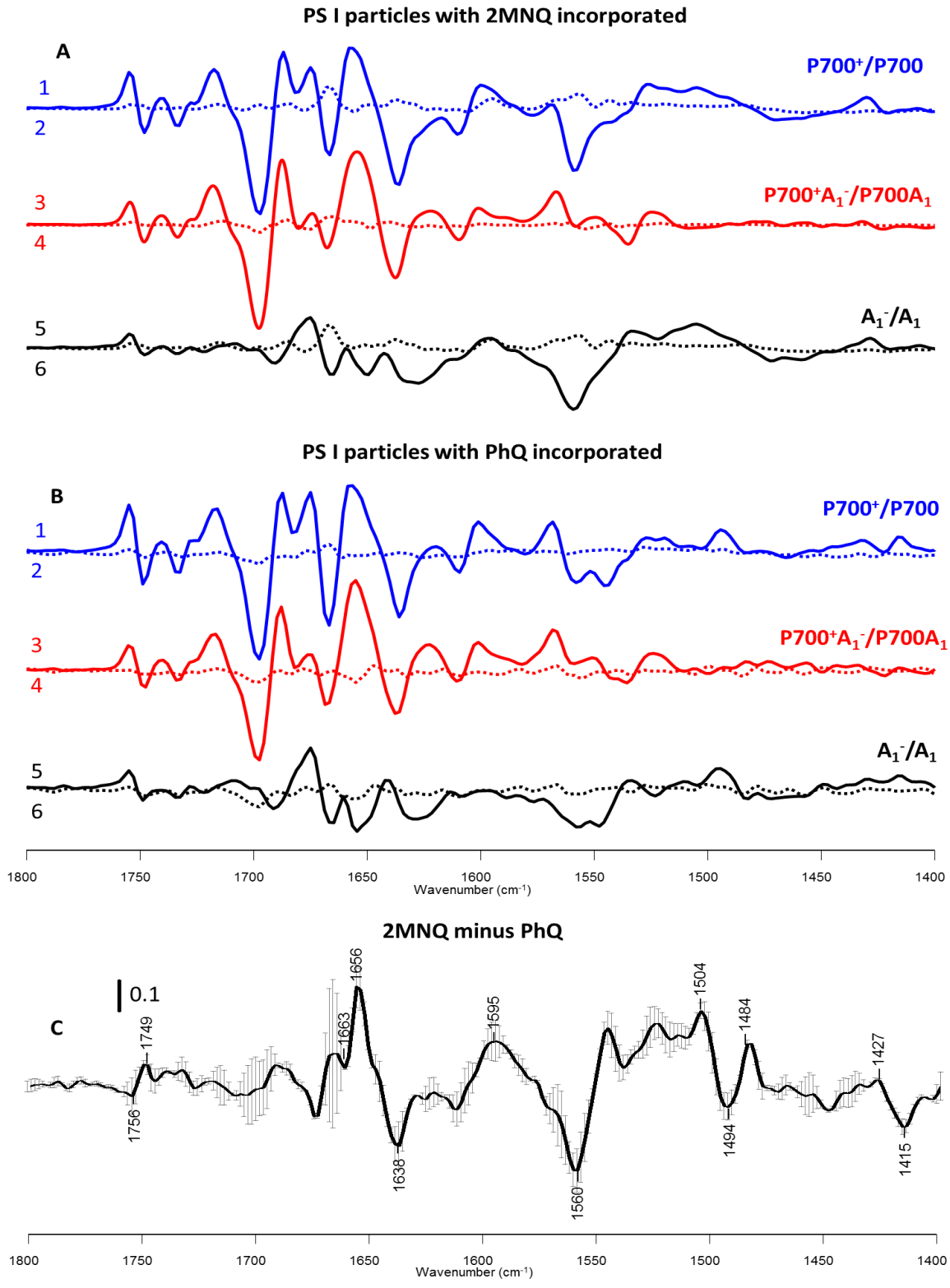
PS I particles with 2MNQ incorporated
A
1
2
P700+/P700
3
4
P700+A1-/P700A1
5
6
A1-/A1
PS I particles with PhQ incorporated
B
1
2
P700+/P700
3
4
P700+A1-/P700A1
5
6
A1-/A1
1800
1750
1700
1650
1600
1550
1500
1450
1400
Wavenumber (cm-1)
2MNQ minus PhQ
C
0.1
1749
1756
1663
1656
1638
1595
1560
1504
1494
1484
1427
1415
1800
1750
1700
1650
1600
1550
1500
1450
1400
Wavenumber (cm-1)

Figure 2.7 $P700^{+}A_1^{-}/P700A_1$ TR FTIR DS (1) and $P700^{+}/P700$ FTIR DS (3) collected at 77 K for *men*B PS I particles with PhQ (A) and 2MNQ (B) incorporated into the A_1 binding site. The spectra shown are the average of 10 (2MNQ) and 11 (PhQ) separated experiments. The standard deviation spectra associated with the static (spectrum 4) and TR experiments (spectrum 2) for 2MNQ (B) and PhQ (A) are shown (*dotted*). These standard deviation spectra give a true measure of the experimental variability (noise level). The spectra have been shifted vertically for clarity. The TR and static spectra were normalized so that the 1718(+)/1697(-) cm^{-1} difference band in both had similar intensity. Also shown in (A) and (B) are so called A_1^{-}/A_1 FTIR DS (5) that result from subtracting spectrum 3 from spectrum 1. The noise level (spectrum 6) associated with the A_1^{-}/A_1 FTIR DS is also shown. Spectrum 6 is obtained by taking the square root of spectrum 2 squared plus spectrum 4 squared. (C) 2MNQ – PhQ FTIR DDS obtained by subtracting spectrum 5 in (A) from spectrum 5 in (B). That is the A_1^{-}/A_1 FTIR DS obtained for PS I particles with PhQ incorporated is subtracted from the A_1^{-}/A_1 FTIR DS obtained for PS I particles with 2MNQ incorporated. The noise level is also shown in (C) (*error bars*), and is obtained by taking the square root of spectrum 6 in (B) squared plus spectrum 6 in (A) squared. The vertical bar in (C) represents an optical density (OD) difference of ~$0.1x10^{-3}$.

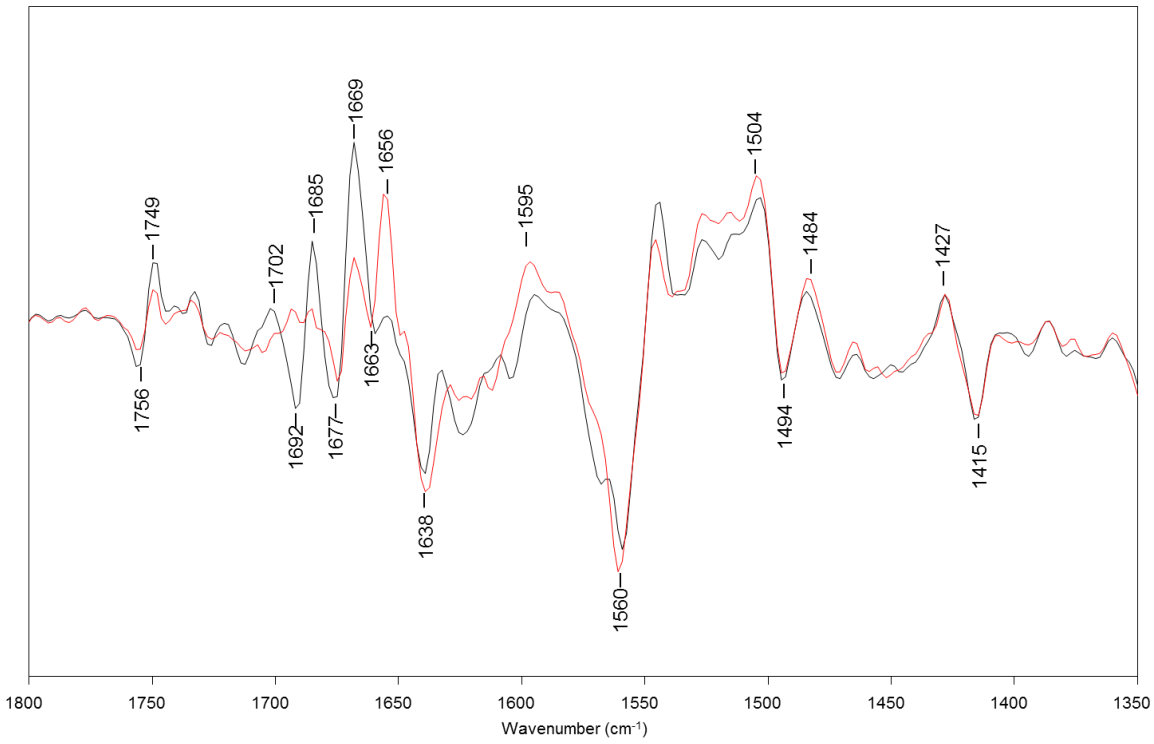

Figure 2.8 Comparison of the (2MNQ-PhQ) FTIR DDS calculated from two approaches. (A) The direct subtraction of $P700^{+}A_1^{-}/P700A_1$ spectra of *men*B PS I particles with 2MNQ or PhQ incorporated, and (B) the subtraction of A_1^{-}/ A_1 FTIR DS for *men*B PS I particles with 2MNQ or PhQ incorporated.

2.3.5 Band assignment for quinone in the A_1 binding site

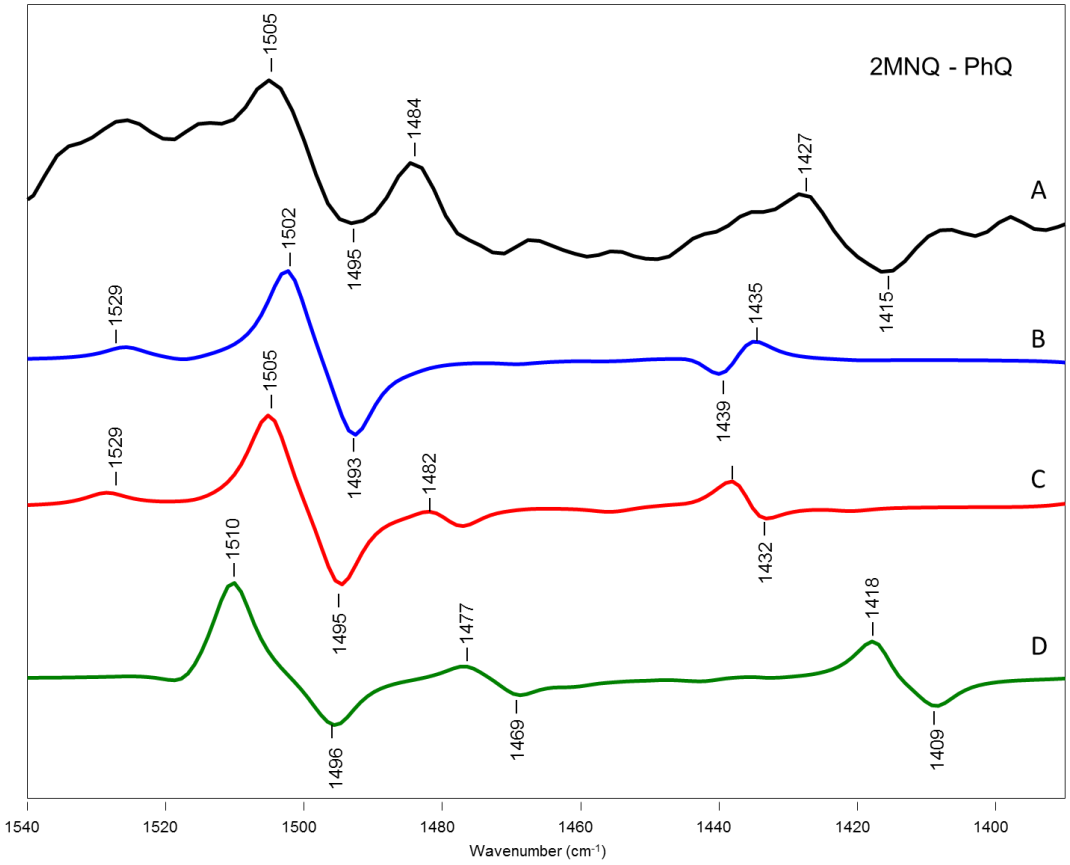

Figure 2.9 Calculated and experimental DS of PhQ^- and $2MNQ^-$ (A) Experimental FTIR DDS obtained by subtracting A_1^-/A_1 spectrum of 2MNQ from that of PhQ (B) Calculated DS of PhQ^- and $2MNQ^-$ in the gas phase by using DFT methods (Model 1); (C) in the presence of a truncated Leu residue by using DFT methods (Model 2); and (D) by using ONIOM method (Model 3). Frequencies in B, C and D were scaled by 0.973/0.973/0.96, respectively.

The calculated and experimental (2MNQ-PhQ) DDS expanded in anion quinone spectral region (1550-1390 cm^{-1}) were compared and shown in Figure 2.9. Figure 2.9A shows the experimental (2MNQ-PhQ) FTIR DDS. Figure 2.9 B shows the calculated (2MNQ-PhQ) DDS obtained using Model 1. Figure 2.9C shows the calculated (2MNQ-PhQ) DDS for Model 2, a PhQ molecule in the presence of a truncated Leu residue. The ONIOM calculated DS (2MNQ-PhQ) DDS is given in Figure 2.9D. In the anion quinone spectra region, bands of $2MNQ^-$ are positive, while bands of PhQ^- are negative.

One prominent observation for the experimental and calculated DDS is the difference band at 1494 (-) /1504(+) cm^{-1}. Isotope edited FTIR DS have suggested that the band at 1494 cm^{-1} in A_1^-/A_1 FTIR DS is due to a C⋯O mode of PhQ^- and downshifts 12 cm^{-1}, 41 $cm^{-1}$and 14 cm^{-1} upon deuteration, ^{13}C and ^{18}O isotope labeling previously [82, 87]. The experimental (2MNQ-PhQ) FTIR DDS suggests that the PhQ^- band at 1494 cm^{-1} upshifts 10 cm^{-1} to 1504 cm^{-1}, upon replacing PhQ with 2MNQ in the A_1 binding site. This result is in good agreement with calculated spectra from Model 1-3. In DFT based vibrational frequency calculations (Model 1 and 2), the band at 1494 cm^{-1} was assigned to antisymmetric stretching of two C⋯O mode of PhQ^-. However, in Model 3, the band at 1494 cm^{-1} is mainly due to the stretching of C_1⋯O mode of PhQ^- and upshifts ~15 cm^{-1} for $2MNQ^-$ when the phytyl tail is replaced by a hydrogen atom.

Another very clear feature in the DDS is the difference band at 1415/1427 cm^{-1}, indicating a band of PhQ^- at 1415 cm^{-1} with the corresponding band of 2MNQ at 1427 cm^{-1}.

In Model 1 and 2, the 1415 cm^{-1} band in A_1^-/A_1 FTIR DS is suggested to be predominantly due to a C-H bending vibrations and weakly coupled to aromatic C-C stretching and antisymmetric C⋯O stretching vibration. The experimental DDS indicates that this mode *upshifts* 12 cm^{-1} to 1427 cm^{-1} for $2MNQ^-$. Upon replacement of the phytyl chain of PhQ^- with a hydrogen, Model 1 suggests that the band at 1415 cm^{-1} *downshifts* 4 cm^{-1}, while Model 2 suggest that the band at 1415 cm^{-1} *upshifts* 7 cm^{-1}. However, the intensity of the difference band at 1439(+)/1432(-) cm^{-1}in the calculated spectrum obtained from Model 2 is too small. In Model 3, the band at 1409 cm^{-1} is mainly assigned to the C_4⋯O mode stretching coupled to C-H bending of the truncated tail of PhQ^- and *upshifts* 9 cm^{-1} for the corresponding mode of $2MNQ^-$ at 1418 cm^{-1}. Therefore, the antisymmetric H-bond should be involved in the model for vibrational frequency calculations, and both intensities and positions of difference bands in the calculated

spectrum from Model 3 are closed to experimental results. In the calculated spectrum from Model 3, the difference band at 1427(+)/1415(-) cm^{-1}, which is due to C_4⎓O mode of reduced quinone, downshifts ~80 cm^{-1} compared to C_1⎓O mode of reduced quinone. The ONIOM calculations suggest that asymmetric H-bond uncouples the two C⎓O modes of PhQ^-.

Another feature in the experimental DDS is the difference band at 1469/1477 cm^{-1}, perhaps indicating a band of PhQ^- at 1469 cm^{-1} with a corresponding band in 2MNQ at 1477 cm^{-1}. The ONIOM calculation (Model 3) suggests the band at 1484 cm^{-1} is due to the stretching of the C_4⎓O group coupling to C-H bending of the methyl group at 2-position, with a corresponding band in $2MNQ^-$ at 1469 cm^{-1}.

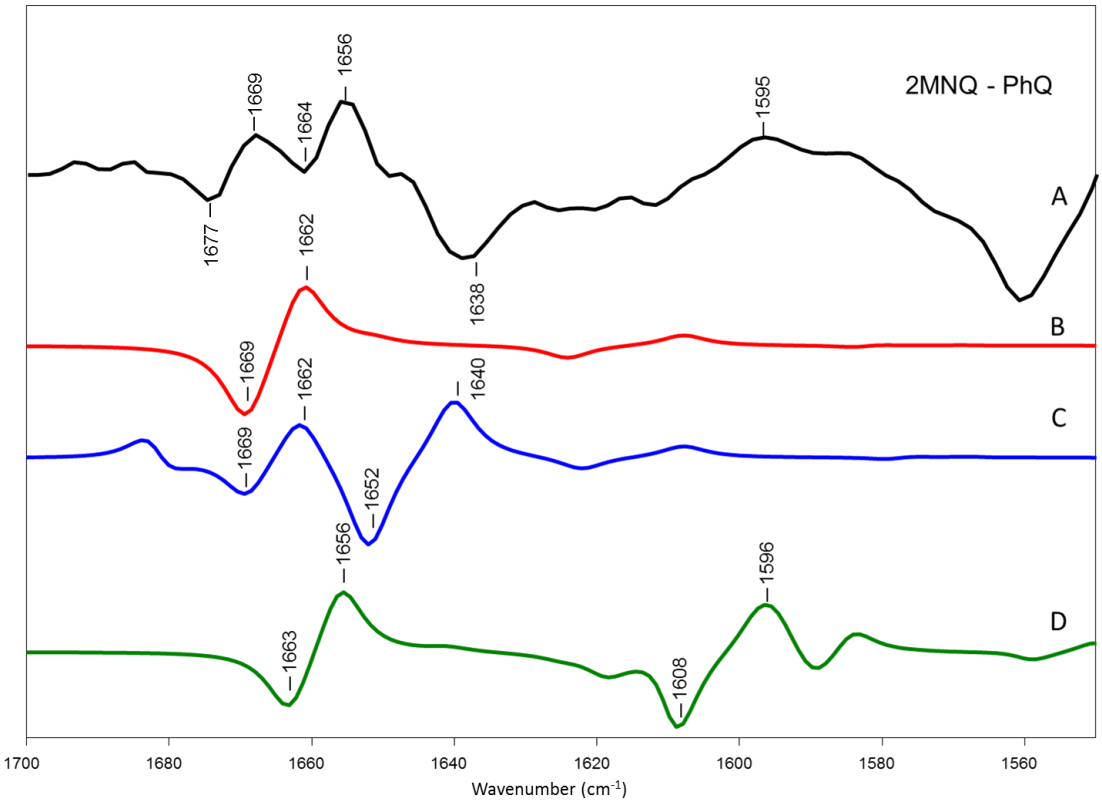

Figure 2.10 Calculated and experimental DS of PhQ and 2MNQ (A) Experimental FTIR DDS obtained by subtracting A_1^-/A_1 spectrum of 2MNQ from that of PhQ (B) Calculated DS of PhQ and 2MNQ in the gas phase by using DFT methods (Model 1); (C) in the presence of a truncated Leu residue by using DFT methods (Model 2); and (D) by using ONIOM method (Model 3). Frequencies in B, C and D were scaled by 0.965/0.965/0.952, respectively.

Experimental (2MNQ-PhQ) DDS in the region of 1700~1550 cm^{-1} is shown in the Figure 2.10. Calculated DS relative to experiments with different models are also shown in Figure 2.10. Figure 2.10 B shows the DS of PhQ and 2MNQ in gas phase by using DFT methods. Figure 2.10C shows the calculated DS of PhQ and 2MNQ in the presence of a truncated Leu residue. The ONIOM calculated DS of PhQ and 2MNQ is given in Figure 2.10D. In the neutral region of DDS, bands of 2MNQ are negative, while bands of PhQ are positive. The neutral quinone spectra is complicated and poorly understood.

A very clear feature in the experimental DDS from 1800~1550 cm^{-1} is the difference band at 1663/1656 cm^{-1}, indicating a band of PhQ at 1656 cm^{-1} with a corresponding band in 2MNQ at 1663 cm^{-1}. A C=O absorption band of PhQ in solvent is observed at ~1662 cm^{-1}. More specifically, the normal mode, which gives rise to most of the intensity of the 1662 cm^{-1}, band is an asymmetric stretching vibration of both C=O groups. The frequency of this normal mode upshifts to 1666 cm^{-1} when the phytyl chain is replaced by a hydrogen atom (Figure 2.6).

FTIR spectroscopy studies also suggested that the negative band near 1655 cm^{-1} in the trimeric A_1^-/A_1 FTIR DS is little impacted by deuteration and downshifts ~26 cm^{-1} upon ^{18}O labeling [82, 87]. Therefore, a frequency of 1655 cm^{-1} is due to a PhQ C=O mode that is free from H-bonding. ONIOM calculation of PhQ in the neutral state also shows that the band at 1656 cm^{-1} is due to the C_1=O stretching of PhQ, which is free from H-bonding. In addition, ONIOM calculation suggests that frequency of 2MNQ C_1=O stretching in the A_1 binding site is 7 cm^{-1} higher than that of PhQ. Therefore, the ONIOM calculations suggest that the difference band at 1663/1656 cm^{-1} in the (2MNQ-PhQ) DDS is due to the C_1=O stretching of 2MNQ/PhQ.

ONIOM calculations of PhQ and 2MNQ show that a negative band at 1638 cm^{-1} in the experimental (2MNQ-PhQ) DDS is not due to quinone. In the previous studies, it was found the

difference band at 1643/1634 cm^{-1} in the A_1^-/A_1 FTIR DS downshifted 8~10 cm^{-1} upon deuteration, suggesting it could be due to amide I mode [82].

In summary, in the anion quinone region of (2MNO-PhQ) DDS, the bands of 2MNQ at 1504 and 1428 cm^{-1} corresponds to the bands of PhQ at 1495 and 1415 cm^{-1}. The comparison of these bands is taken to further support the C=O character previously assigned to the 1654, 1495, and 1415 cm^{-1} bands of PhQ in the A_1 binding site. In the calculated spectrum of ONIOM calculations, the vibrational frequency of C_4=O group of PhQ^- downshifts ~80 cm^{-1} compared to the vibrational frequency of C_1=O group. This observation agrees with the notion of a strong H-bonding to semiquinone derived from ENDOR studies of A_1^-. The band at 1656 cm^{-1} in the (2MNQ-PhQ) FTIR DDS is due to PhQ, with corresponding mode of 2MNQ at 1663 cm^{-1}. The ONIOM calculation also predict that the antisymmetric H-bond also uncouples the two C=O modes of neutral PhQ, and C_4=O group of PhQ downshifts ~60 cm^{-1} compared to the vibrational frequency of C_1=O group. The close analogy between the DDS calculated for RCs reconstituted either with PhQ or with 2MNQ shows that the phytyl chain of PhQ imparts no specific constraint on the geometry of the menaquinone head group in its binding site for both the neutral and reduced state.

2.3.6 Kinetics of infrared absorption change at 77K

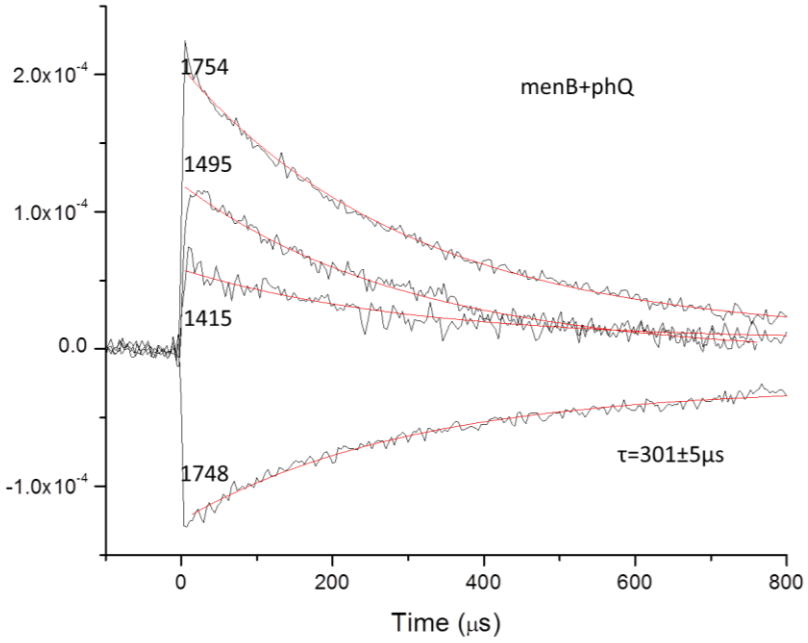

Figure 2.11 Kinetics of absorption changes at 1754, 1748, 1495 and 1415 cm^{-1} obtained following 532 nm laser flash excitation of *men*B PS I particles with PhQ incorporated into the A_1 binding site at 77K. Data were collected in 5 μs increments. The four kinetics were fitted simultaneously to a single-exponential function plus a constant. The fitted functions shown (red) are characterized by a time constant of 301 μs.

To gain an appreciation of the noise level achievable/required for these TRSS FTIR measurements on PS I particles, it is useful to consider the kinetics of the absorption changes at various IR frequencies. Figure 2.11 shows the time course of the absorption changes at several frequencies in the A_1^-/A_1FTIR DS obtained using *men*B PS I particles with PhQ incorporated into the A_1 binding site at 77K. Kinetics of the absorption changes observed at 1754, 1748, 1495, and 1415 cm^{-1} were obtained following 532 nm laser flash excitation of PhQ-containing PS I particles from *menB* mutants at 77K. Data was collected in 5 μs increments. The initial amplitude of the 1754 cm^{-1} time-course is ~$2x10^{-4}$, and the noise level is close to 10^{-5}.

The four kinetic traces were fitted simultaneously to a single decaying exponential component plus a constant component. The fitted functions shown (red) are characterized by a

time constant of 301 µs, which is similar to previous study [82]. The kinetic at 1754 cm^{-1} contains contributions from the decay of $P700^+$ and A_1^-, while the kinetic at 1748 cm^{-1} contains contributions from the recovery of P700 and A_1. The kinetic at 1495 and 1415 cm^{-1} are mostly due to the decay of PhQ^- in the A_1 binding site.

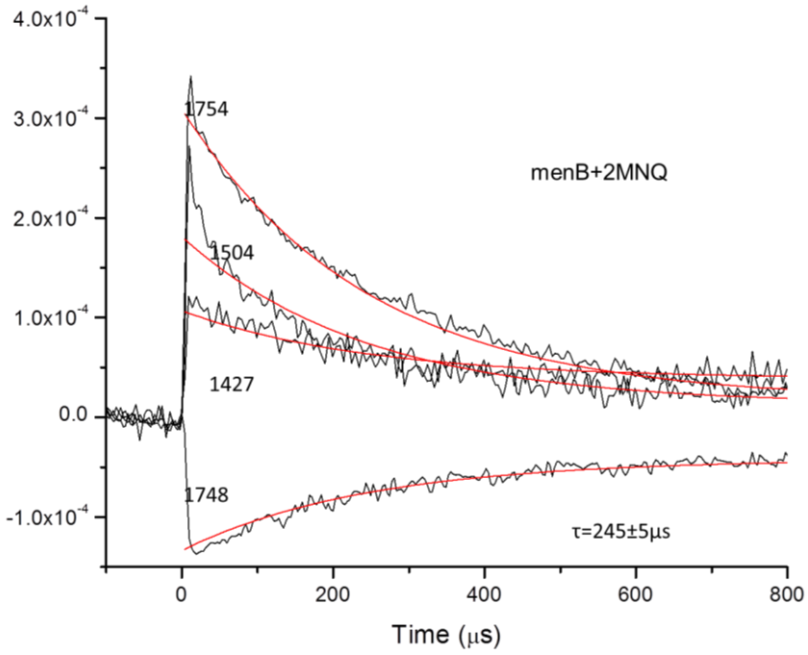

Figure 2.12 Kinetics of absorption changes at 1754, 1748, 1504 and 1427 cm^{-1} obtained following 532 nm laser flash excitation of *men*B PS I particles with 2MNQ incorporated into the A_1binding site at 77K. Data were collected in 5 μ increments. The four kinetics were fitted simultaneously to a single-exponential function plus a constant. The fitted functions shown (red) are characterized by a time constant of 245 µs.

Figure 2.12 shows kinetics of absorption changes at 1754, 1748, 1504, and 1427 cm^{-1} obtained following 532 nm laser excitation of *men*B PS I particles with 2MNQ incorporated into the A_1 binding site at 77K. By fitting the four kinetics in Figure 2.12 simultaneously to a single-exponential component (plus a constant component), we find that the decays are characterized by a time constant of 245 µs, which is faster than *men*B PS I particles with PhQ incorporated into the A_1 binding site at 77K. As discussed above, the band at 1504 and 1427 cm^{-1} are due to

$2MNQ^-$, therefore this 245 µs time constant is the indicative of recombination of the $P700^+A_1^-$ state for *men*B PS I particles with PhQ incorporated into the A_1binding site at 77K.

The midpoint potential of 2MNQ (-420 mv vs. NHE) is +50 mV more oxidizing than that of PhQ (-470 mV vs. NHE) when measured in dimethylformamide (DMF) [92]. The midpoint potential of quinone in the A_1 binding site of PS I (*Em*) can be calculated as following [93]:

$$Em + 700mV = 0.69(E + 387mV)$$

Where *E* is the midpoint potential of quinone measured in DMF.

By employing a value of -420 mV (vs. NHE) for the midpoint potential of 2MNQ in DMF, a midpoint potential of ~-723 mV was estimated for 2MNQ in the A_1 binding site, which is +35 mV more oxidizing than that of PhQ in the A_1 binding site. The change in midpoint potential of would result in increasing the rate of electron transfer between A_1 and F_X.

The rate of electron transfer in protein can be described by a simplified empirical equation, which is given by [94-97]:

$$lgk_{et} = 15 - 0.6R - 3.1(\Delta G + \lambda)^2/\lambda$$

Where, *R* is the edge-to-edge distance between the two redox cofactors; ΔG is the free energy difference between the two redox cofactors; and λ is the reorganization energy. As the ΔG decreases, the rate of electron transfer increases.

If a consensus midpoint potential -688 mV was assign to F_X, the free energy gap between 2MNQ and F_X in PS I is 35 mV, whereas the free energy gap between PhQ and Fx in PS I is 70mV. Since 2MNQ is positioned and oriented identically to the native PhQ in the A_1 binding site, the distance between 2MNQ and F_X should be similar to that of PhQ. The lower free energy difference and similar distance between quinone and F_X would lead to a higher rate of electron transfer from 2MNQ to F_X in PS I. Consequently, forward electron transfer from 2MNQ to F_X

would become slower and the recombination between $P700^{+}$ and F_A/F_B^{-} would become faster. At 77K, the rate of forward electron transfer is limited to the formation and the charge recombination of $P700^{+}A_1^{-}$ is the dominant reversible process. Therefore, the decay of the bands due to $2MNQ^{-}$ should be faster than that of PhQ^{-} in the A_1 binding site, which agrees with the above experimental results.

2.4 Conclusion

We have incorporated PhQ and 2MNQ back into the A_1 binding site of PS I particles from *men*B mutants. Using these PS I particles, we have produced A_1^{-}/A_1 FTIR DS for PhQ and 2MNQ, respectively. To identify the bands which are associated with quinone in the A_1^{-}/A_1 FTIR DS, DFT and ONIOM based vibrational frequency calculations are undertaken. By comparing these calculations with experimental work, we have found that the phytyl tail of PhQ does not play an important role in the orientation and vibrational properties of PhQ in the A_1 binding site. The ONIOM based calculations show that the bands of 2MNQ at 1504 and 1428 cm^{-1} corresponds to the bands of PhQ at 1495 and 1415 cm^{-1} in the DDS, which are due to C_1⋯O mode and C_4⋯O mode of reduced PhQ, suggesting a single H-bond to the C_4=O group of PhQ^{-}.

3 TIME-RESOLVED FTIR SPECTROSCOPY FOR STUDY OF THE A_1 BINDING SITE WITH ISOTOPE LABELED QUINONE IN PHOTOSYSTEM I

Abstract

To distinguish bands associated neutral or reduced phylloquinone (PhQ) from protein bands in the A_1^-/A_1 FTIR difference spectra (DS), we have adopted the fully ^{13}C labeled photosystem I (PS I) particles from *men*B mutants reconstituted with unlabeled PhQ. The comparison of time-resolved FTIR DS obtained for ^{13}C labeled PS I particles with unlabeled and ^{13}C labeled PhQ allows a clear discrimination of bands due to neutral or reduced PhQ from bands associated with protein vibrations.

Density function theory based vibrational frequency calculations are undertaken for unlabeled and ^{18}O or ^{13}C isotope labeled PhQ in the presence of a leucine residue. ONIOM type (QM/MM) calculations are also performed to investigate the vibrational frequencies for unlabeled and ^{18}O or ^{13}C isotope labeled PhQ in the A_1 binding site of PS I. The calculated vibrational frequencies of both neutral and reduced PhQ in the A_1 binding site suggest that the strong hydrogen bond between LeuA722 and PhQ results in the large downshift of H-bonded C_4=O mode of PhQ and PhQ^-.

3.1 Introduction

In type I photosynthetic reaction centers, two phylloquinone (PhQ) molecules are bound to the protein subunits and act as the secondary electron acceptor, A_1. PhQ in the A_1 binding site has a midpoint closed to -800 mV, and PhQ is one of the most reducing quinones in biological systems [81, 98, 99]. The unprecedented redox potential of PhQ^- in the A_1 binding site is in part a result of interactions between PhQ and the surrounding protein environment. The crystal structure of photosystem I (PS I) at 2.5 Å provides a detailed view of the amino acids

surrounding PhQ, and suggests several possible pigment-protein interactions [4]. Figure 2.1 shows a view of the PhQ molecule bound to PsaA (denoted $A_{1\text{-}A}$) and neighboring amino acids.

The ring of PhQ is π-stacked with the indole ring of TrpA697, and one of the carbonyl groups of PhQ is hydrogen (H) bonded to the peptide NH group of LeuA722. The hydroxyl side chain of SerA692 could be H-bonded to the backbone oxygen of MetA688, whereas the indole NH group of TrpA697 could be H-bonded to the hydroxyl oxygen of SerA692. MetA688 also ligates the central magnesium atom of the A_0 chlorophyll-a. The interaction with the Trp residue was assumed to destabilize the negative charge on the semiquinone anion radical, thereby lowering its redox potential of PhQ^- [20]. In contrast, the H-bond withdraws electron density and stabilizes the negative charge on the semiquinone anion radical, thereby raising its redox potential PhQ^- [38, 100].

Fourier transfer infrared (FTIR) difference spectroscopy (DS) has contributed greatly to investigate the structural details of electron transfer cofactors in the photosynthetic complexes [15, 82-84, 87, 101, 102]. Time-resolved step-scan (TRSS) FTIR DS with 5 μs resolution was used to generate $P700^+A_1^-/P700A_1$ FTIR DS at 77K. A_1^-/A_1 FTIR DS was produced by subtracting the static $P700^+/P700$ FTIR DS from the time-resolved (TR) $P700^+A_1^-/P700A_1$ FTIR DS. Though the contributions of P700 and $P700^+$ were removed, the features of other components such as A_0, amide I and II still appear in A_1^-/A_1 FTIR DS [82]. By changing the reduced mass, the isotope edited FTIR spectroscopy can assign a specific group from a large protein. Multiple assignments have been suggested for A_1 and A_1^- vibrational bands with specific isotope labeling [82, 87, 102]. For PS I particles from *men*B mutants with ^{18}O labeled PhQ incorporated into the A_1 binding site, the band at 1495 cm^{-1} due to an antisymmetric vibration of both C⋯O stretching for PhQ^- downshifts 14 cm^{-1} to 1481 cm^{-1}. Furthermore, the band at

1654cm^{-1}, which downshifts 28 cm^{-1} upon ^{18}O labeling, is identified as C_1=O stretching of the non H-bonded carbonyl group [87]. FTIR spectroscopic studies confirmed the occurrence of a single H-bond to A_1, which was suggested by the X-ray crystal structure [4]. Density functional theory (DFT) based vibrational frequency calculations have suggested that in the presence of a single H-bond, the C=O stretching of two carbonyl groups of PhQ could split into two modes, and the vibrational frequency of C=O stretching due to the H-bonded carbonyl group should downshift. However, the C=O mode of the H-bonded carbonyl group was not well resolved in the experiment, and only one intense difference band for PhQ^- was observed in the ^{18}O-^{16}O FTIR double difference spectrum (DDS) [87] .

In recent years, DFT based calculations have been undertaken on small H-boned complexes in solution or protein environment. In previous studies, the model used for calculating vibrational modes of PhQ in the A_1 binding site only includes a PhQ molecule and a truncated Leu residue (or a water molecule) [90]. However, electron paramagnetic renounce (EPR) studies have suggested that mutations of amino acids such as TrpA697 or SerA692 in close contact with the PsaA side quinone lead to change the spin density distribution of the reduced quinone [41]. Theoretical studies have also shown that the fixed π-stacked arrangement of PhQ^- and Trp results in lowering the redox potential of $P700^+A_1^-$ [43]. The recent ONIOM calculation also suggests that the ^{17}O anisotropic hyperfine coupling is sensitive to interactions with neighboring groups, especially TrpA697 and PheA689 [45].

ONIOM type QM/MM method can model a very large system by defending two or more layers within the structure, which are treated at different levels of accuracy. In one layer, the chemical properties of the principal species can be calculated at a quantum mechanics (QM)

level, whereas the surrounding protein environment is included in the other layer using less computationally expensive molecular mechanics (MM) methods.

To understand A_1^-/A_1 spectra and the interactions between quinone and protein environment, we have undertaken such QM/MM calculations for PhQ in the A_1 binding site. In our calculations, quinone and H-bonding ligand are considered at the QM level using DFT based methods, whereas surrounding residues are treated with the MM level using universal force field (UFF) [88].

In this chapter, we have used microsecond TR FTIR DS to probe the molecular properties of PhQ in the A_1 binding site at 77K. To distinguish bands associated with neutral or reduced PhQ from protein bands in TR FTIR DS, we compared the fully ^{13}C labeled PS I particles from *men*B mutants incorporated with unlabeled and fully ^{13}C labeled PS I particles. Assignments for specific bands in the DS are proposed from a consideration of the isotope-induced band-shifts. To complement the experimental work and aid in FTIR difference band assignment, we have used ONIOM methods to calculate FTIR spectra associated with the isotope labeled quinones occupying the A_1 binding site. In addition, by comparing with the simpler isolated H-bonded models, we are able to examine the influence of the neighboring protein matrix on the vibrational modes of neutral and reduced PhQ.

3.2 Materials and Methods

3.2.1 Preparation of fully ^{13}C labeled PS I particles and incorporation of PhQ into PS I particles

For uniform ^{13}C labeling of cells, fully ^{13}C labeled glucose (Sigma) was added to the growth medium [82]. ^{13}C labeled trimeric PS I particles from *Synechocystis sp.* PCC. 6803 (*S6803*) and *menB* mutants were prepared as described previously [103-105]. The extent of

incorporation of the ^{13}C labeling was estimated to be >98% by monitoring the shift of the amide II absorption band (Figure3.2). Similar estimates were also obtained by comparing photo-accumulated $P700^+/P700$ FTIR DS obtained for unlabeled and ^{13}C labeled PS I particles at RT and 77K. To incorporate unlabeled PhQ back into the A_1 binding site, fully ^{13}C labeled PS I particles from *men*B mutants PS I particles were incubated in the presence of a large molar excess of unlabeled PhQ (dissolved in ethanol) as described in Chapter 2.

3.2.2 Photo-accumulated and microsecond time-resolved step-scan FTIR difference spectroscopy at 77K

Light induced photo-accumulation and TRSS FTIR measurements at 77K were described in Chapter 2. $P700^+/P700$ and $P700^+A_1/P700A_1$ FTIR DS were recorded for both fully ^{13}C labeled PS I particles from *S6803* and fully ^{13}C labeled PS I particles from *menB* mutants with unlabeled PhQ incorporated.

3.2.3 Estimating the noise level in double difference spectra

DS were scaled using a min-max algorithm in which the minimum/maximum y-value was set to 0.0/2.0. For each PS I sample, the TR measurements were repeated several times and then averaged. The standard deviation of the average spectra was taken as the most appropriate measure of experimental variability (noise level).

The error associated with the (^{13}C PhQ-^{12}C PhQ) FTIR DDS was calculated using equation (1),

$$\delta f = \sqrt{\delta A^2 + b^2 * \delta B^2} \qquad (1)$$

Where δf is the total error for the (^{13}C PhQ-^{12}C PhQ) FTIR DDS; δA is the standard deviation of $P700^+A_1^-/P700A_1$ FTIR DS obtained using fully ^{13}C PS I particles from *S6803*; δB is the standard deviation of $P700^+A_1^-/P700A_1$ FTIR DS obtained using fully ^{13}C *men*B PS I particles

with unlabeled PhQ incorporated; and *b* is the scale factor used to normalize the difference bands in $P700^{+}A_1^{-}/P700A_1$ FTIR DS obtained using fully ^{13}C labeled *men*B PS I particles with unlabeled PhQ incorporated.

The total error for the (^{13}C PhQ-^{12}C PhQ) TR FTIR DDS is shifted and centered on zero before being used to construct error bars.

3.2.4 DFT based vibrational frequency calculations

Models 1 and Model 2 (Figure 3.1) used for DFT based vibrational frequency calculations in Chapter 2 were also applied to calculate isotopic frequency shifts of PhQ or PhQ^{-} in the gas phase. Following the geometry optimization, vibrational frequency calculations were undertaken for both isotope labeled and unlabeled PhQ/PhQ^{-} using the B3LYP functional and the 6-31G+ (d) basis set. All carbon atoms of PhQ/PhQ^{-} were ^{13}C isotope labeled in order to estimate the isotopic frequency shifts caused by ^{13}C labeling. Carbonyl oxygen atoms of PhQ/PhQ^{-} were ^{18}O isotope labeled in order to estimate the isotopic frequency shifts caused by ^{18}O labeling.

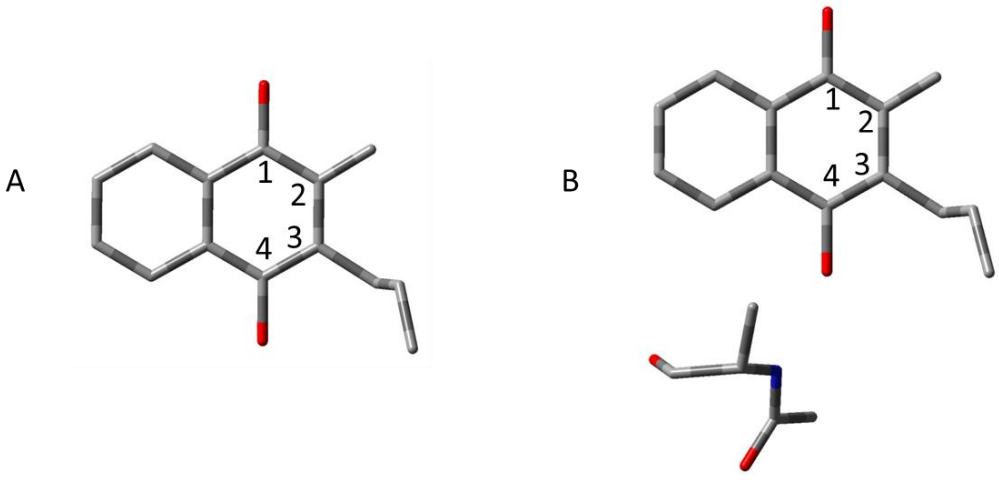

Figure 3.1 Structures and numbering scheme for DFT calculations of (A) PhQ in the gas phase (Model 1) and (B) PhQ in the presence of a truncated Leu residue (Model 2).

3.2.5 ONIOM type QM/MM vibrational frequency calculations

Model 3 used for ONIOM type vibrational frequency calculations in Chapter 2 were also used to predict the isotopic frequency shifts for the normal modes of PhQ and PhQ^-. Following the geometry optimization, DFT based vibrational frequency calculations (B3LYP/6-31G+ (d)) were performed on the QM layer. All carbon atoms of PhQ/PhQ^- were ^{13}C isotope labeled in order to estimate the isotopic frequency shifts caused by ^{13}C labeling. Carbonyl oxygen atoms of PhQ/PhQ^- were ^{18}O isotope labeled in order to estimate the isotopic frequency shifts caused by ^{18}O labeling. Calculated vibrational frequencies were scaled by 0.951 and 0.96 for neutral and reduced PhQ, respectively. Calculated (^{13}C-^{12}C) or (^{18}O-^{16}O) DDS have been produced by subtracting unlabeled spectrum from labeled spectrum. Vibrational frequencies due to the surrounding amino acids were cancelled and only isotopic groups of PhQ/PhQ^- were shown in the (^{13}C-^{12}C) or (^{18}O-^{16}O) DDS. All calculations were performed with the Gaussian 03 program [91].

Assignment of calculated vibrational frequencies to molecular groups is undertaken by visual identification of the molecular groups that most prominently contribute to the vibration. This visual identification is carried out using GaussView 4, in which the atomic motions associated with each of the vibrational modes can be displayed.

3.3 Results and discussions

3.3.1 IR absorption spectra of unlabeled and ^{13}C labeled PS I particles

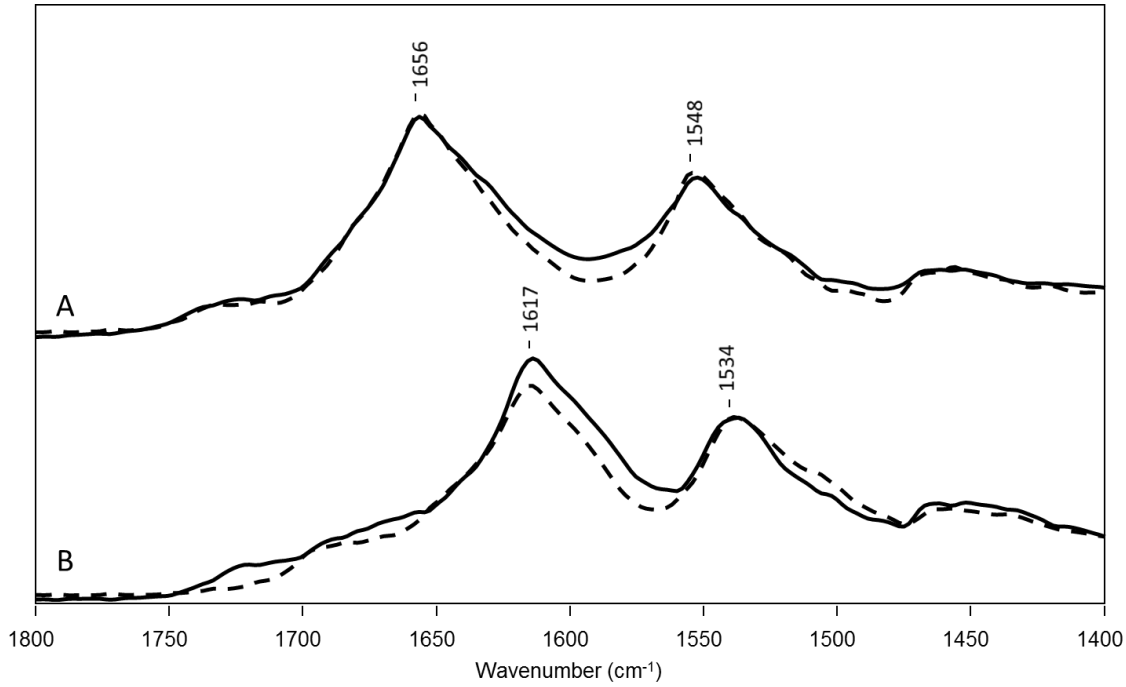

Figure 3.2 IR absorption spectra at 77K for unlabeled (A) and ^{13}C labeled (B) trimeric PS I particles from *menB* mutants (solid) and *S6803* (dotted).

Figure 3.2 (solid) shows IR absorption spectra in the 1800-1400 cm^{-1} region for unlabeled (A) and ^{13}C labeled (B) PS I particles from *men*B mutants. The IR absorption spectra for unlabeled and ^{13}C labeled PS I particles from *S6803* are also shown (dotted). The amide I band at 1656 cm^{-1} arises mainly from the C=O stretching vibration, with minor contributions from the out-of-phase C-N stretching vibration, N-H in plane bend and CCN deformation. The amide II band at 1548 cm^{-1} is due to the out-phase combination of the N-H in plane bend and the C-N stretching vibration, with smaller contributions from the C-O in plane bend and the C-C and N-C stretching vibrations [106]. Upon ^{13}C labeling, the absorption band due to the amide I downshifts ~39 cm^{-1} to 1617 cm^{-1}, while the absorption band due to the amide II downshifts ~14 cm^{-1} to

1534 cm^{-1} for PS I particles from *men*B mutants and *S6803*. These isotope shifts in Figure 3.1 indicate that these PS I particles from *men*B mutants and *S6803* are fully ^{13}C labeled [106].

3.3.2 The (^{13}C-^{12}C) FTIR double difference spectra

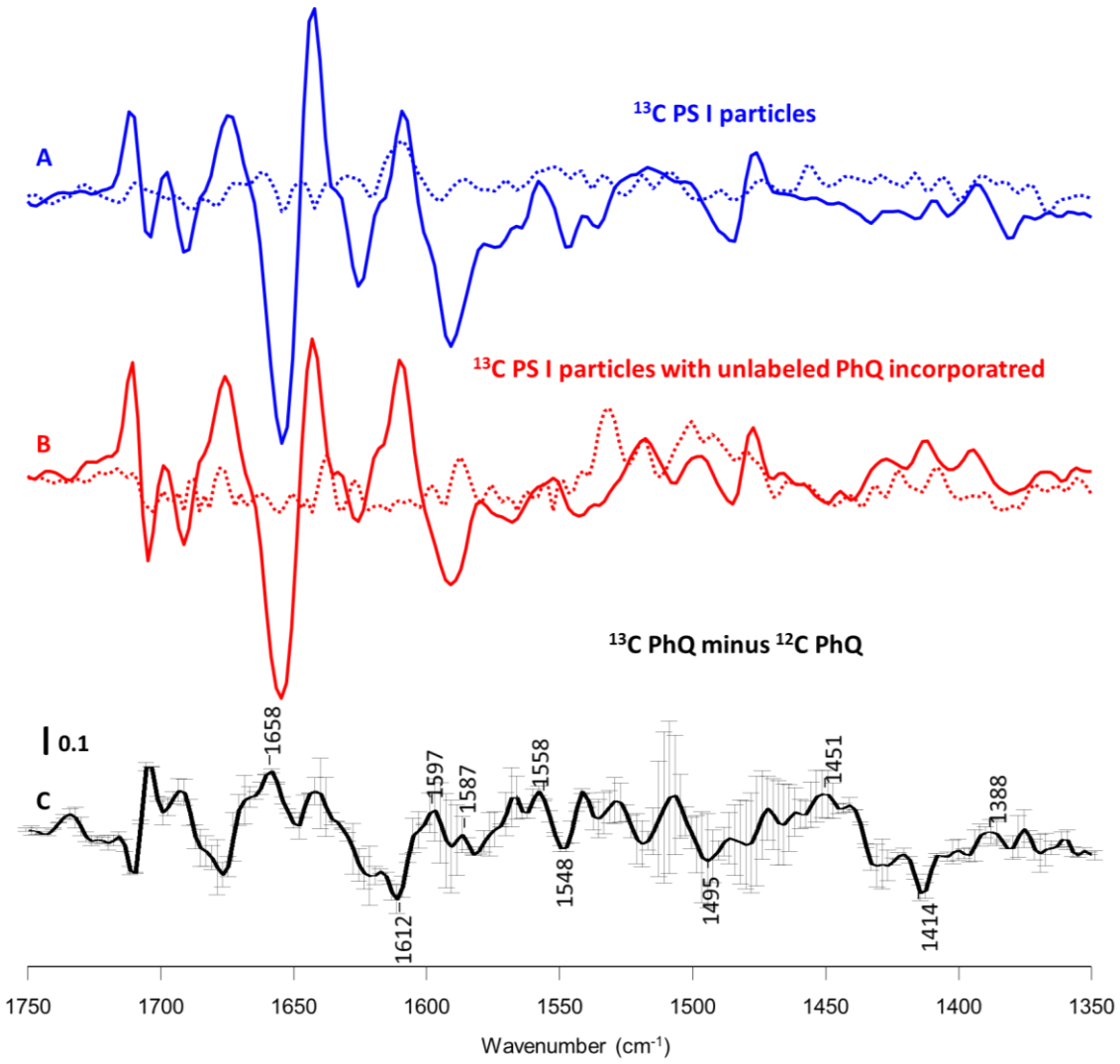

Figure 3.3 TR $P700^+A_1^-/P700A_1$ FTIR DS collected at 77 K for fully ^{13}C labeled PS I particles (A *solid*) and fully ^{13}C labeled PS I particles from *men*B mutants with unlabeled PhQ (B *solid*) incorporated into the A_1 binding site. The spectra shown are the average of 4 (^{13}C labeled PhQ) and 2 (unlabeled PhQ) separated experiments. The standard deviation spectra associated with the TR experiments for ^{13}C labeled PhQ (A) and unlabeled PhQ (B) are shown (*dotted*). These standard deviation spectra give a true measure of the experimental variability (noise level). (C) (^{13}C PhQ- ^{12}C PhQ) TR FTIR DDS obtained by subtracting spectrum B (*solid*) from spectrum A (*solid*). That is the TR $P700^+A_1^-/P700A_1$ FTIR DS obtained for fully ^{13}C labeled *men*B PS I particles with unlabeled PhQ incorporated is subtracted from the TR $P700^+A_1^-/P700A_1$ FTIR DS obtained for ^{13}C labeled PS I particles. The noise level is also shown in (C) (*error bars*), and is obtained by taking the square root of spectrum in (B *dotted*) squared plus

spectrum in (A *dotted*) squared. The vertical bar in (C) represents an optical density (OD) difference of ~$0.1x10^{-3}$.

In Figure 3.3, we present TR $P700^+A_1^-$/$P700A_1$FTIR DS obtained using fully ^{13}C labeled PS I particles from *men*B mutants reconstituted with unlabeled (^{12}C) PhQ and fully ^{13}C labeled *S6803* PS I particles, and (^{13}C-^{12}C) FTIR DDS. Figure 3.3A corresponds to fully ^{13}C labeled *S6803* PS I particles. Figure 3.3B corresponds to fully ^{13}C labeled PS I particles from *men*B mutants reconstituted with unlabeled (^{12}C) PhQ. The spectrum in Figure 3.3C is the (^{13}C-^{12}C) FTIR DDS, which is constructed by subtracting Figure 3.3B from Figure 3.3A. The standard deviations associated with time-resolved $P700^+A_1^-$/$P700A_1$FTIR DS obtained using fully ^{13}C labeled PS I particles from *men*B mutants reconstituted with unlabeled (^{12}C) PhQ and fully ^{13}C labeled *S6803* PS I particles are also shown in Figure 3.3. Error bands associated with the (^{13}C-^{12}C) FTIR DDS (Figure 3.3C) present the estimated noise using equation 1.

Usually, when we use TR $P700^+A_1^-$/$P700A_1$FTIR DS and $P700^+$/P700 FTIR DS to produce A_1^-/A_1 FTIR DDS, the feature bands of $P700^+$/P700 (1716(+), 1698(-), and 1687(+)) are normalized to cancel P700 and $P700^+$ contributions to the TR spectra. However, the difference band at 1716(+)/1698(-) cm^{-1} that is due to 13^1 keto C=O group of one of the Chl in P700 downshifts ~42 cm^{-1} to 1674(+)/1656(-) cm^{-1} upon ^{13}C labeling [82, 107]. FTIR DS studies in combination with isotope labeling suggested that part of the negative band at 1654 cm^{-1} is due to the non-H bonded C_1=O mode of neutral PhQ [87]. Therefore, not only P700 but also A_1 contributes to the negative band at 1654~1656 cm^{-1} in $P700^+A_1^-$/$P700A_1$ FTIR DS obtained using fully ^{13}C labeled PS I particles from *men*B mutants reconstituted with unlabeled PhQ. To avoid losing A_1 contributions to the (^{13}C-^{12}C) FTIR DDS, we have to construct (^{13}C-^{12}C) FTIR DDS by subtracting TR $P700^+A_1^-$/$P700A_1$FTIR DS obtained using fully ^{13}C labeled PS I particles from

*men*B mutants reconstituted with unlabeled (^{12}C) PhQ from TR P700^{+}A$_1^{-}$/P700A$_1$FTIR DS obtained fully ^{13}C labeled *S6803* PS I particles.

We have also shown that (^{18}O-^{16}O) FTIR DDS, constructed by directly subtracting the TR P700^{+}A$_1^{-}$/P700A$_1$ FTIR DS obtained using PS I particles with ^{18}O labeled and unlabeled PhQ , are very similar to those constructed by subtracting A$_1^{-}$/A$_1$ FTIR DS obtained using PS I particles with ^{18}O labeled and unlabeled PhQ [87].

In construction of (^{13}C-^{12}C) FTIR DDS, Figures 3.3 A and 3.3B were normalized so that the difference band at 1698(+)/1691(-) cm^{-1} has a similar amplitude in both spectra. This normalization also minimizes the differences in many of the bands which are due to P700 in the spectra. The difference band at 1698(+)/1691(-) cm^{-1} in TR P700^{+}A$_1^{-}$/P700A$_1$ FTIR DS is due to the 13^3 ester C=O group of the PsaA Chl of P700 upon ^{13}C labeling [108].

For PhQ reconstituted PS I particles, no ^{3}P700 features are observed in the TR FTIR DS, indicating that PhQ is incorporated into *men*B PS I particles at a very high level. In the (^{13}C-^{12}C) FTIR DDS (Figure 3.3C), several intensive bands observed at 1711 (+), 1704 (-), 1693 (+), 1677 (-), 1658(+) and 1612 (-) cm^{-1} are larger than the estimated noise in the region from 1750~ 1600 cm^{-1}.

The previous FTIR DS studies have shown that, for unlabeled *S6803* PS I particles, the difference band at 1754 (+)/1749 (-) cm^{-1} downshifts 43~45 cm^{-1} to 1711 (+)/1704 (-) cm^{-1} upon ^{13}C labeling, and 5~8 cm^{-1} to 1749 (+)/1741 (-) cm^{-1} upon deuteration in the A$_1^{-}$/A$_1$ FTIR DS. The sotope-induced downshifts suggests that the 1711 (+)/1704 (-) cm^{-1} difference band is due to the 13^3 ester C=O group of A$_0$ in the A$_1^{-}$/A$_1$ FTIR DS [82]. Figure 3.3 A/B shows that the intensity of the difference band at 1711(+)/1704 (-) cm^{-1} increases when unlabeled quinones are incorporated into ^{13}C labeled PS I particles. The change of intensity may correspond to the

alteration of the long-range electrostatic effects between A_1 and A_0. The perturbation of A_0 upon reduction of A_1 was discussed previously [82].

As discussed before, for the (^{13}C-^{12}C) FTIR DDS, the neutral quinone spectral region (1770-1550 cm^{-1}) overlaps the downshifts of $P700^+$/P700 features caused by ^{13}C labeling. This overlap makes it difficult to identify the bands in the (^{13}C-^{12}C) FTIR DDS. However, a positive band at 1658 cm^{-1} and a negative band at 1612 cm^{-1} are clearly observed in Figure 3.3C, which may be due to the C=O modes of PhQ. In Figure 3.3A two positive bands at 1495 and 1415 cm^{-1} decrease in intensity on ^{13}C labeling, whereas two positive bands at 1451 and 1388 cm^{-1} increase in intensity. These give rise to the 1495 (+)/1451(-) cm^{-1} and 1451(+)/1388(-) cm^{-1} features in the (^{13}C-^{12}C) FTIR DDS. However, the noise level in Figure 3.3C in the 1530~1350 cm^{-1} region is considerable, and the spectral features mentioned are similar in amplitude to this noise level. It is therefore difficult to place any real confidence in the validity of the observed spectral features, particularly the 1495 (+)/1451(-) cm^{-1} feature. To reduce the validity of the spectral features, more experiments are needed.

3.3.3 Calculated isotope edited spectra of reduced PhQ in the A1 binding site

By comparing A_1^-/A_1 FTIR DS for PS I particles with unlabeled and ^{18}O labeled PhQ incorporated, an (^{18}O-^{16}O) FTIR DDS has been produced [87]. The positive band at 1495 cm^{-1} in the A_1^-/A_1 FTIR DS was found to downshift 14 cm^{-1} and decrease in intensity upon ^{18}O labeling. DFT based vibrational frequency calculations for isolated PhQ or PhQ with an asymmetrical H-bond indicate that the band at 1495 cm^{-1} in the A_1^-/A_1 FTIR DS is due to an antisymmetric vibration of both C⋯O groups of PhQ^-. DFT based vibrational frequency calculations also predict that the band, which only downshifts 7 cm^{-1} upon ^{18}O labeling, is due to C=C stretching

modes of both rings of PhQ^-, coupled to C-H bending, CH_2 wagging modes and the antisymmetric vibration of both C⋯O groups of PhQ^- .

Comparisons of experimental and calculated (^{18}O-^{16}O) isotope edited FTIR DDS for reduced PhQ are shown in Figure 3.4. Figure 3.4A shows the experimental (^{18}O-^{16}O) isotope edited FTIR DDS for reduced PhQ in the region of 1530-1350 cm^{-1}, which is very similar to that produced previously [87]. Figure 3.4 B and C correspond to the vibrational mode frequency calculations for isolated PhQ (Model 1) and PhQ in the presence of a Leu residue (Model 2) based on DFT method. Figure 3.4D corresponds to the ONIOM calculation (Model 3). In Figure 3.4, bands of ^{16}O PhQ^- are all negative, whereas bands of ^{18}O PhQ^- are all positive. All calculated spectra in Figure 3.4 agree with the experimental results that a band at 1495 cm^{-1} downshifts ~14 cm^{-1} upon ^{18}O labeling. However, the difference band at 1415 (+)/1409 (-) cm^{-1} observed in Figure 3.4A is ~27 and 22 cm^{-1} lower than the predictions of Model 1 and 2, respectively, but only ~10 cm^{-1} higher than the prediction of Model 3.

The ONIOM calculated IR DS in Figure 3.4D is closed to the experimental result (Figure 3.4A). In the ONIOM calculation (Model 3), upon quinone reduction, the C_1⋯O stretching are coupled with C_2=C_3 stretching at 1517 cm^{-1} (asymmetrically) and 1495 cm^{-1} (symmetrically). The intensive band at 1495 cm^{-1}, which is mainly due to C_1⋯O stretching, downshifts 13 cm^{-1} to 1482 cm^{-1} upon ^{18}O labeling. The band near 1409 cm^{-1} which is mainly due to C_4⋯O stretching downshifts 11 cm^{-1} to 1398 cm^{-1} upon ^{18}O labeling. There are actually two bands, 1415 and 1409 cm^{-1}, which are both due to quite similar modes.

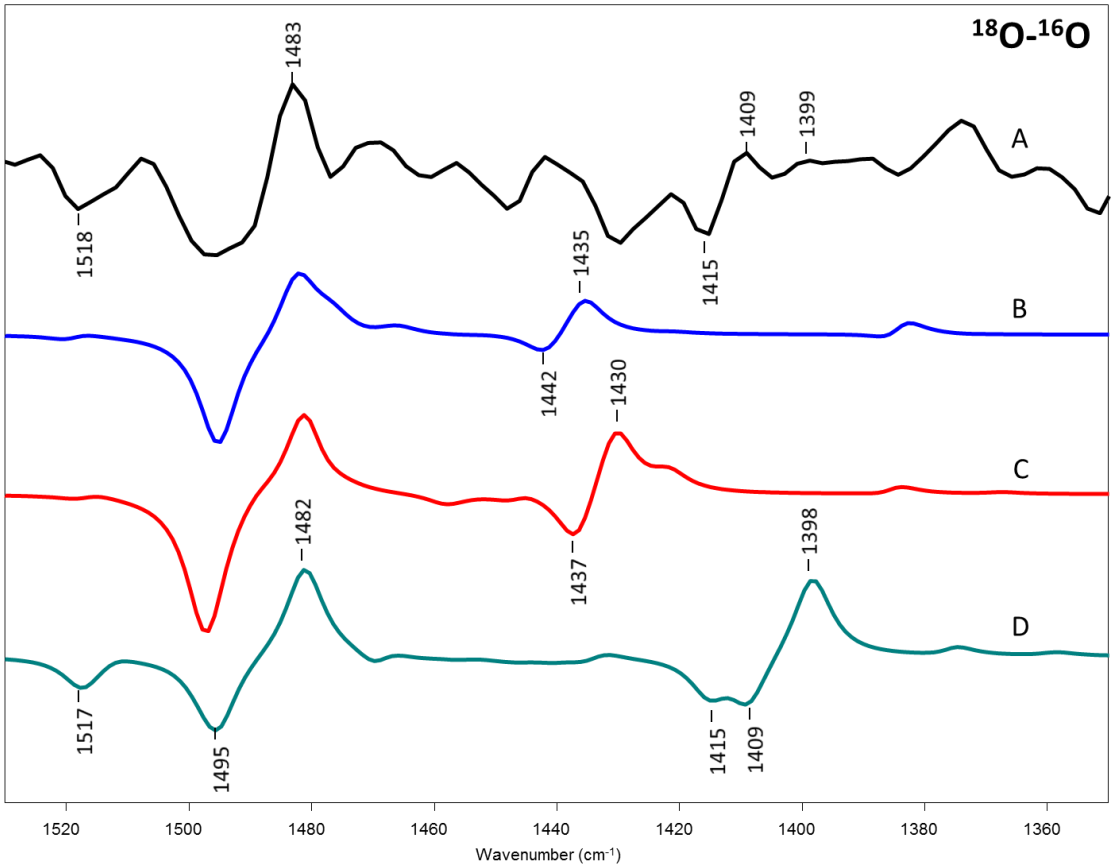

Figure 3.4 Experimental (A) [87] and calculated (^{18}O-^{16}O) isotope edited FTIR DDS for reduced PhQ. (B) DFT calculation for isolated reduced PhQ in the gas phase. (C) DFT calculation for PhQ in the presence of a Leu residue. (D) ONIOM calculations for reduced PhQ in the A_1 binding site. Calculated normal mode frequencies were scaled by 0.974, 0.974 and 0.96, respectively.

The ^{13}C isotope edited FTIR DS is more complicated. Not only the bands due to carbonyl groups, but also all bands that correspond to carbon atoms would downshift. The noise level indicates that the spectral variability of experimental (^{13}C-^{12}C) FTIR DDS in the region from 1530-1350 $cm^{-1}$is large and more experimental data are required to reduce noise. However, the calculated (^{13}C-^{12}C) FTIR DDS can predicate band shifts due to ^{13}C labeled PhQ and assess the band assignments in the A_1^-/A_1 FTIR DS. For the calculated (^{13}C-^{12}C) FTIR DDS in Figure 3.5, bands of unlabeled (^{12}C) PhQ^- are negative, while bands of ^{13}C labeled PhQ^- are positive.

There are two predominate difference bands in Figure 3.5B. The calculated spectrum of Model 1 suggests that the stretching of both C⋯O groups of PhQ^- couples antisymmetrically at

1495 cm^{-1} and downshifts 47 cm^{-1} to 1448 cm^{-1} upon ^{13}C labeling. The band at 1441 cm^{-1}, which downshifts 36 cm^{-1} to 1405 cm^{-1}, is due to the antisymmetric C⋯O mode of PhQ^- coupled to the C-C mode of quinonic and aromatic ring, and C-H wagging on the aromatic ring. In Figure3.5 C the intensive band at 1497 cm^{-1}, which downshifts 42 cm^{-1} to 1455 cm^{-1} upon ^{13}C labeling, comes from the antisymmetric C⋯O group of PhQ^-. The band at 1437 cm^{-1} in Figure 3.5C is due to the same mode at 1441 cm^{-1} in Figure3.5B, and downshifts 34 cm^{-1} upon ^{13}C labeling. For reduced PhQ, the predictions of Model 2 are very similar to Model 1, indicating that the H-bond between the backbone NH group of a Leu residue and reduced PhQ is weak. However, the advanced pulse EPR and ENDOR studies suggested the presence of a strong H-bond to the reduced quinone in the A_1 binding site [69].

As shown in Figure 3.5D, the ONIOM calculations (Model 3) suggest that a band at 1517 cm^{-1} is due to the C_1⋯O mode coupled with C_2=C_3 mode. In Model 3, the negative band at 1495 cm^{-1} downshifts 21 cm^{-1} to 1474 cm^{-1} with decreasing intensity upon ^{13}C labeling (Figure 3.5D). The positive band at 1450 cm^{-1} is assigned to the antisymmetric coupling of C_1⋯O and C_4⋯O groups of reduced PhQ by Model 3. The negative band near 1409 cm^{-1} downshifts 29 cm^{-1} to 1380 cm^{-1} upon ^{13}C labeling, and is assigned to the C_4⋯O mode in the Model 3. The large downshift of C_4⋯O mode of PhQ^- suggests a strong H-bond between the backbone NH group of a Leu residue and reduced PhQ, which confirms the previous advanced pulse EPR and ENDOR studies.

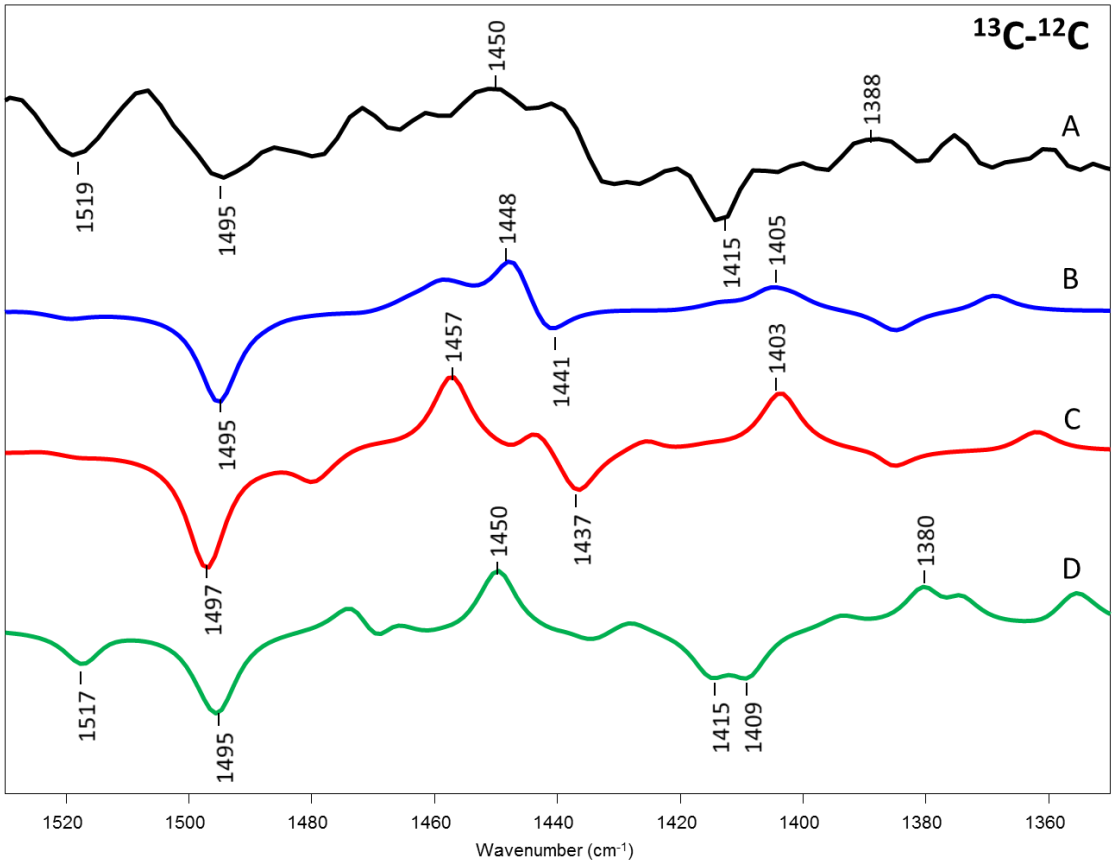

Figure 3.5 Experimental (A) and calculated (^{13}C-^{12}C) isotope edited FTIR DDS for reduced PhQ. (B) DFT calculation for isolated reduced PhQ in the gas phase. (C) DFT calculation for PhQ in the presence of a Leu residue. (D) ONIOM calculations for reduced PhQ in the A_1 binding site. Calculated normal mode frequencies were scaled by 0.974, 0.974 and 0.96, respectively.

3.3.4 Calculated isotope edited spectra of neutral PhQ in the A_1 binding site

The identification of bands associated with neutral PhQ in the TR FTIR DS is still questionable, because the C=O modes of PhQ occur in the region of 1660-1650 cm^{-1}, where the amide I also has huge absorption. However, calculated spectra can help us to identify the bands due to neutral PhQ in the A_1 binding site.

In the resulting isotope edited FTIR DDS of neutral PhQ, vibrational bands of unlabeled PhQ appear as positive signals, while vibrational bands of labeled PhQ appear as negative signals. Figures 3.6A and 3.7A show the experimental (^{18}O-^{16}O) and (^{13}C-^{12}C) FTIR DDS in the

neutral quinone spectral region (1700 -1550 cm^{-1}). Models 1-3 are also used to assign spectra featured to vibrational modes of neutral PhQ in Figure 3.6 and 3.7.

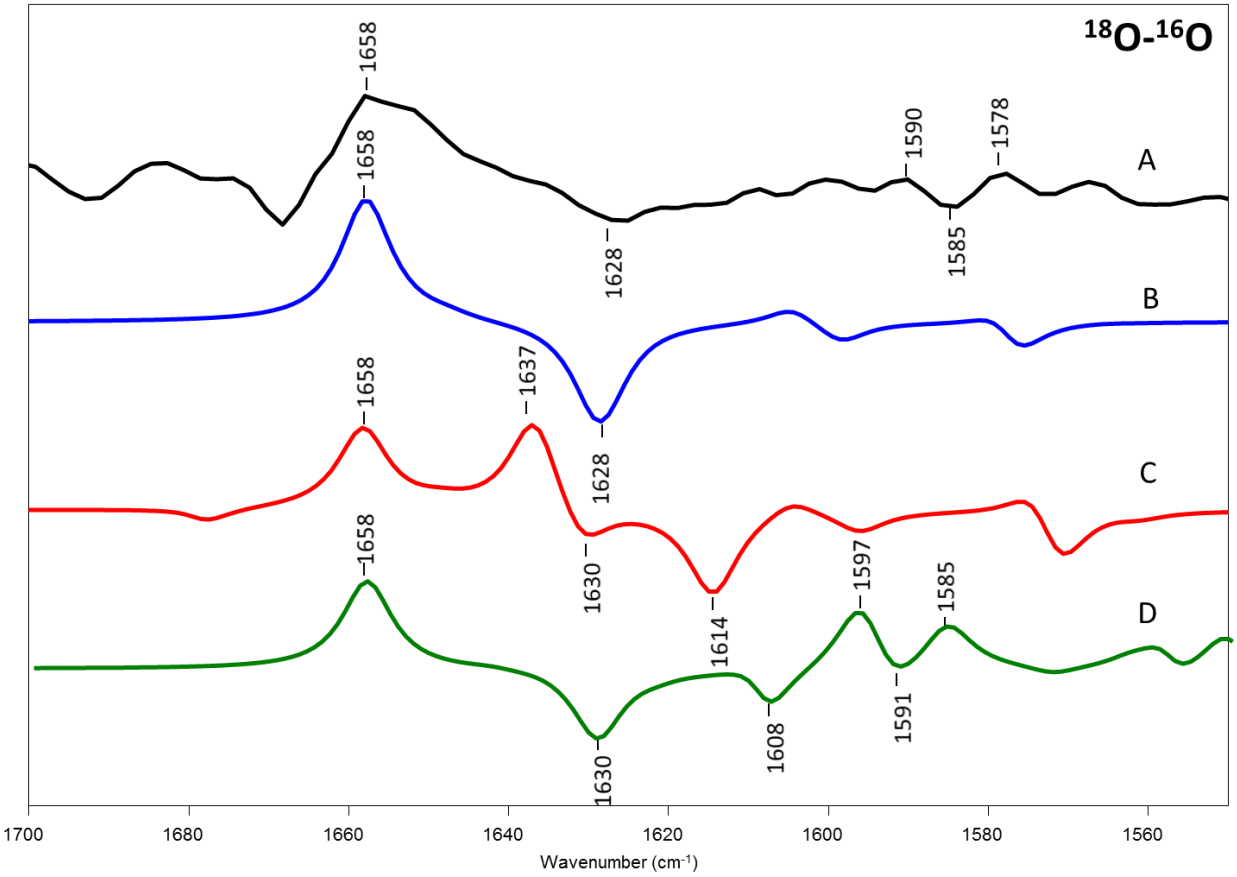

Figure 3.6 Experimental (A) and calculated (^{18}O-^{16}O) isotope edited FTIR DDS for neutral PhQ. (B) DFT calculation for isolated neutral PhQ in the gas phase. (C) DFT calculation for PhQ in the presence of a Leu residue. (D) ONIOM calculations for neutral PhQ in the A_1 binding site. Calculated normal mode frequencies were scaled by 0.963, 0.963and 0.953, respectively.

Figure 3.6A and 3.7A show that the band at 1658 cm^{-1} downshifts 30/46 cm^{-1} to 1628/1612 cm^{-1} upon ^{18}O and ^{13}C labeling, respectively. This band is assigned to antisymmetric C=O groups of neutral PhQ in Model 1. In Model 1, the band at 1605 cm^{-1}, which is due to C_2=C_3 stretching, downshifts 6/57 cm^{-1} to 1599/1548 cm^{-1} upon ^{18}O and ^{13}C labeling, respectively. Model 1 also suggests that the band at 1580 cm^{-1}, which is due to C=C mode of aromatic ring, downshifts 5/56 cm^{-1} to 1575/1544 cm^{-1} upon ^{18}O and ^{13}C labeling, respectively.

However, the band separation of two C=O modes caused by the H-bond is not observed in Figure 3.6A.

From DFT based vibrational frequency calculations for PhQ with the C_4=O group H-bonded to the backbone of NH of a Leu residue (Model 2), the band at 1658 cm^{-1} is expected for a non H-bonded C_1=O mode of PhQ, and downshifts 28/42 cm^{-1} to 1630/1616 cm^{-1} upon ^{18}O and ^{13}C labeling, respectively. The band at 1637 cm^{-1} comes from the H-bonded C_4=O group of PhQ and downshifts 23/43 cm^{-1} upon ^{18}O and ^{13}C labeling, respectively. Figure 3.6C also shows that the band at 1605 cm^{-1}, which is due to C_2=C_3 stretching, downshifts 6 cm^{-1} to 1599 upon ^{18}O labeling. The band at 1575 cm^{-1}, which is due to C=C mode of aromatic ring, downshifts 4 cm^{-1} to 1571 cm^{-1} upon ^{18}O labeling.

The ONIOM calculations of the A_1 binding site are more sophisticated and agree with experiment. The band at 1658 cm^{-1} downshifts 28/41 cm^{-1} to 1630/1617 cm^{-1} upon ^{18}O and ^{13}C labeling, and is assigned to the non H-bonded C_1=O group of PhQ in Model 3. Model 3 suggests that the stretching of C_4=O group is strongly coupled to the C_2=C_3 stretching. The band at 1597 cm^{-1} comes from the symmetric coupling of the C_4=O mode and C_2=C_3 mode, while 1586 cm^{-1} comes from the antisymmetric coupling of the C_4=O mode and C_2=C_3 mode. The stretching of C_4=O group downshifts to 1539/1546 cm^{-1} upon ^{18}O and ^{13}C labeling, respectively. In Model 3, the non H-bonded C_1=O mode of PhQ absorbs ~60 cm^{-1} higher in frequency than the H-bonded C_4=O mode of PhQ. This prediction of Model 3 is much larger than that of Model 2, in which the separation of two C=O modes is only ~30 cm^{-1}, but very closed to the observation for PhQ in Figure 3.6A and 3.7A. In addition, the non H-bonded C_1=O mode also absorbs ~80 cm^{-1} higher in frequency than the H-bonded C_4=O mode of reduced PhQ. The two C=O modes are identified at 1660 and 1628 cm^{-1} for neutral ubiquinone in the Q_A^-/Q_A FTIR DS, and the separations of the

two C=O modes are only ~32 cm^{-1} [109]. Therefore, the ONIOM calculated prediction could indicate that PhQ in the A_1 binding site is more antisymmetrically H-bonded than ubiquinone in the Q_A binding site.

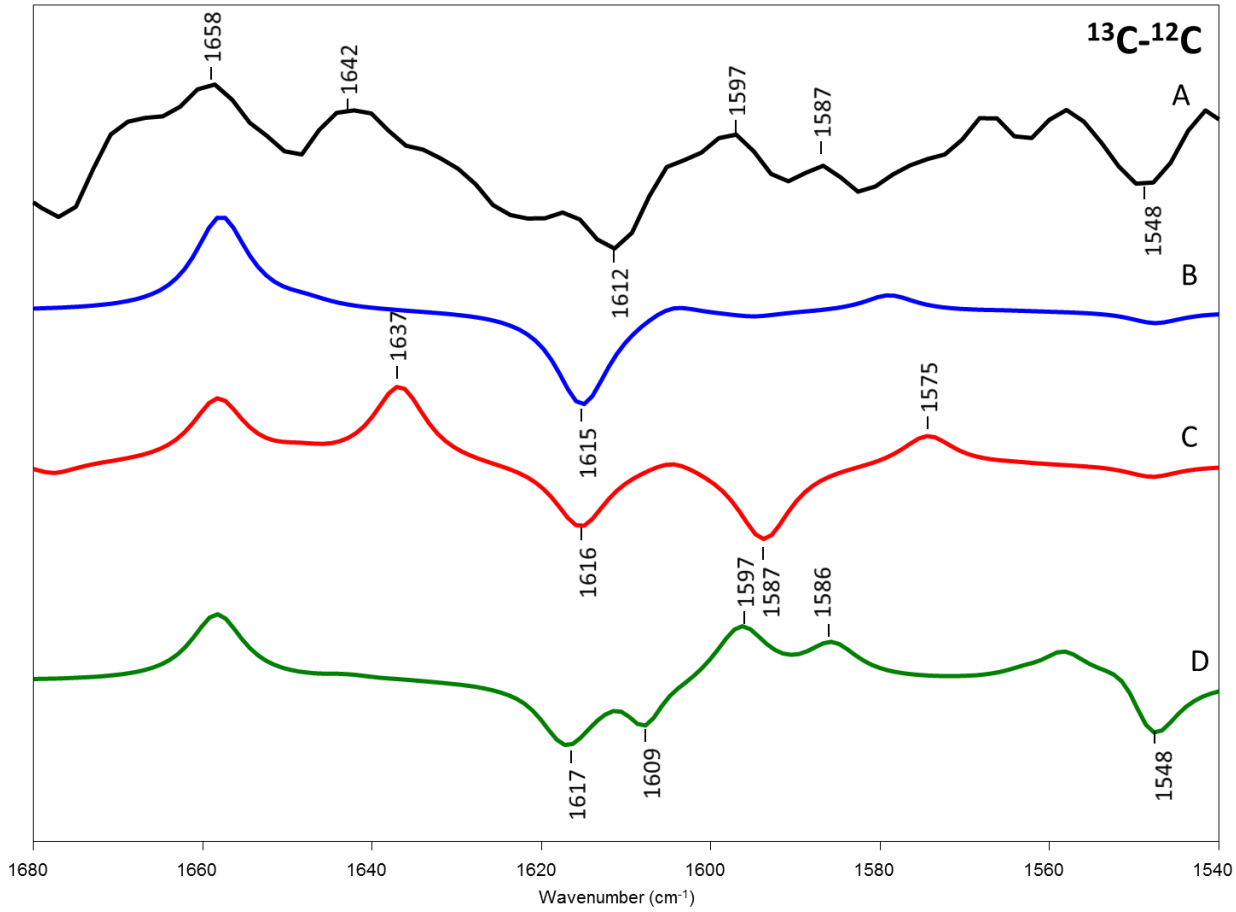

Figure 3.7 Experimental (A) and calculated (^{13}C-^{12}C) isotope edited FTIR DDS for neutral PhQ. (B) DFT calculation for isolated neutral PhQ in the gas phase. (C) DFT calculation for PhQ in the presence of a Leu residue. (D) ONIOM calculations for neutral PhQ in the A_1 binding site. Calculated normal mode frequencies were scaled by 0.963, 0.963 and 0.953, respectively.

3.4 Conclusion

We have incorporated unlabeled PhQ back into the A_1 binding site of fully ^{13}C labeled PS I particles from *men*B mutants. Coupling this experimental work with vibrational frequency calculations, some bands associated with PhQ or PhQ^- in the FTIR DDS are identified. This work further supports the band assignments obtained from previous studies. The band at 1654

cm^{-1}, which downshifts 28 and 46 cm^{-1} upon ^{18}O and ^{13}C labeling, is identified as C_1=O mode of the non H-bonded carbonyl group by OM/MM (ONIOM type) calculation. However, the assignment of 1495 cm^{-1} from ONIOM calculation is different from DFT based calculations. In ONIOM calculation, the band at 1495 cm^{-1} is mainly due to C_1⋯O mode of reduced PhQ. ONIOM calculations also suggest that the strong H-bond between PhQ and LeuA722 leads to C_4=O mode of the H-bonded carbonyl group downshifts ~60 and 80 cm^{-1} for neutral and reduced PhQ, respectively.

4 ON THE NATURE OF THE HYDROGEN BONDS TO NEUTRAL UBIQUINONE IN THE Q_A BINDING SITE IN PURPLE BACTERIAL PHOTOSYNTHETIC REACTION CENTERS

Abstract

The nature of hydrogen bonding to pigments in protein complexes is currently a topic of some debate. The debate centers on whether hydrogen bonds can be understood on purely electrostatic grounds, or whether they need to be considered quantum mechanically. This distinction is of current relevance, primarily because of the application of QM/MM computational methods to the study of biological problems. To address this problem we have used QM/MM methods to study the neutral state of the hydrogen bonded ubiquinone molecule termed Q_A that functions as an electron transfer cofactor in purple bacterial photosynthetic reaction centers. In these calculations we have treated the hydrogen bonding amino acids either quantum mechanically or using molecular mechanics methods. As a specific metric for comparing the different computational methods isotope edited FTIR difference spectra are calculated. The calculated spectra are in remarkable agreement with experimental spectra, and it is found that the calculated spectra are very similar when hydrogen bonding amino acids are treated using either QM or MM methods. The latter result suggests that hydrogen bonding to neutral ubiquinone in purple bacterial reaction centers can be considered in purely electrostatic terms, which is contrary to the widely held belief that the hydrogen bonding amino acids should be treated quantum mechanically. Natural bond orbital analysis is used to further verify that the hydrogen bonds are predominantly electrostatic in nature. Calculated bond lengths and vibrational frequencies of the N-H groups involved in hydrogen bonding are used to estimate the relative strengths of the hydrogen bonds to either UQ carbonyl group.

4.1 Introduction

Quinones play an important role in biological electron and proton transfer processes that occur in both respiration and photosynthesis [110]. In type II photosynthetic reaction centers two quinone molecules are bound to the protein subunits, and act as terminal electron acceptors [51]. The two quinones are often termed Q_A and Q_B. In this manuscript, however, we will refer to the quinone binding site as Q_A and Q_B.

In *Rhodobacter (Rb.) sphaeroides* purple bacterial reaction centers (PBRCs), ubiquinone-10 (UQ10) molecules occupy both the Q_A and Q_B binding sites. Although the UQ10 molecules occupying the Q_A and Q_B binding sites are identical, their functions are very different. The Q_A ubiquinone (UQ) is an intermediary cofactor involved in transferring electrons from bacteriopheophytin to Q_B [111], while the Q_B quinone couples proton and electron transfer processes [112].

The different functionalities of the Q_A and Q_B ubiquinones must arise from different pigment protein interactions that occur in each of the binding sites. Thus the study of the properties of the quinones that occupy the Q_A and Q_B binding sites will allow an assessment of how pigment protein interactions modulate cofactor function.

Fourier transform infrared (FTIR) difference spectroscopy has been widely used to study both the neutral and radical states of cofactors in a range of protein complexes [113, 114]. In particular light induced FTIR difference spectroscopy has been widely used to study both the neutral and reduced states of quinones in PBRCs [115]. Although Q_A^-/Q_A and Q_B^-/Q_B FTIR difference spectra (DS) have been obtained, they are difficult to interpret because many bands not associated with the quinones also contributed to the spectra. Reconstitution of PBRCs with

isotope labeled quinones, however, has allowed some separation of the contributions of the quinones from those of the protein in Q_A^-/Q_A and Q_B^-/Q_B FTIR DS [115].

In this manuscript we focus specifically on the ubiquinone (UQ) molecule that occupies the Q_A binding site in *Rb. sphaeroides* PBRCs. Although experimental Q_A^-/Q_A FTIR DS have been obtained under many sets of conditions, few computational studies aimed at modeling the experimental FTIR DS have been undertaken.

Calculations aimed at modeling the vibrational properties of quinones in the Q_A binding site must account for the protein environment. Quantum mechanical (QM) calculations of such a large molecular system are unfeasible. Methods have been developed, however, that allow one to separate the molecular system into distinct layers that can be treated at different levels of theory. In one layer the chemical properties of the principle species of interest (the pigment or cofactor) can be calculated using "high-level" QM methods. The surrounding protein environment is included but treated using computationally less expensive molecular mechanics (MM) methods [116].

Previously, we have undertaken QM:MM calculations for *neutral* UQ in the Q_A binding site using the ONIOM method [117]. ONIOM is an acronym for: our Own N-layered Integrated molecular Orbital + Molecular mechanics package [60, 118]. In these calculations only UQ was treated at the QM level, while all amino acids were treated using MM methods. Thus any QM effects of H–bonding are not considered.

Computational modeling of hydrogen bonding is a subject of much current interest [119, 120], and it is still a matter of debate as to whether H-bonds should be treated purely electrostatically or quantum mechanically [121]. In computational studies of UQ^- (singly reduced UQ) in the Q_A binding site [50, 122], it is common to consider H–bonding amino acids

at the QM level of theory. This seems appropriate since EPR data suggests the presence of spin density on (one of the) H-bonding amino acid side-chains. Little work has been undertaken to show/verify that such involved QM calculations are required for proper simulation of the EPR parameters of UQ^{-} in the Q_A binding site, however.

Unlike the case for UQ^{-}, for neutral UQ in the Q_A binding site there is no experimental evidence indicating whether H bonding amino acids should be treated using QM or MM methods. It is therefore necessary to compare the results from calculations in which amino acids that H-bond to neutral UQ in the Q_A binding site are treated using both QM and MM methods.

Here we extend upon our previous QM: MM (ONIOM) calculations by including several of the amino acids surrounding the UQ in the QM part of the calculation. In this more detailed computational approach we find that the calculated isotope edited FTIR difference spectra are similar to that obtained previously, where hydrogen bonding amino acids were treated using MM methods. This suggests that hydrogen bonding to the UQ molecule in the Q_A binding site is well modeled without the need for a detailed QM consideration of surrounding amino acids. The H–bonding amino acids can be effectively considered using MM methods, considerably decreasing the computational cost. Following on from this natural bond orbital analysis is used to estimate to what extent the H-bonds to UQ can be considered as electrostatic. Finally, the relative strength of H-bonds to UQ in the Q_A binding site is calculated.

4.2 Materials and Methods

4.2.1 Model Construction

All molecular models were constructed using the crystal structure of *Rb. sphaeroides* PBRCs at 2.2 Å resolutions [25] (PDB file 1AIJ). The initially constructed model includes all atoms within 10 Å of both UQ carbonyl oxygen atoms. The model constructed contains 49

amino acids. Hydrogen atoms are added (using Gaussview 4.0) and then optimized (using an appropriate level of theory) with all heavy atoms fixed. The protonation state of amino acid side chains (at neutral pH and room temperature), particularly Arg and Glu residues, was checked and adjusted (if necessary) prior to calculation.

4.2.2 Calculations

All calculations described here were undertaken using Gaussian03 software [91]. In all calculations the atoms of the protein backbone were fixed in position. Calculations were undertaken with the amino acid side chains both free and fixed. The UQ hydrocarbon tail was modeled as a single prenyl unit. Inclusion of further units did not alter the calculated spectra (not shown).

In previous [117] ONIOM geometry optimizations of the Q_A binding site, we treated only the ubiquinone molecule at the QM level, using the B3LYP functional and the 6-31G+(d) basis set. The molecular mechanics (MM) part of the ONIOM calculation was undertaken using AMBER (Assisted Model Building with Energy Refinement) [123], and only atoms of the protein backbone were constrained. Here we treat the UQ, the hydrogen bonding amino acids (AlaM260 and HisM219), the non-heme iron atom and its ligands (HisM266, HisL190, HisM230 and GluM234) (see Figure 4.1) at the QM level, while the MM layer atoms are treated using either the UFF (Universal Force Field [88]) or AMBER force fields. Atomic charges are calculated using both Mullikan population analysis (MPA) [124] and natural population analysis (NPA) [125].

For some calculations, following geometry optimization, natural bond orbital analysis [126, 127] was undertaken within the Gaussian03 software environment. All atoms in the QM layer are included in this analysis. The charge distribution from the MM layer is also included.

4.2.3 IR Spectral Simulation

Following geometry optimization of the protein-quinone system, all atoms in the model system (QM layer) are included in vibrational frequency calculations at the same level as that considered in geometry optimization. Calculated normal mode vibrational frequencies were obtained for unlabeled and isotope labeled UQ, and isotope edited double difference spectra are constructed, as described previously [117]. In the isotope edited double difference spectra nearly all of the calculated amino acid vibrational modes subtract out, and the calculated spectra are directly comparable to experimental FTIR isotope edited double difference spectra. The calculated spectra are scaled by a factor that is estimated by comparing the frequencies of bands in the calculated and experimental spectra.

4.2.4 Harmonic Normal Mode Vibrational Frequency Assessment

Assignment of calculated vibrational frequencies to molecular groups is based on a consideration of the calculated atomic displacements (in Cartesian coordinates) associated with the normal modes. These atomic displacements can be animated using software (GaussView), and the molecular groups that most prominently contribute to the normal modes can be assessed visually. In addition potential energy distributions of the normal modes of unlabeled and isotope labeled UQ are calculated using GAR2PED [128].

4.3 Results

4.3.1 UQ structure and numbering

Figure 4.1 shows the structure and numbering scheme of the heavy atoms of the model system (atoms treated at the QM level) used in ONIOM calculations. The hydrogen atoms

involved in H–bonding are also shown. There are 99 atoms (including hydrogen atoms) treated at the QM level in this model system.

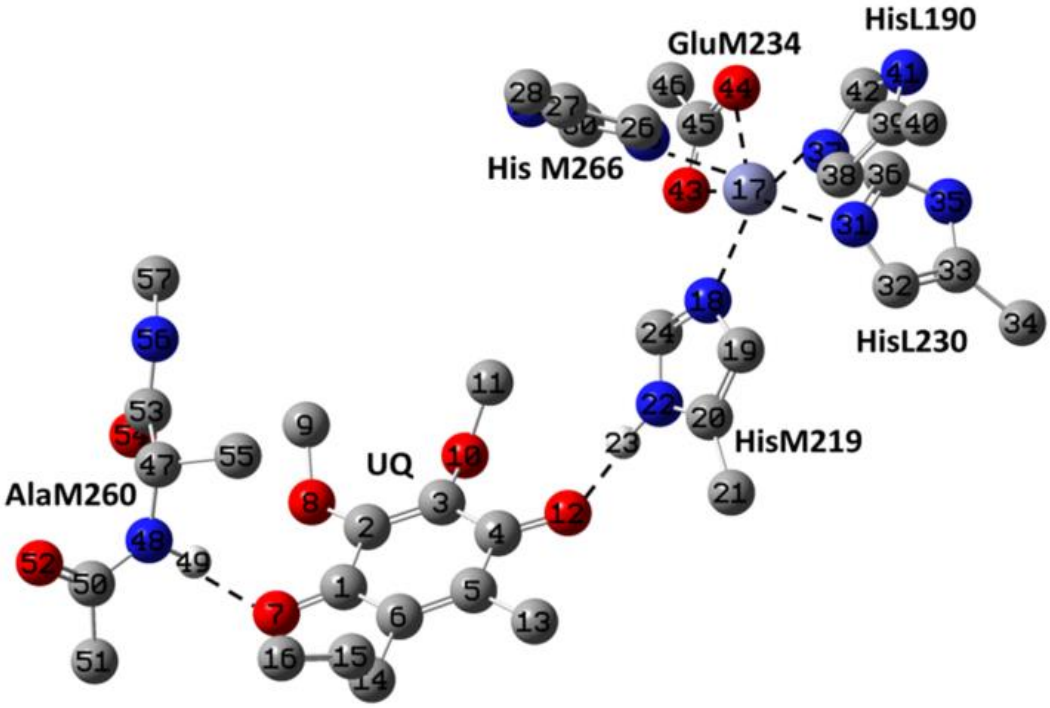

Figure 4.1Ball and bond structural model and numbering scheme of the heavy atoms comprising the QM layer in ONIOM calculations. The hydrogen atoms of the H bonding amino acids are also shown (atoms 23 and 49). Blue/red/grey/white/purple colored balls represent nitrogen/oxygen/carbon/hydrogen /iron atoms, respectively.

Table 4.1 Details and parameters used in the different ONIOM calculations.

	# Atoms **Model system**	**Fixed atoms**	**ONIOM** **Calculation**	**Charge** **Model system**	**Charge** **UQ**
1	31	Protein backbone and Fe	6-31+G(d):Amber 1,1, 0,1, 0,1	0	0
2	31	Protein backbone and Fe	6-31+G(d):UFF 1,1, 0,1, 0,1	0	0
3	99	All heavy atoms except UQ	6-31G(d)/LANL2DZ:UFF 0,2, 0,4, 0,4	0	-0.874
4	99	All heavy atoms except UQ	6-31G(d)/LANL2DZ:UFF 1,1, 1,5, 1,5	1	0.054
5	99	Protein backbone	6-31G(d)/LANL2DZ:UFF 1,1, 1,5, 1,5	1	0.047

For the DFT part of the ONIOM calculations the B3LYP functional was used. The atomic charges (in units of e) listed were calculated using NPA. The "real system" is defined as all of the atoms in both the QM and MM layers. The "model system" is defined as only the QM layer atoms. The series of six numbers in the ONIOM calculation column refer to the charge and multiplicity of the real and model systems. For example, the series of numbers (1,1 1,5, 1,5) in calculations 4 and 5 refer to the charge and multiplicity of: 1/ the real system at the MM level of theory (1,1); 2/ the model system at the QM level of theory (1,5); 3/ the model system at the MM level of theory (1,5).

4.3.2 Calculations Undertaken

In previous ONIOM calculations [ONIOM (B3LYP/6-31G+ (d): AMBER)] only the UQ molecule was treated using QM methods (31 atoms). Electronic embedding [118, 129, 130] was employed. This procedure is referred to as calculation 1 in Table 4.1.

To test if the type of MM layer calculation employed could impact the calculated results we have undertaken an ONIOM (B3LYP/6-31G+ (d): UFF) calculation (MM layer charges generated using the qEq method). This is calculation 2 in Table 4.1. In calculation 2, as in calculation 1, only the UQ molecule (31 atoms) is treated at the QM level.

To further develop our computational approach we treat UQ and several of the surrounding amino acids, as well as Fe, at the QM level. There are 99 atoms (including hydrogen atoms) in the model system (Figure 4.1). For this larger model system all atoms except Fe were treated using the 6-31G(d) basis set, and the Fe atom is treated separately using the LANL2DZ basis set [131]. This basis set treats the inert core electrons (of transition metals) simply as an electrostatic potential. All heavy atoms, except those of UQ, are fixed in position, and the total charge of the 99 atoms in the QM level is set to zero (calculation 3 in Table 4.1). The high spin (S=2) state of Fe is also chosen [132, 133] (multiplicity of the model system is 4). In calculation 3 upon optimization, the NPA calculated charge on the UQ atoms is -0.874. A similar result was obtained using MPA (not shown). For the model system with a multiplicity of 2, with Fe treated using the 6-31G (d) basis set, the NPA calculated charge on the UQ is -0.865 (calculation 3A in Table 4.4). In calculations 3 and 3A UQ has significant anionic character.

Calculation 4 is similar to calculation 3 except that the total charge of the 99 atoms in the model system is set to +1. This setting is appropriate because Fe has a charge of +2 and GluM234 has a charge of -1. In calculation 4, as in calculation 3, all heavy atoms, except those of UQ, are constrained. The Fe atom is in the high spin state and is treated using the LANL2DZ basis set. In calculation 4, upon optimization, the NPA calculated charge on the UQ atoms is +0.054 (Table 4.1). If the Fe atom in the high spin/low spin state is treated using the 6-31G (d) basis set the charge on the UQ atoms is calculated to be +0.055/+0.057 (Calculation 4A/4B in Table 4.4). So the precise spin state of Fe and the use of the LANL2DZ basis set do not appear to be important, at least in terms of the NPA calculated charge on the atoms of UQ. There is some discrepancy in the MPA calculated charge on UQ in calculations 4 and 4A (Table 4.4). It

is well known that MPA calculated charges can depend on the basis set used [125]. This basis set dependence is usually less pronounced for NPA calculated charges, however.

Calculation 5 is the same as 4, except now the amino acid side chains are not constrained. Calculation 5 is computationally very expensive compared to calculation 4.

4.3.3 Calculated Geometric Parameters

Table 4.2 compares geometric parameters obtained from calculations 1-5 with that from various X-ray structures. For calculation 3, the C=O bonds are considerably longer than that found in the other calculations. This is consistent with the anionic character of UQ in calculation 3.

Table 4.2 Comparison of calculated and experimental bond lengths and angles

Calculation	**1**	**2**	**3**	**4**	**5**	**X-ray**
C_1=O	1.227	1.225	1.272	1.229	1.229	
C_4=O	1.238	1.235	1.282	1.238	1.238	
Ala H-O_1	1.89	2.29	1.80	1.99	2.02	1.94±0.11
Ala N-O_1	2.84	3.16	2.81	2.90	2.93	2.79±0.09
∠Ala N-H-O_1	153	140	165	148	147	147±8
His H-O_4	1.85	2.37	1.68	1.89	1.99	1.79±0.11
His N-O_4	2.87	3.36	2.72	2.90	2.99	2.80±0.15
∠HisN-H-O_4	176	159	174	169	166	170±6

The X-ray data are averages obtained from several crystal structures [122, 134].

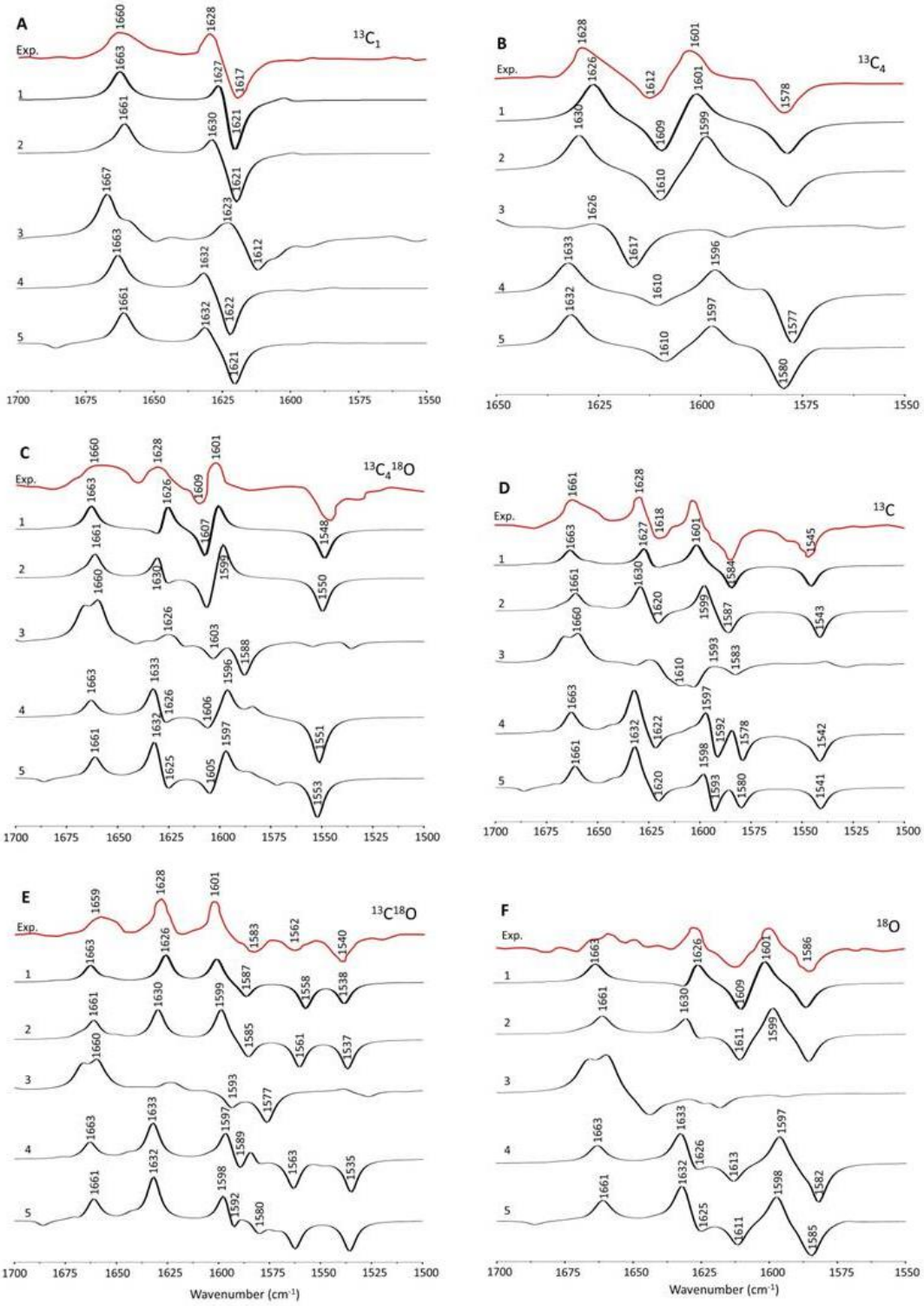

Figure 4.2 Experimental (red) and ONIOM calculated (black) Q_A^-/Q_A isotope edited DDS for neutral UQ. UQ has been specifically (A) $^{13}C_1$, (B) $^{13}C_4$, (C) $^{13}C_4{}^{18}O$, (D) ^{13}C, (E) $^{13}C^{18}O$ and (F) ^{18}O isotope labeled. For ^{18}O labeling, only the carbonyl oxygen atoms are labeled. Experimental spectra are reprinted with permission from references [47] and [109]. In calculations 1-5 spectra have been scaled by 0.9718, 0.9634, 1.0842, 0.9638 and 0.9637, respectively.

In all calculations, the C_1=O bond is shorter than the C_4=O bond. This may be a reflection of an asymmetry in the H–bonding to the UQ carbonyl groups. In calculations 1, 4 and 5 the calculated geometric parameters are in excellent agreement with that derived from a consideration of several X-ray structures. In calculation 2, however, the H–bonds to the UQ C=O groups are considerably longer than that found in calculations 1, 4 and 5. The H–bond angles are also considerably altered in calculation 2. It appears that following geometry optimization in calculation 2, the UQ is somewhat rotated in the Q_A binding site. Calculation 2 poorly models the crystal structure data, and is not in keeping with calculations 1, 4 and 5.

4.3.4 Calculated Isotope Edited Difference Spectra.

Figure 4.2 shows ONIOM calculated (black) isotope edited double difference spectra for neutral UQ in the Q_A binding site for all five calculations. Experimental spectra are also shown (red). The spectra in Figure 4.2A-F are for six different types of specific UQ isotope labeling.

Calculations 1 and 2 yield virtually identical isotope edited difference spectra. Thus the type of MM force field employed (AMBER or UFF) in the ONIOM calculations (with only UQ treated at the QM level) is not important, at least in terms of simulating isotope edited FTIR difference spectra. This is in spite of the differences in the geometric parameters found in calculations 1 and 2 (Table 4.2).

The spectra obtained from calculation 3 do not resemble the experimental spectra. The bands in the spectra from calculation 3 are roughly 180 cm^{-1} lower in frequency than the bands in the spectra for the other calculations (note the differing frequency scaling factor for calculation 3). Such a large downshift is expected for a UQ anion radical, so the spectra obtained in calculation 3 also indicate a considerable negative charge on UQ.

The spectra derived in calculation 4 and 5 are very similar to that from calculations 1 and 2. Thus the additional computational expense for calculations 4 and 5 (especially for calculation 5) is unnecessary. The spectra obtained from calculation 4 are virtually identical to that obtained from calculations for both high and low spin model systems with Fe treated using the 6-31G(d) basis set (not show, but see calculation 4, 4A and 4B in Table 4.4).

4.4 Discussion

All of the calculated spectra presented here relate to the neutral state of UQ in the Q_A binding site. It is possible to undertake corresponding calculations for UQ^{-}, and compare the conclusions derived from these calculations with conclusions derived from calculations that simulate the EPR properties of UQ^{-}. Such calculations and comparisons are currently underway in our lab.

4.4.1 Assignment of Bands in the Calculated and Experimental Spectra

The positive bands in the isotope edited difference spectra in Figure 4.2 are due to vibrational modes of unlabeled UQ, while the negative bands are due to isotope labeled UQ. Figure 4.2 demonstrates that the spectra obtained for calculations 1 and 2 are very similar, the main difference being a slight shift in a positive band near 1626 cm^{-1} in calculation 1, to ~1630 cm^{-1} in calculation 2. In calculations 4 and 5 this band is upshifted further to ~1633 cm^{-1}. This band frequency shift between calculations is most easily seen in Figure4.2E, where positive bands due to modes of unlabeled UQ do not overlap with negative bands due to modes of the $^{13}C^{18}O$ labeled UQ ($^{13}C^{18}O$ isotope induced frequency shifts are in excess of 65/80 cm^{-1} for C=C/C=O modes, respectively).

Below we will refer to positive and negative difference bands using (+) and (-) symbols, respectively. The differences in the spectra for calculations 1, 2, 4 and 5 are best visualized in

Figure 4.2C and F, where a 1630(-)/1626(+) cm^{-1} feature in calculation 1 becomes a 1630(+)/1626(-) cm^{-1} feature in calculation 2 and the 1633(+)/1626(-) cm^{-1} feature in calculations 4 and 5. The potential energy distributions (PEDs) of the normal modes that contribute to the bands in the calculated spectra were presented previously for calculation 1 [117] and very similar results are obtained for calculation 2, 4 and 5. For calculation 1, the positive bands at ~1626 and 1663 cm^{-1} are due predominantly to C_4=O and C_1=O vibrations of unlabeled UQ, respectively [117]. In Figure 4.2C ($^{13}C_4{}^{18}O$ labeling) the C_1=O mode at 1663 cm^{-1} downshifts 33 cm^{-1} to 1630 cm^{-1}, while the C_4=O mode at 1626 cm^{-1} downshifts 78 cm^{-1} to 1548 cm^{-1}. These shifts give rise to the 1630(-)/1626(+) cm^{-1} feature in the spectra for calculation 1 in Figure 4.2C. For calculation 2 the C_1=O mode is at 1661 cm^{-1} and downshifts 35 cm^{-1} to 1626 cm^{-1}, while the C_4=O mode at 1630 cm^{-1} downshifts 80 cm^{-1} to 1550 cm^{-1}. These shifts give rise to the 1630(+)/1626(-) cm^{-1} feature in the spectra for calculation 2 in Figure 4.2C. Thus the differences in the calculated spectra are explained in terms of small changes in band frequencies (<4 cm^{-1}) and in isotope induced frequency shifts (<2 cm^{-1}) of the same normal modes in the different calculations.

4.4.2 Comparison of spectra obtained in the different calculations

The spectra obtained in calculations 4 and 5 are very similar. If the goal is an adequate simulation of experimental isotope edited FTIR DS, then relaxing the constraints on atoms of the amino acid side chains in the molecular model does not appear to offer any advantage.

The spectra obtained in calculations 1, 2, 4 and 5 are very similar. This is in spite of the considerable additional computational expense necessary for calculations 4 and 5 (especially for calculation 5). From the similarity in the spectra in calculations 1, 2, 4 and 5, at least two points can be made:

Firstly, if the goal is an adequate simulation of experimental isotope edited FTIR DS then there is no need to consider any of the surrounding amino acids (or the Fe atom) at the QM level. This point provides a strong justification for the methodological approach taken in our previous ONIOM calculations [117]. In contrast, in previous ONIOM calculations aimed at modeling some of the magnetic spectroscopic parameters of UQ^{-} in the Q_A binding site [50], it was indicated that the metal atom should be treated using QM. No calculations were undertaken with the metal atom treated using MM methods to test this, however. In order to contrast and compare the magnetic spectroscopic computational result we are currently in the process of calculating isotope edited FTIR difference spectra for UQ^{-} in the Q_A binding site with the metal atom being treated using both QM and MM methods.

Secondly, if the goal is an adequate simulation of experimental isotope edited FTIR DS, and computational resources dictate that only the pigment of interest can be treated at the QM level of theory, then it does not appear to be important which of the MM force fields (AMBER or UFF) is chosen. However, the UFF method leads to an alteration of the structural parameters (Table 4.2) that do not appear to be in agreement with the other calculations or the X-ray data. Based on these results we suggest that if one wishes to treat only the pigment of interest at the QM level, with protein amino acids treated using MM methods, then the AMBER method is a better choice than the UFF method. However, if several amino acids are to be included in the QM treated model system, then the choice of MM force field (UFF or AMBER) is not important. In our studies the UFF approach is simpler to implement, and is thus preferred in calculations involving larger model systems.

In ONIOM calculations for the larger model system the spin state of the Fe atom appears not to be of importance, both in terms of the calculated charge on the UQ (calculation 4 and 4B

in Table 4.4), and for simulating isotope edited difference spectra. In the FTIR experiments undertaken to produce the isotope edited FTIR difference spectra the spin state of the Fe atom was not specified. It has been found recently that the Fe atom in *Rb. sphaeroides* reaction centers can exist in both the high and low spin forms [133]. Our calculations predict, however, that the spin state of the Fe atom would have little or no impact on the calculated isotope edited FTIR difference spectra.

4.4.3 Comparison with results obtained in different computational studies

Very recently, Chernov et al. [135] have undertaken DFT calculations using a model of the Q_A binding site that contained UQ, Fe and the amino acids that provide ligands (four histidines and one glutamate), and a water molecule. The peptide backbone of an alanine residue that may be involved in hydrogen bonding was not included (Chernov et al. were focused on the properties of the bidentate ligand to the Fe atom provided by glutamate, and not on quinone H-bonding). In these studies they calculate that the charge on neutral UQ is -0.19 to -0.22 (a charge of -0.09 to -0.19 was also calculated for the neutral plastoquinone in the Q_A site in photosystem II). If the charge on the UQ is ~ -0.2 then any calculation of isotope edited difference spectra using this model would result in spectra that do not resemble the experimental spectra. The error most probably arises because MPA rather than NPA was used to calculate the UQ atomic charges (compare MPA and NPA calculated charges on UQ in calculation 4A in Table 4.4).

Recently, computational studies of small H–bonding molecular dimers have been undertaken which show that treating one of the monomers using QM and the other using MM gave results that were the same as that found when both molecules were treated using QM [136, 137]. These studies on molecular dimers support the validity of the calculations presented here, and indicate that QM/MM potentials can be as effective as pure QM potentials.

The calculations outlined here indicate that H–bonding to neutral UQ in the Q_A binding site can be understood (modeled) in purely electrostatic terms, without consideration of quantum effects. Whether H–bonding needs to be treated at the QM level [138] or not [121, 139] in other systems is an area of ongoing research.

4.4.4 Electronic embedding vs. Mechanical embedding

In previous ONIOM calculations of the magnetic properties of UQ^{-} in the Q_A binding site it was shown that the ONIOM calculations using mechanical embedding (ME) were just as effective (in terms of calculation of spin density distributions and hyperfine coupling constants for UQ^{-}) as calculations undertaken using electronic embedding (EE) [50].

The differences between ME and EE have been discussed [116, 130]. Briefly, in EE the electric potential generated by the atomic charges in the MM layer are included in the QM Hamiltonian. This leads to a more realistic situation in which the MM layer charges can polarize the QM layer. The QM layer charges do not polarize the MM layer charges, however. In ME the interaction between the QM and MM layers is treated using MM. This does not allow for polarization of the QM layer, as MM methods are parameterized in terms of fixed (unpolarizable) point charges.

All five of the calculations in Table 4.2 were undertaken using EE. We have also undertaken calculation 1 using ME instead of EE, and Figure 4.3 in the supplementary information section compares isotope edited spectra obtained for calculation 1 using ME and EE. Figure 4.3 demonstrates that calculated spectra using ME poorly model the experimental spectra. In fact the spectra, the normal mode compositions, and the isotope induced frequency shifts calculated using the ME approach all resemble that calculated for UQ in the gas phase [117].

Thus it appears that the electrostatic environment of neutral UQ in the Q_A binding site leads to some polarization of the QM atoms, which requires an EE ONIOM approach to model correctly.

4.4.5 Quantitative measures of H-bond strength

In Table 4.2, the C_4=O bond is found to be 0.01 Å longer than the C_1=O bond. This could be considered to be a reflection of some asymmetry in the H–bonding to the UQ carbonyl groups. However, from studies of UQ in the gas phase, the C_1=O and C_4=O groups are also found to differ by ~0.01 Å [140]. So the C=O bond lengths do not provide a good measure of the strength of H–bonding to the UQ carbonyl groups. In studies of small H–bonding clusters [141] it was also found that the C=O bond length is a poor measure of H-bond strength.

For N–H - - - O type H–bonds, the H - - - O distance (also listed in Table 4.2) was also found to be a poor measure of H–bond strength [141, 142]. The N–H bond length has been found to correlate very well with H–bond strength, however [142, 143]. The N–H bond lengths of the various histidine imidazole groups, and the AlaM260 backbone, used in our model (Figure 4.1) are listed in Table 4.2.

IR spectroscopy is frequently used for testing the strength of H–bonds. In many cases, upon H–bonding the vibrational frequency of the proton donating moiety red-shifts, usually by several hundred cm^{-1}, and the intensity of the vibration increases several fold [144]. The red-shift of the N–H vibrational stretching frequency can be correlated with other parameters such as the bond length and the strength of the H–bond [143]. For the N–H groups of HisM219 and AlaM260 the bonds lengthen and the N–H vibrational mode frequencies decrease, compared to non H–bonded imidazole N-H groups (Table 4.3). The H–bonds provided by the N–H groups of HisM219 and AlaM260 are classic “red-shifted” H–bonds [145]. The N–H mode of HisM219

downshifts more and gains considerably more in intensity that the N–H mode of AlaM260 (Table 4.3), suggesting that the HisM260 H–bond is stronger than the AlaM260 H-bond.

Table 4.3 Bond lengths, vibrational mode frequencies and intensities of the H-bonding N–H groups of histidine and alanine obtained from calculation 5.

Bond	r_{N-H}	**Mode Intensity**	**Mode Frequency**
N29–H, HisM266	1.00691	75	3687
N41–H, HisL190	1.00978	112	3657
N35–H, HisM230	1.01076	83	3642
N48–H, AlaM260	1.01290	225	3583
N22–H, HisM219	1.01543	1195	3554

Atomic numbering as in Figure 4.1. Bond length in Å, intensity in km/mol, frequency in cm^{-1}.

The parameter, δ_{N-H}, defined in equation 1 below, has been shown to correlate very well with H–bond strength [142, 143], where r_{N-H} is the length of the N–H bond in the H–bonded system and r^0_{N-H} is the length of the free N–H bond, not involved in H–bonding.

$$\delta_{N-H} = \frac{(r_{N-H} - r^0_{N-H})}{r^0_{N-H}}$$

If it is assumed that the non-ligated N-H groups of HisL230, HisM266 and HisL190 are representative of free N-H groups, then using the data in Table 4.3 with r^0_{N-H} = 1.00915, we find δ_{N-H} = 6.223 x 10^{-3} and 3.716 x 10^{-3} for the HisM219 and AlaM260 N–H groups, respectively. This suggests that the HisM219 H–bond is 1.67 times stronger than the AlaM260 H–bond. By considering a similar equation for N–H vibrational frequencies, with a free N-H vibrational frequency of 3662 cm^{-1}, then using the data in Table 4.3, we find that the HisM219 H–bond is 1.37 times stronger than the AlaM260 H–bond. Averaging the results for both calculations we estimate that the HisM219 H–bond is about a factor of 1.52 stronger than the AlaM260 H–bond.

Two points should be noted in the above analysis. Firstly, in order to estimate the relative H–bond strengths from calculated vibrational frequencies, it is necessary to undertake ONIOM calculations with the H–bonding amino acids included at the QM level of theory. Thus calculations 1 and 2 could not be used for this purpose.

Secondly, the data in Table 4.3 indicate that the backbone N-H group of AlaM260 is H-bonded to UQ, albeit weakly. In IR spectroscopy the UQ C=O mode vibrational frequency is often used to give a qualitative measure of H–bond strength. Thus the UQ C_4=O group is more strongly H–bonded than the C_1=O group because it's vibrational frequency is at 1626 cm^{-1}, compared to ~1660 cm^{-1} for the C_1=O group [47]. However, the UQ C_1=O and C_4=O mode vibrational frequencies cannot be used to give a measure of relative H-bond strength because the vibrational frequency of the C_1=O group of UQ in the protein binding site is the same as that found for UQ in solution. This frequency similarity suggests no H–bonding to the UQ C_1=O group. So, if H-bonding is relatively weak, then properties of the N-H group involved in H-bonding, rather than the C=O group, are a better indicator of H-bond strength. Unfortunately, experimental vibrational frequencies for the His N-H groups involved in H-bonding to UQ are unavailable.

4.4.6 The electrostatic nature of the H-bonds to UQ

Many factors have been proposed to contribute to and account for H–bond stabilization energy [144, 146, 147]. The H–bond stabilization energy for the type of H–bonds studied here (red-shifted H–bonds with a proton accepting oxygen atom and proton donating N–H group) is usually dominated by electrostatics, with a smaller charge transfer (sometimes called covalent or hyperconjugative) contribution [144, 147]. The charge transfer contributions to the H–bond energy in our ONIOM calculations can be estimated using the natural bond orbital, second order

perturbation theory method [126, 127, 148]. Charge transfer interaction energies of ~3–5 kcal/mol indicate that charge transfer contributes negligibly to H–bonding [126, 127]. In calculation 5 we calculate charge transfer interaction energies of the H–bonds at O_1 and O_4 of 3.79 and 3.84 kcal/mol, respectively (see the supplementary information section for more details). Similar results are found for calculation 4. Thus charge transfer contributions to the H–bonds of UQ in the Q_A binding site are very small, suggesting that the H–bonds to UQ in the Q_A site are dominated by electrostatic interactions. This conclusion is in line with previous suggestions that N-H···O type H-bonds are predominantly electrostatic in nature [149].

The conclusion from natural bond orbital analysis, that the H–bonds to UQ are mainly electrostatic in nature may provide an explanation as to why the procedures outlined for calculations 1, 4 and 5 (Table 4.2) all lead to a successful description of the experimental isotope edited difference spectra.

Calculation of the vibrational properties of neutral UQ (presented here) indicates that H-bonding amino acids are adequately treated using MM methods. In contrast, calculation of the EPR properties of UQ^{-} indicates that H-bonding amino acids need to be treated using QM methods [50, 122]. Taken together these results indicate differences in the nature of H-bonding for the neutral and anion UQ species. Changes in H-bonding upon radical formation may be a mechanism for stabilizing/destabilizing cofactors to promote/inhibit/fine-tune electron transfer processes in biological systems. To investigate this intriguing topic further it will be useful to undertake calculations similar to that presented here (modeling isotope edited FTIR difference spectra) for UQ^{-} in the Q_A binding site, and compare the findings to that obtained for calculations of the EPR properties of UQ^{-}.

4.5 Conclusions

ONIOM (QM/MM) calculations, with H–bonding amino acids treated at the MM level, give calculated isotope edited difference spectra that are similar to that obtained in ONIOM (QM/MM) calculations where the H–bonding amino acids are treated at the QM level. Thus quantum effects associated with H–bonding to neutral Q_A are negligible.

The H–bond to the UQ C_4=O group (provided by the side chain N–H group of HisM219) is about 1.5 times stronger than the H–bond to the UQ C_1=O group (provided by the backbone N–H group of AlaM260).

For ONIOM calculations of UQ in the Q_A binding site, if only the cofactor is treated at the QM level, with the protein environment treated at the MM level, then the AMBER force field is preferable (to the UFF force field) for the MM part of the calculation. This seems reasonable since the AMBER force field was designed with protein systems in mind. If H–bonding amino acids are treated at the QM level then the choice of AMBER or UFF force fields is unimportant.

In the ONIOM calculations described here an electronic embedding scheme (rather than mechanical embedding) is required for accurate simulation of the experimental spectra.

The ONIOM calculated charge on UQ in the Q_A binding site, as well as the calculated isotope edited difference spectra, are not sensitive to the spin state of the non-heme iron atom.

In terms of simulating isotope edited difference spectra, relaxing constraints on the atoms of amino acid side chains during optimization does not appear to offer any advantage.

4.6 Supporting Information

Table 4.4 Charge and spin on Fe and UQ obtained from several ONIOM calculations. Atomic charges were calculated using both NPA and MPA.

Calc	QM atoms	Fixed atoms	ONIOM Calculation	Charge Model system	Charge UQ NPA	Charge UQ MPA	Charge Fe NPA	Charge Fe MPA	Spin Fe
1	31	Protein backbone and Fe	6-31+G(d):Amber 1,1, 0,1, 0,1	0	0	0		2	
2	31	Protein backbone and Fe	6-31+G(d):UFF 1,1, 0,1, 0,1	0	0	0		0.933	
3	99	All heavy atoms except UQ	6-31G(d)/ LANL2DZ:UFF 0,2, 0,4, 0,4	0	-0.874	-0.790	1.456	0.581	3.738
3A	99	All heavy atoms except UQ	6-31G(d):UFF 0,2, 0,2, 0,2	0	-0.865	-0.799	1.378	1.053	0
4	99	All heavy atoms except UQ	6-31G(d)/ LANL2DZ:UFF 1,1, 1,5, 1,5	1	0.054	0.078	1.393	0.579	3.740
4A	99	All heavy atoms except UQ	6-31G(d):UFF 1,1, 1,5, 1,5	1	0.055	-0.112	1.545	1.175	3.952
4B	99	All heavy atoms except UQ	6-31G(d):UFF 1,1, 1,1, 1,1	1	0.057	0.074	1.298	1.000	0
5	99	Protein backbone	6-31G(d)/ LANL2DZ:UFF 1,1, 1,5, 1,5	1	0.047	0.077	1.449	0.634	3.740

4.6.1 Comparison of isotope edited difference spectra obtained from ONIOM calculations employing mechanical and electronic embedding

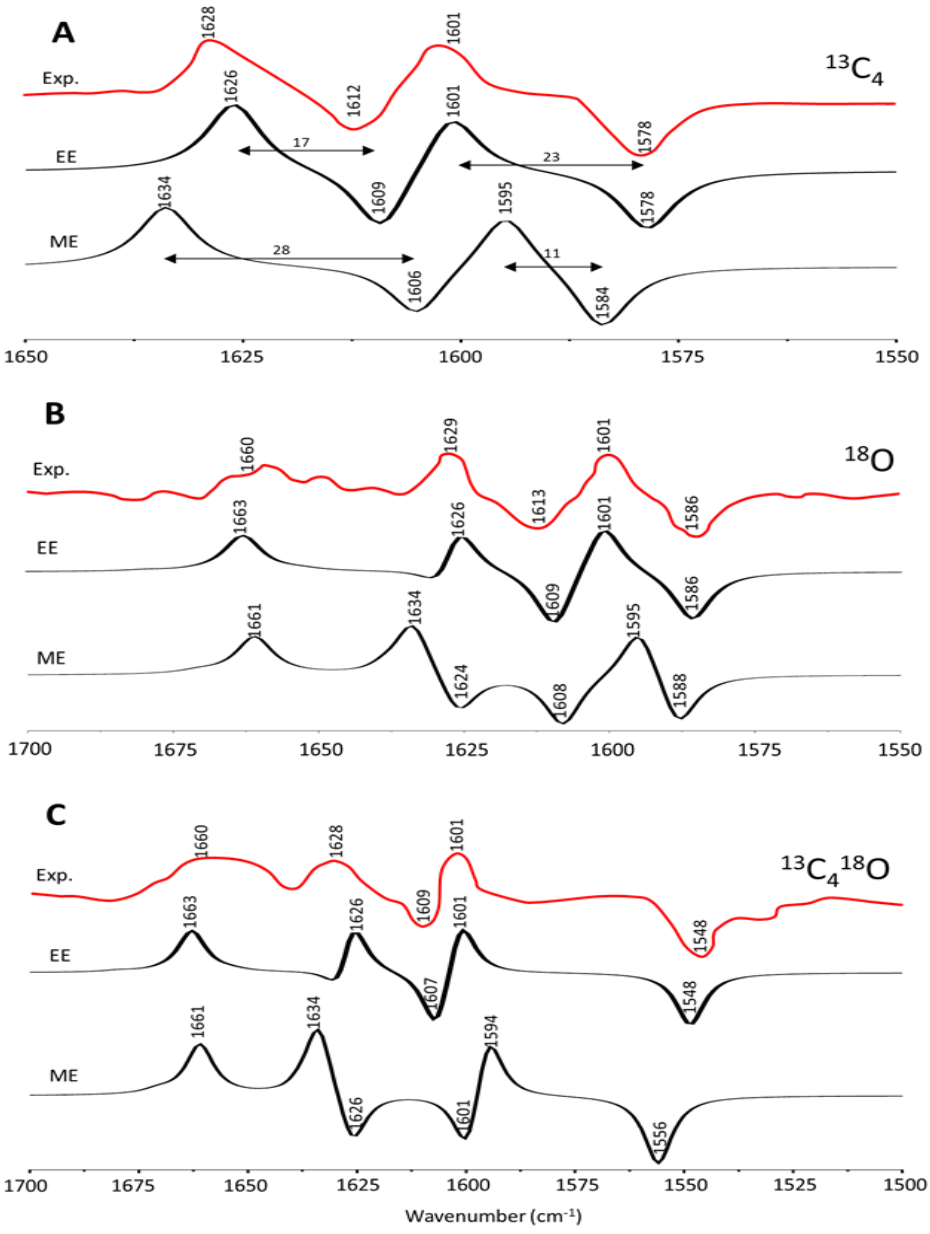

Figure 4.3 Experimental (red) and ONIOM calculated (black) isotope edited DDS for neutral UQ. UQ has been specifically (A) $^{13}C_4$, (B) ^{18}O and (C) $^{13}C^{18}O$ isotope labeled (only the carbonyl oxygen atoms are ^{18}O labeled). Experimental spectra are reprinted with permission from [47]and [109].

Figure 4.3 compares isotope edited difference spectra obtained from ONIOM calculations employing ME and EE (using the same approach as calculation 1 in Table 4.2). The spectra

obtained using ME clearly differ from that obtained using EE, and from that obtained experimentally. For example, in Figure 4.3A, the separation between the positive and negative bands is 17 and 23 cm^{-1} for EE, compared to 28 and 11 cm^{-1} for ME. The spectra calculated using the ME ONIOM approach appears to be very similar to the spectra calculated for UQ in the gas phase (see Table 1 in reference 19).

The composition of the normal modes that are associated with the bands in the spectra in Figure 4.3, obtained using the ME and EE approaches, are listed in Table 4.5, for unlabeled and $^{13}C_4$ labeled UQ in the Q_A binding site. For the ONIOM approach employing ME, the composition of the normal, and the isotope induced frequency shifts of the modes (Table 4.5), are very similar to that found in calculations of UQ in the gas phase (see Table 1 in (19)) and, as was pointed out previously, calculated spectra for UQ in the gas phase do not resemble the experimental spectra.

In summary, the ONIOM approach employing ME gives results that are essentially the same as that found for calculations of UQ in the gas phase, and the calculated spectra poorly resemble the experimental spectra. These observations suggest that calculations employing ME are not well suited, for modeling isotope edited difference spectra associated with UQ in the Q_A binding site, and the ONIOM calculations employing ME are clearly inferior to calculations employing EE.

Table 4.5 Normal mode frequencies, intensities, and potential energy distributions (PEDs) obtained from ONIOM calculations employing ME and EE, for unlabeled and $^{13}C_4$ labeled neutral UQ_1.

ONIOM-EE						
Unlabeled			**$^{13}C_4$**			
ν	**Intensity**	**Potential energy Distribution**	**ν**	**Intensity**	**Potential energy distribution**	**Δν**
1679	12	$C=C_t$ (66%)	1679	11	$C=C_t$ (66%)	0
1663	185	$C_1=O$ (81%)	1663	200	$C_1=O$ (82%)	0
1653	26	$C_5=C_6$ (45%), $C_2=C_3$ (19%)	1653	23	$C_5=C_6$ (45%), $C_2=C_3$ (19%)	0
1626	305	$C_4=O$ (68%), $C_2=C_3$ (9%)	1579	258	$C_4=O$ (71%), $C_2=C_3$ (6%)	47
1601	275	$C_2=C_3$ (35%), $C_5=C_6$ (18%) $C_4=O$ (14%), C_2-O (7%)	1609	276	$C_2=C_3$ (38%), $C_5=C_6$ (19%) $C_4=O$ (9%), C_2-O (10%)	-8
ONIOM-ME						
1671	19	$C=C_t$ (65%)	1671	19	$C=C_t$ (65%)	0
1661	177	$C_1=O$ (80%)	1661	188	$C_1=O$ (80%)	0
1640	37	$C_5=C_6$ (39%), $C_2=C_3$ (26%)	1640	37	$C_5=C_6$ (39%), $C_2=C_3$ (27%)	0
1634	264	$C_4=O$ (77%)	1584	276	$C_4=O$ (53%), $C_2=C_3$ (16%) $C_5=C_6$ (9%)	50
1594	260	$C_2=C_3$ (36%), $C_5=C_6$ (26%) C_2-O (7%), C4=O (6%)	1605	223	$C_4=O$ (28%), $C_2=C_3$ (23%) $C_5=C_6$ (20%), C_2-O (6%)	-11

Frequency in cm^{-1} and intensity in km/mol.

4.6.2 Charge transfer contributions to H–bond energy

The natural bond orbital (NBO) second order perturbation theory method can provide information on donor-acceptor orbital interaction energies [126]. The charge transfer interaction energy can be expressed as $E^{(2)} = \Delta E_{ij} = -n^{\sigma} F_{ij}^2 / (E_j - E_i)$, where n^{σ} is the donor orbital occupancy, $F(i, j)$ is the off-diagonal NBO Fock matrix element, and E_i and E_j are the donor and acceptor orbital energies [126, 127].

To gain a more detailed understanding of the origins of the red-shifted N_{48}-H$\cdots$O and N_{22}-H$\cdots$O H-bonds, NBO analysis has been carried out at the B3LYP/6-31G(d) level for calculation 5.

In the following BD* denotes an σ^* antibonding orbital; LP (1) and LP (2) denotes the two lone pair electrons.

For the AlaM260 (N_{48}-H) H-bond, there is an increase in the antibonding orbital occupancy n^{σ^*}, mainly caused by the two pairs of intermolecular donor-acceptor orbital interactions: LP(1)O_1→BD*(N_{48}-H) and LP(2)O_1→BD*(N_{48}-H). These interaction energies are 2.06 and 1.73 kcal/mol, respectively. Thus, in calculation 5, the overall charge transfer interaction energy of the H–bond at O_1 is 3.79 kcal/mol.

For the HisM219 (N_{22}-H) H-bond there is an increase in the σ^* antibonding orbital occupancy, that arises primarily from LP(1)O_4→BD*(N_{22}-H) and LP(2)O_4→BD*(N_{22}-H). The charge transfer interaction energies are 3.62 and 0.22 kcal/mol, respectively, and the total charge transfer interaction energies of the H–bond to O_4 is 3.84kcal/mol.

As indicated in the text, an orbital interaction energies of 3-4 kcal/mol is considered very small, and UQ H-bonds are negligibly covalent.

5 COMPARISON OF CALCULATED AND EXPERIMENTAL ISOTOPE EDITED FTIR DIFFERENCE SPECTRA OBTAINED USING PURPLE BACTERIAL PHOTOSYNTHETIC REACTION CENTERS WITH DIFFERENT QUINONES INCORPORATED INTO THE Q_A BINDING SITE

Abstract

Previously we have shown that ONIOM type (QM/MM) calculations can be used to simulate isotope edited FTIR difference spectra for neutral ubiquinone in the Q_A binding site in *Rhodobacter sphaeroides* photosynthetic reaction centers. Here we considerably extend upon this previous work by calculating isotope edited FTIR difference spectra for reaction centers with a variety of unlabeled and ^{18}O labeled foreign quinones incorporated into the Q_A binding site. Isotope edited spectra were calculated for reaction centers with 2,3-dimethoxy-5,6-dimethyl-1,4-benzoquinone (MQ_0), 2,3,5,6-tetramethyl-1,4-benzoquinone (duroquinone, DQ), and 2,3-dimethyl-l,4-naphthoquinone (DMNQ) incorporated, and compared to corresponding experimental spectra. The calculated and experimental spectra agree well, further demonstrating the utility and applicability of our ONIOM approach for calculating the vibrational properties of pigments in protein binding sites.

The normal modes that contribute to the bands in the calculated spectra, their composition, frequency and intensity, and how these quantities are modified upon ^{18}O labeling, are presented. This computed information leads to a new and more detailed understanding/interpretation of the experimental FTIR difference spectra.

Hydrogen bonding to the carbonyl groups of the incorporated quinones is shown to be relatively weak. It is also shown that there is some asymmetry in hydrogen bonding, accounting for 10-13 cm^{-1} separation in the frequencies of the carbonyl vibrational modes of the

incorporated quinones. The extent of asymmetry H-bonding could only be established by considering the spectra for various types of quinones incorporated into the Q_A binding site.

The quinones listed above are "tail-less". Spectra were also calculated for reaction centers with corresponding "tail" containing quinones incorporated, and it is found that replacement of the quinone methyl group by a phytyl or prenyl chain does not alter ONIOM calculated spectra.

5.1 Introduction

Quinones play an important role in biological proton and electron transfer processes that occur in both respiration and photosynthesis [110]. In type II photosynthetic reaction centers two quinone molecules act as terminal electron acceptors [150, 151]. The two quinones are often termed Q_A and Q_B. In this manuscript we will refer to the quinone binding site as Q_A and Q_B, however. The quinones that occupy the Q_A and Q_B binding sites have very different functions. The Q_A quinone is an intermediary cofactor involved in transferring electrons from (bacterio)pheophytin to Q_B, while the Q_B quinone couples proton and electron transfer processes [111, 112, 151].

In this chapter we focus on the Q_A binding site. The quinone occupying the Q_A binding site is species dependent. In *Rhodobacter* (*Rb.*) *sphaeroides* purple bacterial reaction centers (PBRCs) a ubiquinone (UQ) molecule occupies the Q_A binding site. In PBRCs from *Blastochloris Viridis* [152] and *Chloroflexus aurantiacus* [153] a menaquinone occupies the Q_A binding site. In photosystem II reaction centers from oxygen evolving organisms, a plastoquinone (PQ) molecule occupies the Q_A binding site. In photosystem I the secondary electron acceptor, termed A_1, is a vitamin K_1 (VK) molecule (also called phylloquinone).

Menaquinone and VK are both naphthoquinone (NQ) moieties that differ only in the degree of saturation of the tail at C_6.

Figure 5.1 shows the structure, numbering and abbreviations we will use for the various quinones discussed in this manuscript. MQ_0 and DMNQ are UQ and VK analogues, respectively, in which the hydrocarbon tail has been replaced with a methyl group. DQ is a PQ analogue in which the hydrocarbon chain at C_6 is replaced with a methyl group.

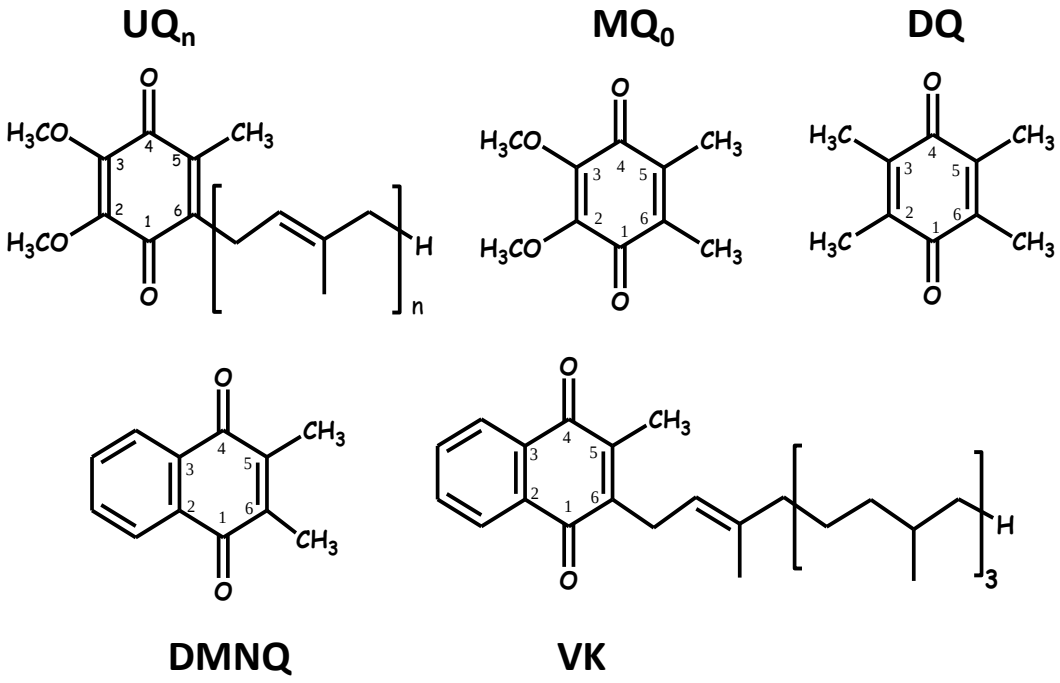

Figure 5.1 Structure and numbering of ubiquinone (2,3-dimethoxy, 5-methyl,6-prenyl benzoquinone) (UQ_n), 2,3-dimethoxy, 5,6-methyl benzoquinone (MQ_0), 2,3,5,6-methyl benzoquinone (duroquinone, DQ), 2,3-dimethyl, 1,4-naphthoquinone (DMNQ) and 2-methyl, 3-phytyl 1,4-naphthoquinone (VK). The numbering scheme employed here for the naphthoquinone structures is nonstandard, and was chosen to facilitate comparison between naphthoquinone and ubiquinone structures.

It has been suggested, at least for the UQ that occupies the Q_A site in PBRCs, that the role of the hydrocarbon chain at C_6 is to anchor and orient the quinone head-group in a specific way [154]. Data is available that may argue against this proposal, however [68, 134, 155].

Comparison of the properties of PBRCs with MQ_0 and UQ_n, or VK and DMNQ, incorporated into the Q_A binding site will allow one to assess how or if the hydrocarbon chain at

C_6 modifies the quinones functional properties. Similarly, comparison of the properties of PBRCs with MQ_0 and DQ incorporated into the Q_A binding site will allow one to assess how or if the methoxy groups at C_2 and C_3 modifies the quinones functional properties. Calculated spectra for *Rb. sphaeroides* PBRCs with VK in the Q_A binding site can be compared to experimental spectra. These calculated spectra may also serve as a useful model for *B. viridis* PBRCs that naturally have VK incorporated into the Q_A binding site.

Fourier transform infrared (FTIR) difference spectroscopy (DS) is a sensitive molecular-level probe of pigment-protein interactions, and it is widely used to study both the neutral and reduced states of quinones in PBRCs [115] and in photosystem II [156]. In this manuscript we focus on Q_A^-/Q_A FTIR DS. Many molecular species contribute to Q_A^-/Q_A FTIR DS, and in the past it has been difficult to identify which bands are associated specifically with UQ in the Q_A site. However, fully functional quinones can be incorporated into Q_A depleted PBRCs, and by collecting Q_A^-/Q_A FTIR DS using PBRCs with unlabeled and isotopically labeled quinones incorporated, so called isotope edited FTIR difference spectra can be constructed, and from these spectra it has proven possible to separate contributions of the quinones from those of the protein in Q_A^-/Q_A FTIR DS [115]. Previously, a variety of unlabeled and ^{18}O labeled quinones have been incorporated into the Q_A binding site in PBRC's, and ^{18}O isotope edited FTIR DS have been obtained [157]. The goal in this manuscript is the simulation of these experimental ^{18}O isotope edited FTIR DS associated with the neutral state of the quinone in the Q_A binding site. Calculated IR spectra associated with the quinone anion state are considerably more complicated [158] and are currently being undertaken.

Although experimental Q_A^-/Q_A FTIR DS have been obtained using PBRCs with various unlabeled and isotope labeled quinones incorporated, virtually no computational work aimed at

modeling the experimental FTIR DS have been undertaken. Calculations aimed at modeling the vibrational properties of quinones in the Q_A binding site must account for the protein environment. Quantum mechanical (QM) calculations of such a large molecular system (pigment plus protein environment) are unfeasible. To circumnavigate this problem methods have been developed that allow one to separate the molecular system into distinct layers that can be treated at different levels of theory. In one layer the chemical properties of the principle species of interest (the pigment) can be calculated using "high-level" QM methods. The surrounding protein environment is included in the calculation but it is treated using computationally less expensive molecular mechanics (MM) methods.

Recently we have undertaken QM: MM calculations for UQ in the Q_A binding site using the ONIOM method [118]. ONIOM is an acronym for: our Own N-layered Integrated molecular Orbital + Molecular mechanics package. In these calculations we showed that we could simulate experimental isotope edited FTIR difference spectra obtained using PBRCs with neutral UQ in the Q_A binding site. Here we extend upon these previous studies by attempting to simulate experimental isotope edited FTIR difference spectra obtained using PBRCs with symmetric tail-less and corresponding tail containing quinones incorporated into the Q_A binding site. We show that the calculated spectra agree well with the experimental spectra, further supporting the notion that the ONIOM method is a useful approach for understanding complex FTIR difference spectra associated with pigments in protein binding sites. We are also able to assess to what extent the quinone hydrocarbon chain may influence the calculated spectra.

5.2 Materials and Methods

5.2.1 Structural Model Used in Calculations

The molecular model used in ONIOM calculations was generated from the crystal structure of *Rb. sphaeroides* PBRCs at 2.2 Å resolution [25] (PDB file 1AIJ). From the PDB file all atoms within 10 Å of either carbonyl oxygen atom of UQ were selected. This subset of atoms formed the basis of the Q_A binding site structural model. Hydrogen atoms (not included in the PDB file) were added to the model using the software Gaussview4, resulting in a final structural model consisting of 1024 atoms. Following the addition of hydrogen atoms the structural model was optimized (energy minimized) using ONIOM methods with all atoms associated with the protein backbone, and the non-heme iron atom, being held fixed. All atoms of the amino acid side chains and the incorporated quinone are unconstrained. For calculations of UQ/VK the hydrocarbon tail was modeled as a single prenyl/phytyl unit, respectively. Inclusion of further prenyl/phytyl units did not alter the calculated spectra (not shown).

The structural models for the different incorporated quinones are initially set up by simply replacing the molecular substituents of the originally incorporated UQ species. So, the C=O groups of the different quinones incorporated will initially have the same orientation and position to that found for UQ in the Q_A binding site. DMNQ and VK structures were constructed starting from the UQ structure, by replacing the methoxy groups with the NQ aromatic ring, without alteration of the quinone ring (Figure 5.2F). This orientation of the NQ ring (of DMNQ and VK) was chosen as previous docking calculations have suggested it is the most favorable [159].

5.2.2 Calculations

All calculations were undertaken using Gaussian 03 [91] software. For calculation of UQ molecules in the gas phase, and for the QM part of ONIOM calculations, molecular geometry optimizations and harmonic vibrational frequency calculations were undertaken using hybrid DFT methods, employing the B3LYP functional and the 6-31+G(d) basis set. This choice of functional and basis set are appropriate for calculation of the vibrational properties of quinones [160, 161]. The MM part of the ONIOM calculation is undertaken using the AMBER force field [123]. Following ONIOM geometry optimization of the structural model, the optimized quinone molecule from the model is considered separately for vibrational frequency calculations.

5.2.3 Normal Mode Assessment

Assignment of calculated vibrational frequencies to molecular groups is based on a consideration of the calculated atomic displacements (in Cartesian coordinates) associated with the normal modes. These atomic displacements can be animated using software (GaussView4), and the molecular groups that most prominently contribute to the normal modes can be assessed visually (for example, see Figure 5.2 in reference [160]). In addition, potential energy distributions of the normal modes are calculated using the freeware GAR2PED [128]. For the various quinones in the Q_A binding site we calculate both vibrational mode frequencies and intensities. With both the frequency and intensity information "stick spectra" can be constructed. These stick spectra are representative of IR absorption spectra, as described previously [90, 140, 162]. The calculated stick spectra are convolved with a Gaussian function with half-width of 4 cm^{-1} to produce more realistic looking IR absorption spectra [90, 140, 162].

5.3 Results

5.3.1 UQ structure and numbering

Figure 5.1 shows the structure and numbering scheme used here for UQ_n, MQ_0, DQ, DMNQ and VK. Naphthoquinones generally have a different numbering scheme. We have applied the UQ numbering scheme to DMNQ and VK for the sake of easy comparison. Figure 5.2 shows a picture of (A) DMNQ, (B) VK, (C) MQ_0 and (D) UQ_1 in the Q_A binding site along with the two H-bonding amino acids. The structures shown are after geometry optimization using ONIOM methods. Possible hydrogen bonds (or ligand to the non-heme iron atom) are indicated by dotted lines.

To gain a better sense of the relative orientation of the different quinones in the Q_A binding site Figure 5.2 also shows the (E) DMNQ/DQ and (F) DMNQ/UQ structures from two ONIOM calculations overlapped. These overlapped structures are created by considering the (fixed) atoms of the protein backbone. Figure 5.2E/F indicates that the side chains of HisM219 and AlaM260 are unaltered when a different quinone is incorporated into the binding site.

Table 5.1 lists several bond lengths and bond angles derived from our ONIOM calculated optimized geometries of the various quinones in the Q_A binding site. For comparison, Table 5.1 also lists corresponding bond lengths and angles derived from our DFT calculated optimized geometries of the various quinones in the gas phase. Table 5.1 also list results obtained from previous QM/MM calculations [122], and data taken from the 1AIJ crystal structure [25].

Table 5.1 list the three distances associated with the peptide or imidazole H-bond to the carbonyl oxygen atoms of the quinone (N-H, NH - - O and N - - O distances). These distances completely determine the N-H - - O H-bond geometry. These angles are listed in Table 5.1.

Table 5.1 Comparison of bond lengths and angles derived from the ONIOM calculated (**O**) and gas phase calculated (**GP**) optimized geometry of neutral UQ_1, MQ_0, DQ, VK and DMNQ. Bond lengths and angles from the 1AIJ crystal structure [25] are also listed. Distances are in Å and angles are in degrees. The C_2 and C_3 methoxy group dihedral angles are defined as the C_3-C_2-O-CH_3 and C_2-C_3-O-CH_3 dihedral angles.

	x-ray	**UQ_1**		**MQ_0**		**DQ**		**VK_1**		**DMNQ**		**Ref [122]**
	[25]	**O**	**GP**	**O**	**GP**	**O**	**GP**	**O**	**GP**	**O**	**GP**	**UQ_1**
C_1=O	1.234	1.227	1.223	1.227	1.223	1.232	1.230	1.233	1.229	1.232	1.229	1.235
C_4=O	1.232	1.238	1.231	1.238	1.231	1.236	1.231	1.236	1.229	1.236	1.229	1.237
C_2=C_3	1.404	1.366	1.364	1.367	1.364	1.355	1.355	1.405	1.405	1.406	1.405	
C_5=C_6	1.419	1.354	1.354	1.354	1.354	1.357	1.355	1.363	1.361	1.362	1.360	
AlaM260 H Bond												
N--O	2.837	2.837		2.846		2.895		2.856		2.878		
N-H	1.014	1.014		1.014		1.013		1.013		1.013		1.014
N-H--O	1.912	1.894		1.886		1.907		1.883		1.883		1.94±0.11
∠ N-H-O	150.2	153.3		156.7		164.4		159.9		166.7		147±7
∠ C-O--N	131.5	127.0		125.9		127.4		125.7		124.1		
∠ C-O-H	133.4	128.7		128.3		132.6		128.0		128.1		
HisM219 H Bond												
N--O	2.788	2.868		2.865		2.829		2.832		2.831		
N-H	1.020	1.020		1.020		1.019		1.020		1.020		1.017
N-H--O	1.788	1.849		1.845		1.810		1.815		1.812		1.79±0.14
∠ N-H--O	166.2	175.8		177.7		178.8		174.3		178.2		170±6
∠ C-O--N	138.4	140.1		139.7		137.4		138.4		137.8		
∠ C-O--H	140.6	139.4		139.2		137.4		137.5		137.3		
C_4=O - Fe	6.832	6.744		6.715		6.627		6.692		6.637		
∠ Tail	113.0	114.9	111.7					114.7	111.6			
C_2-dihedral	-57.1	-25.3	-8.9	-26.5	-10.1							
C_3-dihedral	109.5	150.5	123.6	150.6	123.1							

For UQ_{10} in the Q_A site the 1AIJ crystal structure [25] indicates that the C_1=O bond is marginally longer than the C_4=O bond. (1.234 *versus* 1.232 Å). In contrast, from ONIOM calculations of all the quinones listed in Table 5.1 the C_1=O bond is shorter than the C_4=O bond.

In gas phase calculations the C_1=O and C_4=O bond lengths are shorter than that found in ONIOM calculations (except the C_1=O of DQ). This lengthening of the C=O bonds of the quinones in the Q_A binding site is related to hydrogen bonding and other electrostatic interactions of the pigment with the protein environment.

For UQ_1 and MQ_0 the C_1=O bond is shorter than the C_4=O bond in both ONIOM and gas phase calculations. In gas phase calculations this difference in C_1=O and C_4=O bond lengths of UQ_1 and MQ_0 must relate to the differing orientations of the C_2 and C_3 methoxy groups. The

ONIOM calculated C_2 and C_3 methoxy group dihedral angles for UQ_1 are -25.3 and 150.5^o (Table 5.1). Similar angles are calculated for MQ_0. The calculated dihedral angles for UQ_1 in the gas phase, and the observed angles for UQ_{10} in the Q_A binding site (from the crystal structure) are within 32 degrees of that calculated for UQ_1 using ONIOM methods.

For UQ_{10} in the Q_A site the crystal structure indicates that the C_2=C_3 bond is shorter than the C_5=C_6 bond. (1.404 *versus* 1.419 Å). In contrast, for all quinones except DQ, in both ONIOM and gas phase calculations the C_2=C_3 bond is longer than the C_5=C_6 bond. For VK and DMNQ the calculated C_2=C_3 and C_5=C_6 bond lengths are considerably different.

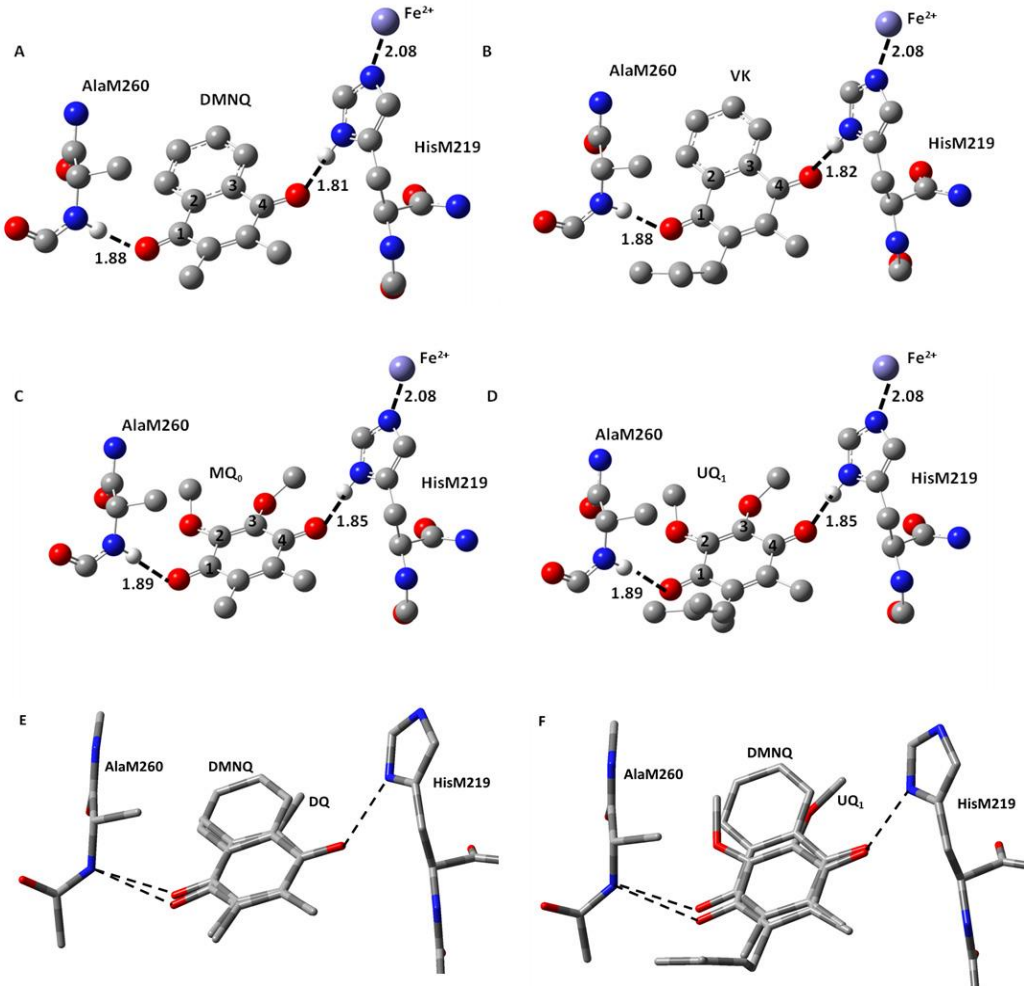

Figure 5.2 Ball and stick representation of the calculated structure of (A) DMNQ, (B) VK, (C) MQ_0 and (D) UQ_1 in the Q_A binding site in PBRCs from *Rb. sphaeroides*. Structure shown is after geometry

optimization using ONIOM methods. Possible H-bonds are shown (*dotted*). Hydrogen atoms, except the ones involved in H-bonding, have been omitted. Distances quoted are in Å. (E, F) Overlap of structures obtained from ONIOM calculations for (E) DMNQ and DQ and (F) DMNQ and UQ_1. Overlap is based on using the (fixed) backbone atoms of HisM219 and AlaM260. The amino acid side chains are virtually unaltered in the structures shown.

For UQ_1 and VK the hydrocarbon chain attached at C_6 makes a distinct "kink" after the first carbon atom (Figure 5.2B, D). The C-C-C bond angle is 112-115^o for both quinones in both the ONIOM and gas phase calculations. The calculated angles are virtually the same as that found in the crystal structure. Given these similarities (between the ONIOM and gas phase calculations for both UQ_1 and VK, as well as between calculation and experiment) the suggestion is that the protein environment does not constrain the orientation of the quinone ring relative to the C_6 hydrocarbon chain.

Figure 5.3A shows ONIOM calculated ^{18}O isotope edited difference spectra for neutral VK and DMNQ. Figure 5.3D shows corresponding DFT calculated spectra for VK and DMNQ in the gas phase. Experimental spectra are also shown (Figure 5.3B and C) for comparison. Positive/negative bands in the isotope edited spectra are due to the unlabeled/^{18}O labeled quinone species, respectively. The ONIOM calculated spectra clearly better describe the experimental spectra. Calculations including the protein environment appear to be necessary in order to adequately simulate the experimental spectra.

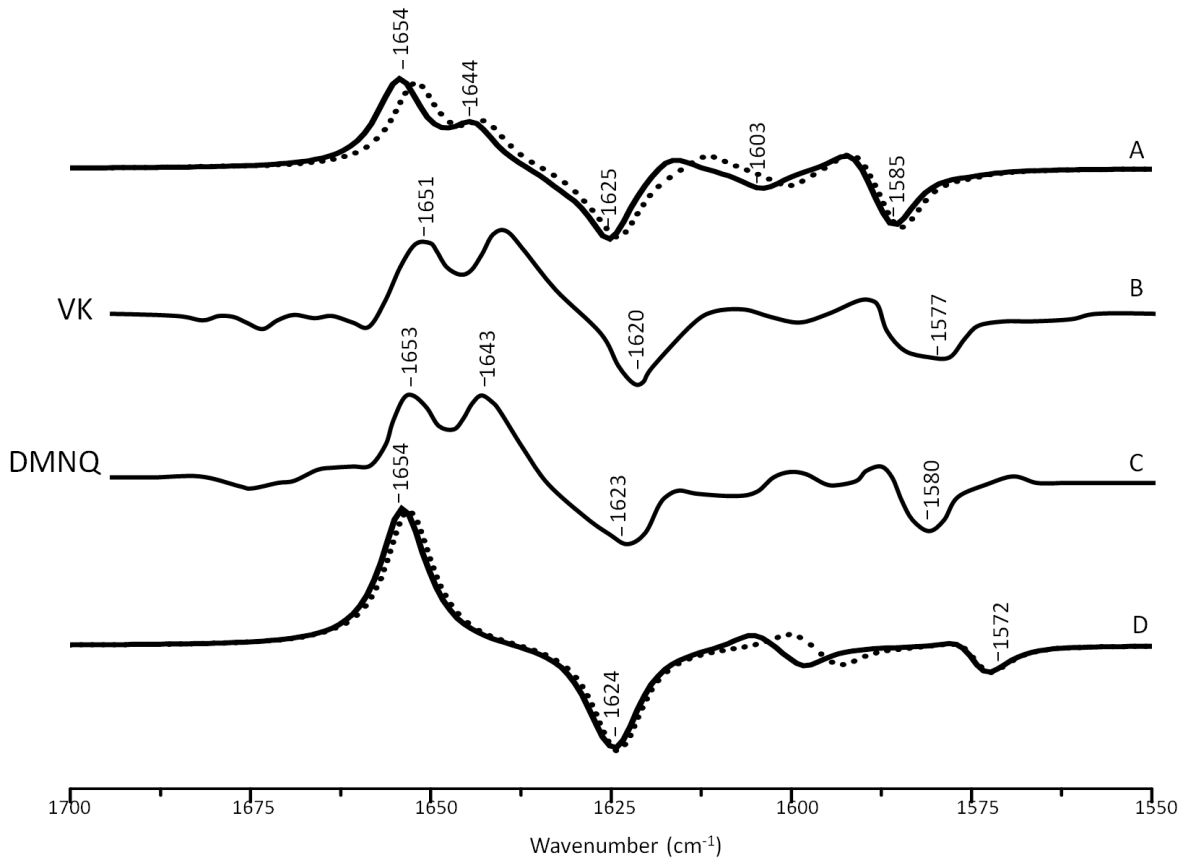

Figure 5.3 (A) ONIOM calculated ^{18}O isotope edited DDS for neutral VK (*dotted*) and DMNQ (*solid*) in the Q_A binding site. Experimental spectra for VK (B) and DMNQ (C) are also shown, and were taken from reference [157], with permission. (D) DFT calculated ^{18}O isotope edited DDS for neutral VK (*dotted*) and DMNQ (*solid*) are also shown. ONIOM/gas phase calculated spectra were scaled by 0.9718/0.9608, respectively.

In the DFT calculated ^{18}O isotope edited spectrum for DMNQ/VK in the gas phase (Figure 5.3D) the antisymmetric vibration of both C=O groups gives rise to the band at ~1654 cm^{-1} (Figure 5.3D), which downshifts 30 cm^{-1} upon ^{18}O labeling [160]. The calculated isotope-edited gas phase spectrum is in excellent agreement with the experimental spectrum for DMNQ in solution [157].

Figure 5.3 shows that except for a small frequency shift in some of the modes, the calculated spectra for DMNQ and VK are virtually the same. Replacement of the methyl group at C_6 with an isoprene unit therefore has no influence on the calculated spectra.

The normal modes (frequencies and intensities) that give rise to the various bands in the ONIOM calculated ^{18}O isotope edited spectra of DMNQ and VK are listed in Table 5.2. The potential energy distributions (PEDs), which quantify to what extent various internal coordinates contribute to the normal modes, are also listed in Table 5.2. Results for DMNQ and VK are very similar. Below we will discuss calculated data obtained for DMNQ with the recognition that very similar results and conclusions also apply to VK.

Table 5.2 Normal mode frequencies (in cm^{-1}), intensities (in km/mol) and PEDs (in %) calculated using ONIOM methods for unlabeled and ^{18}O labeled neutral DMNQ, VK, DQ, MQ_0 and UQ_1. Frequency shifts upon ^{18}O labeling are also listed. Negative signs in the PEDs refer to the relative phase of vibration of the internal coordinates. Only internal coordinates that contribute at least 5 % are shown. Mode frequencies were scaled by 0.9718.

	Unlabeled			**^{18}O Labeled**			
	ν	**I**	**Potential Energy Distribution**	**ν**	**I**	**Δν**	**Potential Energy Distribution**
DMNQ	1654	235	C_1=O (71)	1631	32	23	C_1=O (28), C_5=C_6 (22), C_2=C_3 (10)
VK	1652	224	C_1=O (69)	1628	29	24	C_1=O (32), C_5=C_6 (16), C_2=C_3 (6)
DQ	1646	254	C_1=O (83)	1613	264	33	C_1=O (80)
MQ_0	1666	209	C_1=O (81)	1631	211	35	C_1=O (83)
UQ_1	1663	185	C_1=O (80)	1629	187	34	C_1=O (82)
DMNQ	1644	108	C_4=O (60)	1625	199	19	C_4=O (26), -C_1=O (21), C_5=C_6 (8), -C_3=C_7 (7)
VK	1642	107	C_4=O (60)	1624	188	18	
DQ	1632	181	C_4=O (83)	1599	144	33	C_4=O (29), -C_1=O (15), C_5=C_6 (8), -C_3=C_7 (7)
MQ_0	1627	270	C_4=O (70), -C_2=C_3 (8)	1587	265	40	
UQ_1	1626	305	C_4=O (68), -C_2=C_3 (9)	1586	249	40	C_1=O (81) C_4=O (63), C_2=C_3 (9), -C_5=C_6 (5) C_4=O (65), C_2=C_3 (7), -C_5=C_6 (6)
DMNQ	1617	59	C_5=C_6 (61), -C_4=O (8)	1604	54	13	C_5=C_6 (37), - C_4=O (25), -C_1=O (14)
VK	1611	54	C_5=C_6 (60), -C_4=O (8)	1600	52	11	C_5=C_6 (42), -C_4=O (20), -C_1=O (14)
DQ	1660	1	C_2=C_3 (32), C_5=C_6 (28)	1660	0	0	C_5=C_6 (29), C_2=C_3 (33)
MQ_0	1657	20		1657	8	0	C_5=C_6 (49), C_2=C_3 (13)
UQ_1	1653	26	C_5=C_6 (52), C_2=C_3 (15) C_5=C_6 (45), C_2=C_3 (19)	1654	18	-1	C_5=C_6 (44), C_2=C_3 (17)
DMNQ	1591	93	C=C_{arom} (55)	1586	181	5	C=C_{arom} (43), -C_4=O (13), C_1=O (10)
VK	1591	96	C=C_{arom} (54), -C_4=O (5)	1585	186	6	C=C_{arom} (40), -C_4=O (14), C_1=O (11)
DQ	1620	55		1620	56	0	C_5=C_6 (37), -C_2=C_3 (34)
MQ_0	1601	293	C_5=C_6 (38), -C_2=C_3 (33)	1609	273	-7	C_2=C_3 (40), -C_4=O (15), -C_5=C_6 (12), -C_2=O (11)
UQ_1	1601	275	C_2=C_3 (39), -C_5=C_6 (15), C_4=O (12), -C_2=O (7) C_2=C_3 (35), -C_5=C_6 (18), C_4=O (14), -C_2=O (6)	1609	308	-8	C_2=C_3 (37), -C_4=O (13), -C_5=C_6 (15), -C_2-O (10)

In the ONIOM calculated ^{18}O isotope edited spectra for DMNQ the two bands at 1654 and 1644 cm^{-1} are due to C_1=O and C_4=O stretching vibrations, respectively (Table 5.2). These bands almost certainly correspond to the at 1653 and 1643 cm^{-1} bands in the experimental spectrum (Figure 5.3C). So our calculations *predict* that the 1653 and 1643 cm^{-1} bands in the experimental spectrum are due to C_1=O and C_4=O stretching vibrations, respectively. This is in fact the first direct evidence that the 1653 and 1643 cm^{-1} bands in the experimental spectrum are due to C_1=O and C_4=O stretching vibrations. A direct assignment has never been made because specific $^{13}C_1$ and $^{13}C_4$ isotopic labeled VK or DMNQ has never been incorporated into the Q_A binding site in PBRCs.

In contrast to the observation of two separate C=O modes in ONIOM calculations, in gas phase calculations the two C=O modes of DMNQ are anti-symmetrically coupled [90], giving rise to a single intense band at 1654 cm^{-1} (Figure 5.3D).

In ONIOM calculations it is found that upon ^{18}O labeling the C_1=O and C_4=O modes of DMNQ downshift 23 and 19 cm^{-1}, to 1631 and 1625 cm^{-1}, respectively (Table 5.2). Upon ^{18}O labeling the 1625 cm^{-1} mode is more than six times more intense than the 1631 cm^{-1} mode. The 1625 cm^{-1} mode in ^{18}O labeled DMNQ is due mainly to the antisymmetric coupled vibration of both C=O groups. That is, two separate C=O modes of unlabeled DMNQ couple upon ^{18}O labeling. This behavior is not predicted based upon consideration of the experimental spectra, where it is "assumed" that the two C=O modes remain separate upon ^{18}O labeling [109, 163].

A C=C mode of the quinone ring of DMNQ is found at 1617 cm^{-1}. This quinonic C=C mode downshifts 13 cm^{-1}, to 1604 cm^{-1}, upon ^{18}O labeling, with little change in intensity. The 1604 cm^{-1} mode composition in ^{18}O labeled DMNQ displays considerable mixing of the C=O

and C=C modes (the C=O modes account for 39% of the PED). This behavior might be expected given that the C=O and C=C modes are closer in frequency upon ^{18}O labeling.

A C=C mode of the aromatic ring of DMNQ occurs at 1591 cm^{-1}. This aromatic C=C mode downshifts 5 cm^{-1} to 1586 cm^{-1} upon ^{18}O labeling. The 1586 cm^{-1} mode in ^{18}O labeled DMNQ displays some mixing with C=O modes (23%), and the intensity of the aromatic C=C mode nearly doubles upon ^{18}O labeling. The calculated C=C normal modes and their interpretation in terms of internal coordinates, as well as the calculated ^{18}O induced frequency shifts are similar to that suggested on the basis of the experimental spectra [157].

Figure 5.4A shows ONIOM calculated ^{18}O isotope edited IR difference spectra for neutral DQ in the Q_A binding site. Figure 5.4C shows the corresponding DFT calculated spectrum for DQ in the gas phase. The experimental spectrum is shown in Figure 5.4B. Again, the ONIOM calculated spectrum agrees well with the experimental spectrum while the calculated gas phase spectrum does not. The ONIOM calculated normal modes (frequencies and intensities) that give rise to the bands in the ^{18}O isotope edited spectrum for DQ, as well as the PEDs, are listed in Table 5.2.

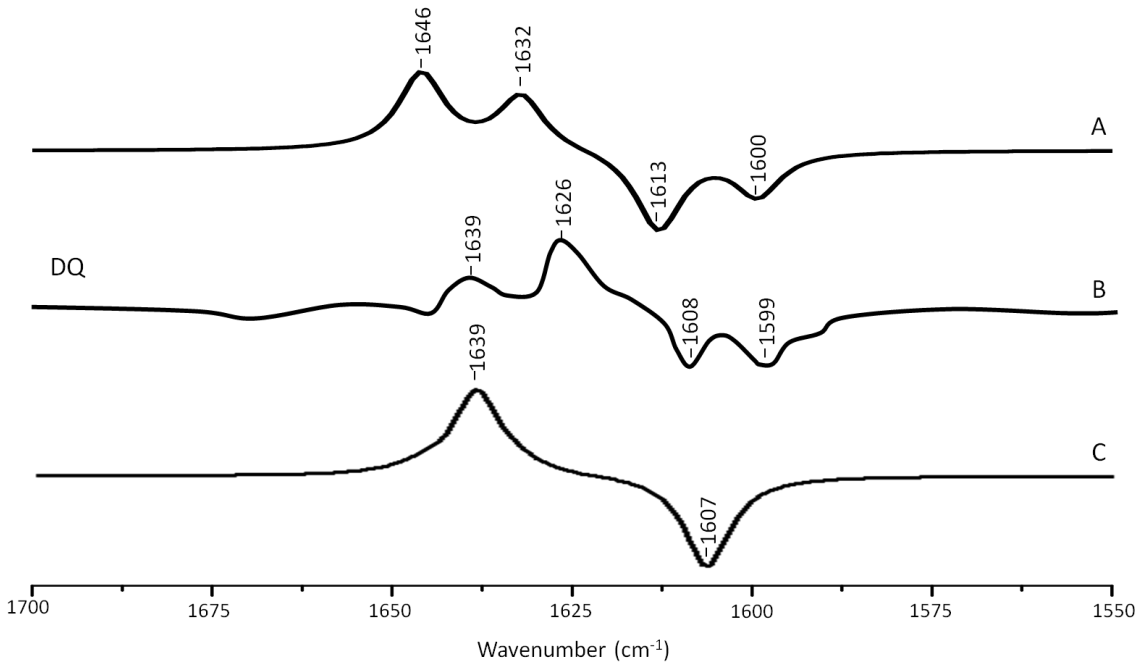

Figure 5.4 (A) ONIOM calculated ^{18}O isotope edited DDS for neutral DQ in the Q_A binding site. Experimental spectra are shown in (B), and were taken from reference [157] with permission. (C) DFT calculated ^{18}O isotope edited DDS for neutral DQ. ONIOM and gas phase calculated spectra were scaled by 0.9718 and 0.9608, respectively.

In the ONIOM calculated ^{18}O isotope edited spectrum for DQ the two bands at 1646 and 1632 cm^{-1} are due to C_1=O and C_4=O stretching vibrations, respectively (Table 5.2). Upon ^{18}O labeling the C_4=O and C_1=O modes both downshift 33 cm^{-1} with little change in mode intensities (Table 5.2). This 33 cm^{-1} downshift is large compared to that calculated for DMNQ (19-23 cm^{-1}). For DQ, the ONIOM calculated mode composition is virtually unchanged upon ^{18}O labeling. This is also markedly different to that calculated for DMNQ. The normal modes that give rise to the isotope edited spectra of DQ and DMNQ in the gas phase are very similar, so replacing the methyl groups of DQ with the aromatic ring of DMNQ in the Q_A binding site leads to an alteration in the electronic structure of the quinone ring. This modification is not obvious given the similar orientation of DQ and DMNQ in the Q_A binding site (Figure 5.2E).

In the DFT calculated ^{18}O isotope edited spectrum for DQ in the gas phase, the two C=O modes are strongly coupled, and give rise to the band at 1639 cm^{-1} in Figure 5.4C. The calculated gas phase spectrum is in line with the experimental FTIR spectrum for DQ in solution [157].

From ONIOM calculations for DQ, C=C modes do not couple with the C=O modes. The C_2=C_3 and C_5=C_6 groups couple to produce in phase and out of phase vibrational modes. The in phase mode has negligible IR intensity. The out of phase C=C mode is calculated to be at 1620 cm^{-1}. This C=C mode is virtually unaltered in frequency, intensity and mode composition upon ^{18}O labeling (Table 5.2).

Figure 5.5A shows ONIOM calculated ^{18}O isotope edited IR spectra for neutral MQ_0 (*solid*) and UQ_1 (dotted) in the Q_A binding site. Figure 5.5D shows DFT calculated spectra for MQ_0 and UQ_1 in the gas phase. The experimental spectra for UQ_1 and MQ_0 are shown in Figure 5.5B and C, respectively. The normal modes (frequencies and intensities) that give rise to the various bands in the ONIOM calculated spectra, as well as the PEDs, are listed in Table 5.2. The data for UQ_1 has been presented previously [117], and we show here that very similar spectra are calculated for both MQ_0 and UQ_1. Replacement of an isoprene unit at C_6 with a methyl group does not greatly alter the calculated spectra.

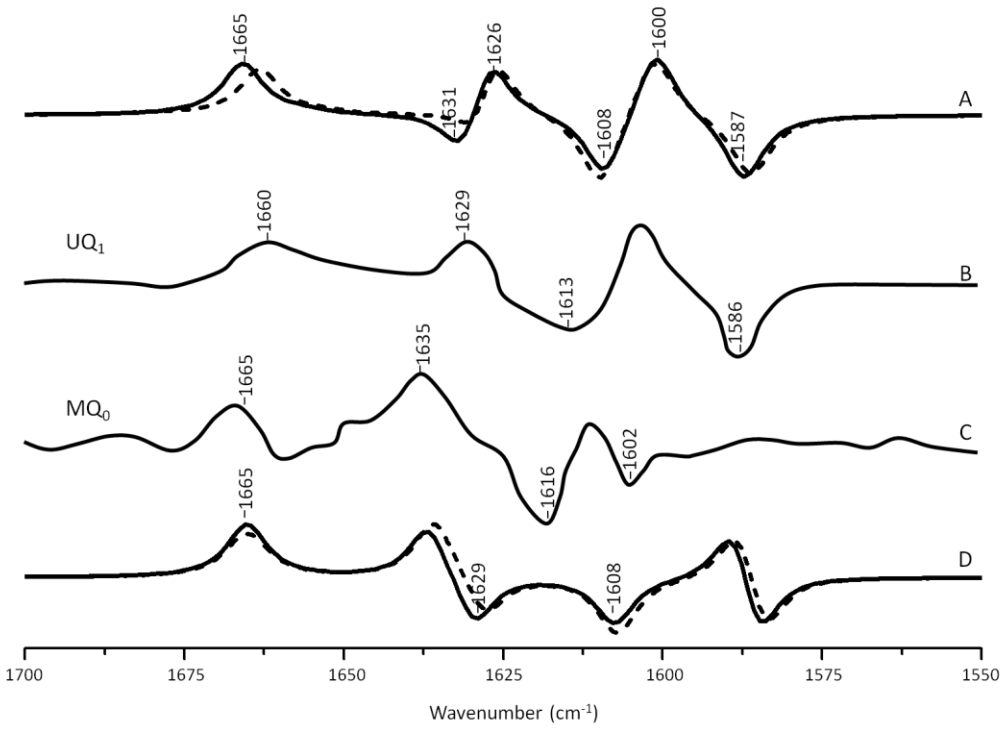

Figure 5.5 (A) ONIOM calculated ^{18}O isotope edited DDS for neutral MQ_0 (*solid*) and UQ_1 (*dotted*) in the Q_A binding site. Experimental spectrum for (B) MQ_0 and (C) UQ_1 are also shown, and were taken from reference [157] with permission. (D) DFT calculated ^{18}O isotope edited DDS for neutral MQ_0 (*solid*) and UQ_1 (*dotted*). ONIOM and gas phase calculated spectra were scaled by 0.9718 and 0.9608, respectively.

In the ONIOM calculated ^{18}O isotope edited spectra for neutral MQ_0 the two bands at 1666 and 1627 cm^{-1} (Figure 5.5C) are due to C_1=O and C_4=O stretching vibrations, respectively (Table 5.2). Upon ^{18}O labeling the C_1=O and C_4=O modes downshift 35 and 40 cm^{-1}, respectively (Table 5.2). The mode intensities and composition are little altered by ^{18}O labeling. The C=C mode of MQ_0/UQ_1 at 1601 cm^{-1} up-shifts 8/7 cm^{-1} upon ^{18}O labeling (Table 5.2). An explanation for this ^{18}O induced frequency upshift has been presented [117].

In the DFT calculated ^{18}O isotope edited spectra for UQ_1/MQ_0 in the gas phase, the two C=O modes are well separated, and give rise to bands at ~1665 and ~1635 cm^{-1} (Figure 5.5D), which downshift 36 and 27 cm^{-1}, respectively, upon ^{18}O labeling, as described previously [140].

5.4 Discussion

Previously we have shown that ONIOM methods can be used to calculate isotope edited difference spectra for UQ_1 in the Q_A binding site, and that these calculated spectra model very well the corresponding experimental spectra [117]. Here we considerably extend these studies, and show that ONIOM calculated isotope edited spectra for different quinones in the Q_A binding site model very well the corresponding experimental spectra. We further show that the calculated spectra for quinones in the gas phase are totally inappropriate for modeling the vibrational properties of quinones in the Q_A binding site. This is also very likely to be the case for modeling the properties of any protein bound pigment.

Without normal mode vibrational frequency calculations interpretation of experimental spectra is limited, and here we clearly show that our computational methods lead to a greatly increased understanding of the normal modes that contribute to the bands in the experimental spectra.

In our ONIOM calculations for neutral UQ_1 in the Q_A binding site we considered all amino acids included in the model only at the molecular mechanics level of computation. Previously, ONIOM calculations have been undertaken in order to model EPR data associated with the UQ anion in the Q_A binding site [50]. In these calculations key amino acids, such as HisM219 and AlaM260, were considered at the higher quantum mechanical level of calculation. Taken together these results may indicate differences in the nature of H-bonding for the neutral and anion UQ species. Changes in H-bonding upon radical formation may be a mechanism for (de)stabilizing cofactors to fine-tune electron transfer processes in biological systems. Clearly it will be useful to undertake calculations similar to that presented here (modeling isotope edited FTIR difference spectra) for the UQ anion in the Q_A binding site, and such calculations are

underway in our lab. Based on the above one could argue that the methods used here, with only the quinone treated at the QM level, will be inadequate to simulate the experimental spectra associated with quinone anions in the Q_A binding site. Or, for simulating the vibrational properties of quinone anions in the Q_A binding site it will be necessary to treat key amino acids at a quantum mechanical level. Again, calculations are underway in our lab to test this proposal.

For the neutral state of quinones occupying the Q_A binding site, calculations with the H-bonding amino acids treated at the MM level lead to calculated spectra that are in excellent agreement with experimental spectra (Figures 5.3, 5.4 and 5.5). Clearly, treating H-bonding amino acids quantum mechanically will not lead to improved modeling of the experimental spectra. We have in fact undertaken calculations in which neutral UQ and the H-bonding amino acids are treated using QM, and we have found that the calculated spectra are very similar to that obtained when only neutral UQ is treated using QM (and the surrounding amino acids are treated using MM) [63]. Thus it is very clear that, at least for the case of neutral quinones occupying the Q_A binding site, and as far as modeling isotope edited FTIR spectra is concerned, QM/MM calculations with only the quinone treated at the QM level need to be considered.

An experimental ^{18}O isotope edited FTIR difference spectrum for UQ in the Q_A binding site is shown in Figure 5.5B. Three positive bands at 1660, 1629 and 1601 cm^{-1} are observed. By considering FTIR difference spectra obtained using PBRCs with unlabeled and specifically $^{13}C_1$ and $^{13}C_4$ labeled UQ occupying the Q_A binding site, it was concluded that the 1660 and 1601 cm^{-1} bands are due to the C_1=O and C_4=O vibrations of unlabeled neutral UQ, respectively. It was also concluded that the 1628 cm^{-1} band is due to a UQ C=C vibration [47]. Since the C_4=O mode was so massively downshifted (from ~1660 cm^{-1} for UQ in solvent to 1601 cm^{-1} for UQ in the Q_A binding site) it was suggested that this group must be engaged in very strong

hydrogen bonding, presumably with HisM219 (Figure 5.2) [47]. This conclusion is difficult to rationalize based on the crystal structural data and other experimental data (see [134] for a review). Such a conclusion is also not supported by the data presented here. Specifically, the C_1=O and C_4=O modes of DMNQ and VK are found at 1653 and 1643 cm^{-1} (Table 5.2), respectively, compared to ~1662 cm^{-1} for the coupled C=O vibration in solution [90]. Thus the C_1=O/C_4=O mode of DMNQ or VK in the Q_A site is downshifted 9/19 cm^{-1}, respectively, compared to that found in solution. Such shifts suggest that both C=O modes of DMNQ or VK are H-bonded in the Q_A site, albeit quite weakly.

From the experimental spectrum of VK (or DMNQ) in Figure 5.3B two positive bands are observed at 1651 and 1640 cm^{-1} and one negative band at 1620 cm^{-1}. The two C=O modes of unlabeled VK give rise to the positive bands at 1651 and 1640 cm^{-1}, but only a single band is observed at 1620 cm^{-1} upon ^{18}O labeling. Two interpretations for these observations have been proposed [109]. One suggestion is that upon ^{18}O labeling the 1640 cm^{-1} band downshifts to ~1620 cm^{-1}, while the 1651 cm^{-1} band downshifts to near 1640 cm^{-1} and decreases in intensity. The negative band near 1640 cm^{-1} due to a C=^{18}O group of VK is then masked by the positive band (also at 1640 cm^{-1}) due to the unlabeled C=O group. A second hypothesis is that the two C=O modes of unlabeled VK (at 1651 and 1640 cm^{-1}) both downshift to ~1620 cm^{-1} upon ^{18}O labeling. The different ^{18}O induced shifts of the two C=O modes results from differential coupling to C=C modes.

The calculated data presented here allow us to address which of these interpretations could be appropriate, or if either is appropriate. The ONIOM calculations show that the C_1=O and C_4=O modes of unlabeled VK occur at 1652 and 1642 cm^{-1}, and that neither of these modes are coupled to C=C modes (Table 5.2). Upon ^{18}O labeling the C_1=O/C_4=O mode downshifts

24/18 cm^{-1}, respectively. The modes of ^{18}O labeled VK also display considerable coupling with C=C modes. Upon ^{18}O labeling the C_1=O/C_4=O group couples with C=C_{ring} in-phase/out-of-phase vibrations, respectively. Coupling of the C_4=O group to the out of phase C=C vibration leads to a large intensity enhancement, while coupling of the C_1=O group to the in-phase C=C vibration leads to a large intensity decrease (Table 5.2). So, the calculations indicate that two separate uncoupled C=O modes in unlabeled VK give rise to predominantly a single mixed mode (that carries most of the intensity) in ^{18}O labeled VK. These calculated results indicate that neither of the two previously proposed interpretations of the experimental spectra is correct. Clearly, the calculations presented here allow a more detailed insight into the nature of the bands in the experimental isotope edited FTIR difference spectra.

Experimentally, the vibrational modes of DMNQ are at a slightly higher frequency (~3 cm^{-1}) than corresponding modes of VK. Presumably replacing the C_6 methyl group with a phytyl unit causes this difference. Interestingly, this small frequency difference in the modes of DMNQ and VK is also found in our ONIOM calculated spectra (compare spectra in Figure 5.5C and B). This result is not entirely specific to the ONIOM method, however, as a small shift is also found in the gas phase calculations (Figure 5.3D).

The C_1=O and C_4=O modes of DMNQ and VK are calculated to be separated by 10 cm^{-1}. This separation cannot be due to differences in the molecular group attached at C_6. It must be due to differences in how the two C=O groups interact with the protein. Similarly, the two C=O modes of DQ are calculated to be separated by 13 cm^{-1}, and this separation is also likely due to differences in how the two C=O groups of DQ interact with the protein.

For UQ_1 (and MQ_0) the separation of the C=O modes is ~32 cm^{-1} (1660-1628). Some of the differences in frequency of the C=O modes of UQ are due to the different orientation of the

methoxy groups. If we assume that protein interactions with the C=O groups gives rise to a 13 cm^{-1} separation in the frequencies of the two C=O modes then this would indicate that the difference in the orientation of the methoxy groups of UQ (or MQ_0) gives rise to a frequency difference of 19 cm^{-1} for the two C=O groups. This result is in quite good agreement with results from experimental spectra of UQ in solution, which show that the two C=O modes are separated by ~ 16 cm^{-1} [46, 47].

Normal mode vibrational frequencies are governed by molecular bonding force constants. These force constants relate to the electronic structure of the molecule. Since the calculated and experimental spectra for DMNQ and VK are virtually the same it is concluded that the replacing the phytyl unit at C_6 of VK with a methyl group does not appreciably perturb the electronic structure of the naphthoquinone ring. In addition, the tail does not perturb the protein in a way that significantly modifies any pigment protein interactions

In VK and UQ_1, the "kink" in the hydrocarbon chain after the first carbon atom is 3.1-3.2 degrees higher in ONIOM calculations compared to gas phase calculations. It seems therefore that the hydrocarbon chain is somewhat constrained relative to the quinone ring when incorporated into the Q_A binding site. It is not clear if this is a significant constraint, however. The C_1=O and C_4=O bonds of MQ_0 and UQ_1 (and of DMNQ and VK) are virtually unaltered in ONIOM calculations (Table 5.1). The hydrogen bond lengths for the C=O groups are also little altered (Table 5.1). The distance of the C_4=O oxygen to the non-heme iron atom is 0.029/0.055 Å longer for UQ_1/VK compared to MQ_0/DMNQ, respectively, suggesting a very small change in orientation of the UQ_1/VK head-group (since the iron atom is fixed) compared to MQ_0/DMNQ in the Q_A binding site. The hydrocarbon chain may therefore lead to a very slight change in the

orientation of the quinone ring in the Q_A binding site. Figure 5.2F shows that there is only a very small difference in the orientation of DMNQ relative to UQ_1.

The experimental ^{18}O isotope edited spectra for MQ_0 and UQ_1 are quite different (compare Figure 5.5B and C). This difference cannot be modeled computationally (Figure 5.5A). The experimental isotope edited spectrum for MQ_0 is considerably noisier than the spectrum for UQ [157]. As far as we are aware the Q_A^-/Q_A FTIR difference spectrum for RCs with MQ_0 in the binding site have never been reproduced, so the accuracy of the spectrum may be somewhat questionable. On the other hand MQ_0 may be able to incorporate into the Q_A binding site with the methoxy groups oriented in several different ways. As described previously, each of these methoxy group conformers will have slightly different spectra [140]. This heterogeneity in orientation of MQ_0 in the Q_A binding site may be a factor that contributes to differences in the experimental spectra for MQ_0 and UQ, as demonstrated in Figure 5.5B and C. In spite of this, there are some overall similarities in the MQ_0 and UQ_1 experimental spectra in Figure 5.5B and C. For the MQ_0 spectrum positive bands are found at 1665, 1631 and 1608 cm^{-1}. For UQ_1 the bands are at 1660, 1628 and 1601 cm^{-1}. For the MQ_0 spectrum negative bands are found at 1616 and 1602 cm^{-1}. For UQ the bands are at 1613 and 1586 cm^{-1}.

The ONIOM calculated and experimental isotope edited spectra for VK are very similar, although the intensity ratios of the different bands do not appear to match well. For example, the intensity ratio of 1652 and 1644 cm^{-1} bands in the calculated spectrum (Figure 5.3A, dotted) is ~2.1, compared to a ratio of ~0.95 in the experimental spectrum. To investigate this further we have also calculated the ^{13}C isotope edited spectrum for VK in the Q_A binding site (Figure 5.6A) (global ^{13}C labeling of VK), and compared it to the corresponding experimental spectrum (Figure 6B). For completeness the calculated ^{13}C isotope edited spectrum for VK in the gas phase is

shown in Figure 5.6C. Again, it is evident that the calculated gas phase spectrum in no way resembles the experimental spectrum (compare Figure 5.6B and 5.6C). The normal modes (frequencies, intensities and PEDs) that give rise to the various bands in the ONIOM calculated ^{13}C isotope edited spectra of VK in Figure 5.6A are listed in Table 5.3.

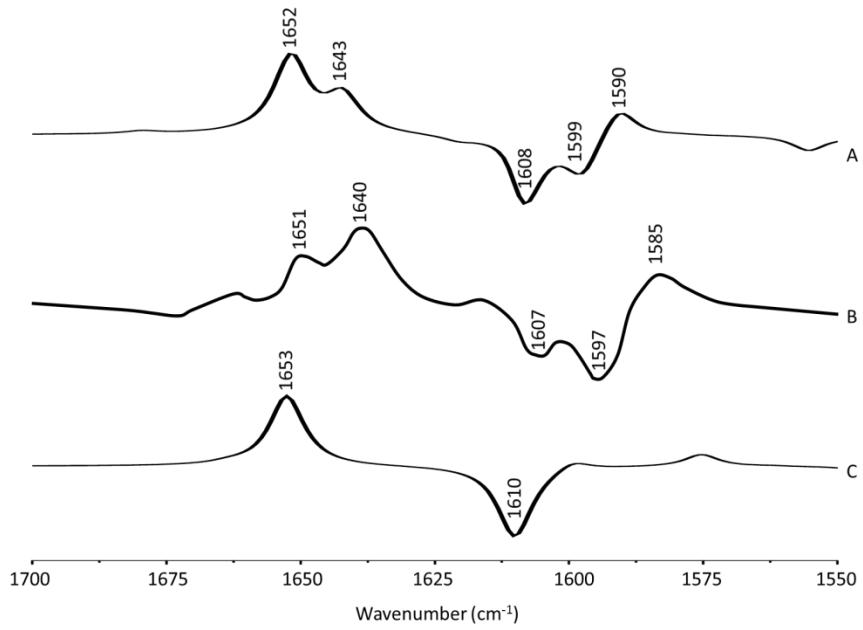

Figure 5.6 (A) ONIOM calculated ^{13}C isotope edited DDS for neutral VK in the Q_A binding site. Experimental spectrum is also shown (B), taken from [163] (with permission). (C) DFT calculated ^{13}C isotope edited DDS for neutral VK in the gas phase. ONIOM and gas phase calculated spectra were scaled by 0.9718 and 0.9608, respectively.

Notice that the ONIOM calculation predicts that the two C=O modes remain completely separate (do not mix) upon ^{13}C labeling (Table 5.3), which is unlike the behavior observed for the C=O modes upon ^{18}O labeling (see above). Also notice that in the experimental isotope edited spectrum (Figure 5.6B) the 1640 cm^{-1} band is now considerably more intense than the 1651 cm^{-1} band, whereas in the calculated spectrum the higher frequency band is considerably more intense. The origin of these mode intensity differences are not entirely clear and are currently being investigated by considering calculations associated with VK in the presence of various types of H-bonding molecules.

Table 5.3 Normal mode frequencies (in cm^{-1}), intensities (in km/mol) and PEDs (in %) calculated using ONIOM methods for unlabeled and ^{13}C labeled neutral VK. Frequency shifts upon ^{13}C labeling are also listed. Negative signs in the PEDs refer to the relative phase of vibration of the internal coordinates. Only internal coordinates that contribute at least 5 % are shown. Mode frequencies were scaled by 0.9718.

	Unlabeled			**^{13}C Labeled**			
	ν	**I**	**Potential Energy Distribution**	**ν**	**I**	**Δν**	**Potential Energy Distribution**
VK	1652	224	C_1=O (69)	1609	227	43	C_1=O (73)
	1642	107	C_4=O (60)	1598	116	44	C_4=O (70)
	1611	54	C_5=C_6 (60), -C_4=O (8)	1555	43	56	C_5=C_6 (57)
	1591	96	C=C_{arom} (54), -C_4=O (5)	1537	67	54	C=C_{arom} (55)

5.5 Conclusions

We have shown that ONIOM type QM/MM calculations can be used to model experimental isotope edited FTIR difference spectra obtained using purple bacterial reaction centers that have had several different quinones incorporated into the Q_A binding site. The fact that the many different spectra can all be modeled is a clear indicator of the appropriateness of the approach.

The calculated spectra appear not to depend on whether the quinone incorporated has a prenyl/phytyl unit or a methyl group attached at C_6. The electronic structure of the quinone ring is therefore not sensitive to the presence or absence of a hydrocarbon side chain at C_6. This suggests that the hydrocarbon side chain does not significantly constrain the quinone ring in the Q_A binding site.

Comparison of the calculated and experimental spectra, in combination with a consideration of the calculated potential energy distributions of the normal modes, allows a direct assessment of the appropriateness of previous suggestions as to the origin of the bands in the experimental spectra.

6 CONCLUSIONS AND FURTURE WORK

6.1 Dissertation conclusions

This dissertation presents studies of the vibrational properties of quinones in photosynthetic reaction centers (RCs) using FTIR DS in combination with ONIOM type QM/MM vibrational frequency calculations. In particular, quinones in the A_1 binding site in PS I, and in the Q_A binding site in purple bacterial RCs were studied.

PhQ has a long hydrocarbon (phytyl) chain. 2MNQ is a PhQ analogue in which the hydrocarbon chain is replaced with a hydrogen atom. To evaluate if the hydrocarbon chain of PhQ influences FTIR difference spectra, we compared spectra obtained using PS I particles with PhQ and 2MNQ incorporated into the A_1 binding site. ONIOM type QM/MM calculations aimed at modeling the experimental (2MNQ-PhQ) A_1^-/A_1 FTIR DS were also undertaken. The calculated spectrum agrees well with the experimental spectrum. The calculations indicate that the hydrocarbon chain of PhQ does not significantly modify the orientation of PhQ or PhQ^- in the A_1 binding site, compared to 2MNQ.

To test the appropriateness of the computational methods, and to further investigate whether the presence of the hydrocarbon chain constrains the quinone ring, calculations were undertaken for several different quinones in the Q_A binding site. In particular chain containing and corresponding chain-less UQ and PhQ species were studies. The calculated spectra are very similar for incorporated quinones with and without a hydrocarbon chain, again suggesting that the hydrocarbon chain does not constrain the quinone ring in the protein binding site.

Our studies help in better understanding the role of hydrocarbon chain in the Q_A binding site. The available literature indicates that the hydrocarbon chain in the Q_A binding site plays an important role in the binding free energies for UQ and menaquinones. It was also found that

competitive interference of quinone function can be effectively inhibited by *in vivo* tail-protein interaction by amphiphilic species present in the native membrane [154].

ONIOM type QM/MM calculations were an essential aid in assigning bands to the vibrational modes of PhQ and PhQ^- (and 2MNQ and $2MNQ^-$) in TRSS A_1^-/A_1 FTIR DS. In experimental spectra, a band at 1494 cm^{-1} was observed and assigned (based on computational modeling) to a C_1⋯O stretching vibrational mode of PhQ^-. The corresponding mode of $2MNQ^-$ was found at 1505 cm^{-1} and assigned similarly. A band at 1415 cm^{-1} was observed and assigned to a C_4⋯O stretching vibrational mode of PhQ^-. The corresponding mode appears at 1427 cm^{-1} for $2MNQ^-$.

Based on the accumulated results from several sets of experiments bands of neutral PhQ were identified at 1656 and 1596 cm^{-1} and assigned (via calculation) to C_1=O and C_4=O modes of neutral PhQ, respectively. ONIOM calculations predict that upon binding at the A_1 site, the C_4=O mode of PhQ and PhQ^- are downshifted ~60 and 80 cm^{-1} relative to the C_1=O mode, respectively. The C_1=O group is essentially free from hydrogen bonding while the C_4=O group is very strongly hydrogen bonded. Such strong hydrogen bonding has been observed in other systems. For example, intramolecular hydrogen bonding interactions in β-hydroxylated naphthoquinones and anthraquinones cause downshifts of C=O modes by 30~80 cm^{-1} [164, 165]. For Lewis acids interacting with carbonyl groups, notably with phenyl ketones [166] C=O mode downshifts of 70~180 cm^{-1} have been documented. Hence, a 60~80 cm^{-1} downshift of the C_4=O mode for PhQ or PhQ^- observed in our studies is not totally unprecedented.

We also studied isotope edited Q_A^-/Q_A FTIR DS, by comparing ONIOM based calculations to experimental spectra. For neutral UQ in the Q_A binding site, the C_4=O mode of UQ downshifted ~32 cm^{-1} due to the H-bonding. This downshift indicated that the formed H-

bond of C_4=O group of UQ with the Q_A binding site was not strong. Isotope edited difference spectra calculated with ONIOM methods were similar when H-bonding amino acids were treated at the MM level and at the QM level. This result further supports that the H-bonding to neutral UQ in the Q_A binding site is relatively weak and can be considered in purely electrostatic terms.

The differences in H-bonding to two C=O groups of UQ would cause separation of two C=O modes. Our studies showed that the H-bond to the C_4=O group (provided by the side chain NH group of HisM219) was stronger than the H-bond to the C_1=O group (provided by the backbone NH group of AlaM260).

Previous studies show that the reduction potential for PhQ in the A_1 binding site was -800 mV [167], compared to -190 mV for UQ or menaquinone in the Q_A binding site [168], and the difference could be due to their different structures of the hydrocarbon chain. Another study suggested that the strong hydrogen bonds, possibly from the enveloping proteins, make quinones more reducible [169]. In our study with quinones in the PS I and purple bacteria RCs, time-resolved (TR) FTIR DS in combination with ONIOM calculations suggests that the single H-bonding to quinone is very strong in the A_1 binding site, while the H-bonding to quinone is relatively weak and asymmetric in the Q_A binding site. Therefore, the work presented here suggests that the reduction potential of quinone is more negative in the A_1 binding site than in Q_A binding site, because of the stronger H-bond.

6.2 Future work

The work presented here has shown that ONIOM type QM/MM vibrational frequency calculations are an essential tool for assigning bands in FTIR DS associated with cofactors in protein binding sites.

TR A_1^-/A_1 FTIR DS obtained using PS I particles with supposedly plastoquinone incorporated (from *men*B mutants) is dominated by bands associated with ^{3}P700, indicating that, under our conditions, the A_1 bind site is empty, or the quinine in the binding site does not support forward electron transfer, in a large fraction of the PS I particles [83]. However, EPR studies of *men*B mutant PS I showed that PQ9 is present in the A_1 site, and it functions as an efficient cofactor in electron transfer [78]. How or whether the hypotheses proposed from EPR studies are compatible with FTIR DS studies is still an open question. ONIIOM calculations of plastoquinone incorporated into the A_1binding site could be used to interpret these experimental results.

We have undertaken ONIOM calculations for the neutral state of UQ in the Q_A binding site. However, ONIOM calculations for UQ^- in the Q_A binding site have yet to be presented.

Experimental Q_B^-/Q_B isotope edited FTIR DS have been obtained. Although the reconstitution of purple bacterial RCs with isotope labeled quinones allowed separation of quinone bands from those of the protein, the interpretation of the spectra is still purely qualitative. No computational studies have been undertaken in the attempt to model the Q_B^-/Q_B isotope edited FTIR DS.

The X-ray crystal structures of the mutant RCs Pro-L209→ Tyr, Pro-L209 →Phe, and Pro-L209→Glu have revealed that Q_B occupies a proximal, intermediate, and distal position in these three mutants, respectively. However, all Q_B^-/Q_B FTIR DS obtained using the above mutants are similar to wild type. ONIOM type calculations may be a useful tool to address this issue. The various locations and orientations of Q_B observed in the different crystallographic structures of the RC can be explained by the Q_B model whose ONIOM calculated frequencies agree with experimental measurements. In addition, comparison of vibrational modes of UQ in

Q_A and Q_B binding sites would enable the comparison of the interaction between UQ and protein in different binding sites.

We have shown that TR FTIR DS is a useful tool for probing the substituents of quinones in protein binding sites. Similar experiments for different quinones incorporated into A_1 binding site can be designed to investigate the role of other quinine functional groups, such as the methyl group of the quinone ring. In addition, more experimental data (specific isotope labeling of incorporated quinones, in combination with computational work, are required to establish band assignments unambiguously.

REFERENCES

1. Balzani, V., A. Credi, and M. Venturi, *Photochemical Conversion of Solar Energy.* ChemSusChem, 2008. **1**(1-2): p. 26-58.
2. Morton, O., *Solar energy: a new day dawning? Silicon Valley sunrise.* Nature, 2006. **443**(7107): p. 19-22.
3. Olson, J.M., *Evolution of photosynthetic reaction centers.* Biosystems, 1981. **14**(1): p. 89-94.
4. Jordan, P., et al., *Three-dimensional structure of cyanobacterial photosystem I at 2.5 angstrom resolution.* Nature, 2001. **411**(6840): p. 909-917.
5. Sétif, P., *Ferredoxin and flavodoxin reduction by photosystem I.* Biochimica et Biophysica Acta (BBA) - Bioenergetics, 2001. **1507**(1–3): p. 161-179.
6. Chitnis, V.P. and P.R. Chitnis, *PsaL subunit is required for the formation of photosystem I trimers in the cyanobacterium Synechocystis sp. PCC 6803.* FEBS Letters, 1993. **336**(2): p. 330-334.
7. Xu, Q., et al., *Mutational Analysis of Photosystem I Polypeptides in the Cyanobacterium Synechocystis sp. PCC 6803. TARGETED INACTIVATION OF psaI REVEALS THE FUNCTION OF PsaI IN THE STRUCTURAL ORGANIZATION OF PsaL.* Journal of Biological Chemistry, 1995. **270**(27): p. 16243-16250.
8. Fromme, P. and I. Grotjohann, *Structural Analysis of Cyanobacterial Photosystem I*, in *Photosystem I: The Light Driven Plastocyanin:Ferredoxin Oxidoreductase.*, J.H. Golbeck, Editor. 2006, Springer: Dordrecht. p. 47-69.
9. Ben-Shem, A., F. Frolow, and N. Nelson, *Light-Harvesting Features Revealed by the Structure of Plant Photosystem I.* Photosynthesis Research, 2004. **81**(3): p. 239-250.

10. Lunde, C., et al., *The PSI-H subunit of photosystem I is essential for state transitions in plant photosynthesis.* Nature, 2000. **408**(6812): p. 613-615.

11. Haldrup, A., H. Naver, and H.V. Scheller, *The interaction between plastocyanin and photosystem I is inefficient in transgenic Arabidopsis plants lacking the PSI-N subunit of photosystem.* The Plant Journal, 1999. **17**(6): p. 689-698.

12. Jensen, P.E., et al., *The PSI-O Subunit of Plant Photosystem I Is Involved in Balancing the Excitation Pressure between the Two Photosystems.* Journal of Biological Chemistry, 2004. **279**(23): p. 24212-24217.

13. Guergova-Kuras, M., et al., *Evidence for two active branches for electron transfer in photosystem I.* Proc. Natl. Acad. Sci. U S A, 2001. **98**(8): p. 4437-4442.

14. Muhiuddin, I.P., et al., *Evidence from time resolved studies of the P700(.+)/A1(.-) radical pair for photosynthetic electron transfer on both the PsaA and PsaB branches of the photosystem I reaction centre.* FEBS Lett, 2001. **503**(1): p. 56-60.

15. Hastings, G. and V. Sivakumar, *A Fourier transform infrared absorption difference spectrum associated with the reduction of A(1) in photosystem I: Are both phylloquinones involved in electron transfer?* Biochemistry, 2001. **40**(12): p. 3681-3689.

16. Brettel, K., *Electron transfer and arrangement of the redox cofactors in photosystem I.* Biochim. Biophys. Acta, 1997. **1318**(3): p. 322-373.

17. Brettel, K. and W. Leibl, *Electron transfer in photosystem I.* Biochimica et Biophysica Acta (BBA) - Bioenergetics, 2001. **1507**(1–3): p. 100-114.

18. Luneberg, J., et al., *Spectroscopic Characterization of PS-I Core Complexes from Thermophilic Synechococcus Sp - Identical Reoxidation Kinetics of a(1)(-) before and*

after Removal of the Iron-Sulfur-Clusters F-a and F-B. FEBS Lett., 1994. **338**(2): p. 197-202.

19. Sivakumar, V., *Static and Time resolved FTIR Difference Spectroscopy for the Study of A_1, the Secondary Electron Acceptor in Photosystem I*, in *Physics and Astronomy*. 2004, Georgia State University.
20. Agalarov, R. and K. Brettel, *Temperature dependence of biphasic forward electron transfer from the phylloquinone(s) A1 in photosystem I: only the slower phase is activated.* Biochim. Biophys. Acta, 2003. **1604**(1): p. 7-12.
21. Schlodder, E., et al., *Temperature dependence of forward and reverse electron transfer from A_1^-, the reduced secondary electron acceptor in photosystem I.* Biochem., 1998. **37**(26): p. 9466-9476.
22. Holzwarth, A.R., et al., *Ultrafast transient absorption studies on photosystem I reaction centers from Chlamydomonas reinhardtii. 2: mutations near the P700 reaction center chlorophylls provide new insight into the nature of the primary electron donor.* Biophysical journal, 2006. **90**(2): p. 552-565.
23. Shelaev, I.V., et al., *Femtosecond primary charge separation in Synechocystis sp. PCC 6803 photosystem I.* Biochimica et Biophysica Acta (BBA) - Bioenergetics, 2010. **1797**(8): p. 1410-1420.
24. Ptushenko, V., et al., *Semi-continuum electrostatic calculations of redox potentials in photosystem I.* Photosynthesis Research, 2008. **97**(1): p. 55-74.
25. Stowell, M.H., et al., *Light-induced structural changes in photosynthetic reaction center: implications for mechanism of electron-proton transfer.* Science, 1997. **276**(5313): p. 812-816.

26. Martin, J.-L., et al., *Femtosecond spectroscopy of electron transfer in the reaction center of the photosynthetic bacterium Rhodopseudomonas sphaeroides R-26: Direct electron transfer from the dimeric bacteriochlorophyll primary donor to the bacteriopheophytin acceptor with a time constant of 2.8 ± 0.2 psec.* Proceedings of the National Academy of Sciences, 1986. **83**(4): p. 957-961.

27. Arlt, T., et al., *The accessory bacteriochlorophyll: a real electron carrier in primary photosynthesis.* Proceedings of the National Academy of Sciences, 1993. **90**(24): p. 11757-11761.

28. Kirmaier, C. and D. Holten, *Evidence that a distribution of bacterial reaction centers underlies the temperature and detection-wavelength dependence of the rates of the primary electron-transfer reactions.* Proceedings of the National Academy of Sciences, 1990. **87**(9): p. 3552-3556.

29. Tiede, D.M., et al., *Time-Resolved Electrochromism Associated with the Formation of Quinone Anions in the Rhodobacter sphaeroides R26 Reaction Center†.* Biochemistry, 1996. **35**(33): p. 10763-10775.

30. Okamura, M.Y. and G. Feher, *Proton Transfer in Reaction Centers from Photosynthetic Bacteria.* Annual Review of Biochemistry, 1992. **61**(1): p. 861-896.

31. Gunner, C.A.W.a.M.R., *The Acceptor Quinones of Purple Photosynthetic Bacteria—Structure and Spectroscopy*, in *The Purple Phototrophic Bacteria*, F.D. C. Neil Hunter, Marion C. Thurnauer and J. Thomas Beatty, Editor. 2008, Springer: The Netherlands. p. 379-405.

32. Axelrod, H., O. Miyashita, and M. Okamura, *Structure and Function of the Cytochrome c 2:Reaction Center Complex from Rhodobacter sphaeroides*, in *The Purple Phototrophic Bacteria*, C.N. Hunter, et al., Editors. 2009, Springer Netherlands. p. 323-336.

33. Leonova, M.M., et al., *Structure-function investigations of bacterial photosynthetic reaction centers.* Biochemistry (Moscow), 2011. **76**(13): p. 1465-1483.

34. Malkin, R., *On the function of two vitamin K1 molecules in the PS I electron acceptor complex.* FEBS Letters, 1986. **208**(2): p. 343-346.

35. Snyder, S.W., et al., *Direct assignment of vitamin K1 as the secondary acceptor A1 in photosystem I.* Proceedings of the National Academy of Sciences, 1991. **88**(21): p. 9895-9896.

36. Ishikita, H. and E.-W. Knapp, *Redox Potential of Quinones in Both Electron Transfer Branches of Photosystem I.* Journal of Biological Chemistry, 2003. **278**(52): p. 52002-52011.

37. Prince, R.C., P. Leslie Dutton, and J. Malcolm Bruce, *Electrochemistry of ubiquinones: Menaquinones and plastoquinones in aprotic solvents.* FEBS Letters, 1983. **160**(1–2): p. 273-276.

38. Mula, S., et al., *Introduction of a Hydrogen Bond between Phylloquinone PhQA and a Threonine Side-Chain OH Group in Photosystem I.* The Journal of Physical Chemistry B, 2012. **116**(48): p. 14008-14016.

39. Srinivasan, N., et al., *Alteration of the H-Bond to the A1A Phylloquinone in Photosystem I: Influence on the Kinetics and Energetics of Electron Transfer.* The Journal of Physical Chemistry B, 2011. **115**(8): p. 1751-1759.

40. Santabarbara, S., et al., *Interquinone Electron Transfer in Photosystem I As Evidenced by Altering the Hydrogen Bond Strength to the Phylloquinone(s).* The Journal of Physical Chemistry B, 2010. **114**(28): p. 9300-9312.

41. Xu, W., et al., *Electron transfer in cyanobacterial photosystem I: I. Physiological and spectroscopic characterization of site-directed mutants in a putative electron transfer pathway from A_0 through A_1 to F_X.* J. Biol. Chem., 2003. **278**(30): p. 27864-27875.

42. Xu, W., et al., *Electron transfer in cyanobacterial photosystem I: II. Determination of forward electron transfer rates of site-directed mutants in a putative electron transfer pathway from A_0 through A_1 to F_X.* J. Biol. Chem., 2003. **278**(30): p. 27876-27887.

43. Kaupp, M., *The function of photosystem I. Quantum chemical insight into the role of tryptophan-quinone interactions.* Biochemistry, 2002. **41**(9): p. 2895-2900.

44. Boudreaux, B., et al., *Mutations in both sides of the photosystem I reaction center identify the phylloquinone observed by electron paramagnetic resonance spectroscopy.* J Biol Chem, 2001. **276**(40): p. 37299-37306.

45. Lin, T.-J. and P.J. O'Malley, *Binding Site Influence on the Electronic Structure and Electron Paramagnetic Resonance Properties of the Phyllosemiquinone Free Radical of Photosystem I.* The Journal of Physical Chemistry B, 2011. **115**(29): p. 9311-9319.

46. Brudler, R., et al., *Asymmetric binding of the 1- and 4-C=O groups of QA in Rhodobacter sphaeroides R26 reaction centres monitored by Fourier transform infra-red spectroscopy using site-specific isotopically labelled ubiquinone-10.* Embo J, 1994. **13**(23): p. 5523-30.

47. Breton, J., et al., *Binding sites of quinones in photosynthetic bacterial reaction centers investigated by light-induced FTIR difference spectroscopy: assignment of the*

interactions of each carbonyl of Q_A in Rhodobacter sphaeroides using site-specific ^{13}C-labeled ubiquinone. Biochem., 1994. **33**(48): p. 14378-14386.

48. Lamichhane, H.P., *Calculated Vibrational Properties of Quinones in Photosynthetic Reaction Center*, in *Physics and Astronomy*. 2011, Georgia State University: Atlanta. p. 175.

49. Flores, M., et al., *Protein-cofactor interactions in bacterial reaction centers from Rhodobacter sphaeroides R-26: II. Geometry of the hydrogen bonds to the primary quinone formula by 1H and 2H ENDOR spectroscopy.* Biophys J, 2007. **92**(2): p. 671-82.

50. Lin, T.-J. and P.J. O'Malley, *An ONIOM study of the QA site semiquinone in the Rhodobacter sphaeroides photosynthetic reaction centre.* Journal of Molecular Structure: THEOCHEM, 2008. **870**(1–3): p. 31-35.

51. Ke, B., *Photosynthesis: Photobiochemistry and Photobiophysics*. Advances in photosynthesis ; v. 10. Vol. 10. 2001, Dordrecht ; Boston: Kluwer Academic Publishers.

52. Utschig, L.M., et al., *Influence of Iron-Removal Procedures on Sequential Electron Transfer in Photosynthetic Bacterial Reaction Centers Studied by Transient EPR Spectroscopy†.* Biochemistry, 1997. **36**(28): p. 8548-8558.

53. Debus, R.J., G. Feher, and M.Y. Okamura, *Iron-depleted reaction centers from Rhodopseudomonas sphaeroides R-26.1: characterization and reconstitution with iron(2+), manganese(2+), cobalt(2+), nickel(2+), copper(2+), and zinc(2+).* Biochemistry, 1986. **25**(8): p. 2276-2287.

54. Twardowski, J. and P. Anzenbacker, *Raman and IR Spectroscopy in Biology and Biochemistry*. 1994, Chichester: Ellis Horwood.

55. Smith, B.C., *Infrared spectral interpretation : a systematic approach*. 1999, Boca Raton: CRC Press.

56. Stuart, B., *Infrared Spectroscopy: Fundamentals and Applications*. 2004: John Wiley & Sons, Ltd.

57. Wang, R., *FTIR Difference Spectroscopy for the Study of P700, the Primary Electron Donor in Photosystem I*, in *Physics and Astronomy*. 2005, Georgia State University: Atlanta. p. 233.

58. Griffiths, P. and J. de Haseth, *Fourier Transform Infrared Spectrometry. Second Edition*. 2007: JOHN WILEY & SONS, INC.

59. Schrader, B., *Infrared and raman spectrascopy method and application*. 1995: VCH.

60. Dapprich, S., et al., *A new ONIOM implementation in Gaussian98. Part I. The calculation of energies, gradients, vibrational frequencies and electric field derivatives.* Journal of Molecular Structure: THEOCHEM, 1999. **461–462**(0): p. 1-21.

61. Vreven, T., et al., *Geometry optimization with QM/MM, ONIOM, and other combined methods. I. Microiterations and constraints.* J Comput Chem, 2003. **24**(6): p. 760-9.

62. Rauhut, G. and P. Pulay, *Transferable Scaling Factors for Density-Functional Derived Vibrational Force-Fields.* Journal of Physical Chemistry, 1995. **99**(10): p. 3093-3100.

63. Zhao, N. and G. Hastings, *On the Nature of the Hydrogen Bonds to Neutral Ubiquinone in the QA Binding Site in Purple Bacterial Photosynthetic Reaction Centers.* The Journal of Physical Chemistry B, 2013. **117**(29): p. 8705-8713.

64. Zhao, N., H.P. Lamichanne, and G. Hastings, *Comparison of calculated and experimental isotope edited FTIR difference spectra for purple bacterial photosynthetic*

reaction centers with different quinones incorporated into the QA binding site. Frontiers in Plant Science, 2013. **4**.

65. Golbeck, J.H. and D. Bryant, *Photosystem I*, in *Current topics in bioenergetics*. 1991, Academic Press: New York. p. 83-175.
66. Vassiliev, I.R., M.L. Antonkine, and J.H. Golbeck, *Iron-sulfur clusters in type I reaction centers.* Biochim Biophys Acta, 2001. **1507**(1-3): p. 139-60.
67. Setif, P. and K. Brettel, *Forward electron transfer from phylloquinone A1 to iron-sulfur centers in spinach photosystem I.* Biochemistry, 1993. **32**(31): p. 7846-7854.
68. Srinivasan, N. and J.H. Golbeck, *Protein–cofactor interactions in bioenergetic complexes: The role of the A1A and A1B phylloquinones in Photosystem I.* Biochimica et Biophysica Acta (BBA) - Bioenergetics, 2009. **1787**(9): p. 1057-1088.
69. Niklas, J., et al., *Electronic Structure of the Quinone Radical Anion A1•− of Photosystem I Investigated by Advanced Pulse EPR and ENDOR Techniques.* The Journal of Physical Chemistry B, 2009. **113**(30): p. 10367-10379.
70. Karyagina, I., et al., *Single-sided hydroge bonding to the quinone cofactor in photosystem I probed by selective13C-labelled naphthoquinones and transient EPR.* Applied Magnetic Resonance, 2006. **30**(3-4): p. 287-310.
71. Srinivasan, N., et al., *Role of the Hydrogen Bond from Leu722 to the A1A Phylloquinone in Photosystem I†‡.* Biochemistry, 2009. **48**(15): p. 3315-3324.
72. Pushkar, Y.N., et al., *Asymmetric hydrogen-bonding of the quinone cofactor in photosystem I probed by C-13-labeled naphthoquinones.* Journal of Physical Chemistry B, 2004. **108**(27): p. 9439-9448.

73. Pushkar, Y.N., et al., *An EPR/ENDOR study of the asymmetric hydrogen bond between the quinone electron acceptor and the protein backbone in photosystem I.* Journal of Molecular Structure, 2004. **700**(1-3): p. 233-241.

74. Stehlik, D., *Transient EPR Spectroscopy as Applied to Light-Induced Functional Intermediates Along the Electron Transfer Pathway In Photosystem I*, in *Photosystem I: The Light Driven Plastocyanin:Ferredoxin Oxidoreductase.*, J. Golbeck, Editor. 2006, Springer: Dordrecht. p. 361-386.

75. Biggins, J., *Evaluation of selected benzoquinones, naphthoquinones, and anthraquinones as replacements for phylloquinone in the A1 acceptor site of the photosystem I reaction center.* Biochemistry, 1990. **29**(31): p. 7259-7264.

76. Sieckman, I., et al., *Nanosecond electron transfer kinetics in photosystem I following substitution of quinones for vitamin K1 as studied by time resolved EPR.* FEBS Lett, 1991. **284**(1): p. 98-102.

77. Pushkar, Y., et al., *Orientation and Protein-Cofactor Interactions of Monosubstituted n-Alkyl Naphthoquinones in the A_1 Binding Site of Photosystem I.* J. Phys. Chem. B, 2002. **106**: p. 12052-12058.

78. Johnson, T.W., et al., *Recruitment of a foreign quinone into the A_1 site of photosystem I. I. Genetic and physiological characterization of phylloquinone biosynthetic pathway mutants in Synechocystis sp. pcc 6803.* J. Biol. Chem., 2000. **275**(12): p. 8523-8530.

79. Zybailov, B., et al., *Recruitment of a Foreign Quinone into the A1 Site of Photosystem I: II. STRUCTURAL AND FUNCTIONAL CHARACTERIZATION OF PHYLLOQUINONE BIOSYNTHETIC PATHWAY MUTANTS BY ELECTRON PARAMAGNETIC*

RESONANCE AND ELECTRON-NUCLEAR DOUBLE RESONANCE SPECTROSCOPY. Journal of Biological Chemistry, 2000. **275**(12): p. 8531-8539.

80. Johnson, T.W., et al., *The menD and menE homologs code for 2-succinyl-6-hydroxyl-2, 4-cyclohexadiene-1-carboxylate synthase and O-succinylbenzoic acid-CoA synthase in the phylloquinone biosynthetic pathway of Synechocystis sp PCC 6803.* Biochim. Biophys. Acta, 2003. **1557**(1-3): p. 67-76.

81. Semenov, A.Y., et al., *Recruitment of a foreign quinone into the A_1 site of photosystem I. Altered kinetics of electron transfer in phylloquinone biosynthetic pathway mutants studied by time-resolved optical, EPR, and electrometric techniques.* J. Biol. Chem., 2000. **275**(31): p. 23429-23438.

82. Sivakumar, V., R. Wang, and G. Hastings, *A1 Reduction in Intact Cyanobacterial Photosystem I Particles Studied by Time-Resolved Step-Scan Fourier Transform Infrared Difference Spectroscopy and Isotope Labeling†.* Biochemistry, 2005. **44**(6): p. 1880-1893.

83. Bandaranayake, K.M.P., et al., *Time-Resolved FTIR Difference Spectroscopy for the Study of Photosystem I Particles with Plastoquinone-9 Occupying the A1 Binding Site†.* Biochemistry, 2006. **45**(42): p. 12733-12740.

84. Bandaranayake, K.M.P., R. Wang, and G. Hastings, *Modification of the Phylloquinone in the A1 Binding Site in Photosystem I Studied Using Time-Resolved FTIR Difference Spectroscopy and Density Functional Theory†.* Biochemistry, 2006. **45**(13): p. 4121-4127.

85. Hastings, G. and P. Banderanayake, *(ˉ-A_1) FTIR difference spectra obtained using photosystem I particles with O-18 and specifically C-13 labeled quinones occupying the A_1 Binding SitA_1r.* Photosynthesis Research, 2007. **91**(2-3): p. 149-149.

86. Hastings, G. and K. Bandaranayake, *Quinone anion bands in A_1^-/A_1 FTIR difference spectra investigated using photosystem I particles with specifically labeled Naphthoquinones incorporated into the A_1 binding site.*, in *Photosynthesis. Energy from the Sun. Procedings of the 14th International Congress on Photosynthesis Research*, J. Allen, et al., Editors. 2008, Springer. p. 69-72.

87. Hastings, G., K.M. Bandaranayake, and E. Carrion, *Time-resolved FTIR difference spectroscopy in combination with specific isotope labeling for the study of A1, the secondary electron acceptor in photosystem 1.* Biophysical journal, 2008. **94**(11): p. 4383-4392.

88. Rappe, A.K., et al., *Uff, a Full Periodic-Table Force-Field for Molecular Mechanics and Molecular-Dynamics Simulations.* Journal of the American Chemical Society, 1992. **114**(25): p. 10024-10035.

89. Wang, R., et al., *FTIR difference spectroscopy in combination with isotope labeling for identification of the carbonyl modes of P700 and P700+ in photosystem I.* Biophysical journal, 2004. **86**(2): p. 1061-1073.

90. Bandaranayake, K.M.P., et al., *Modeling the A(1) binding site in photosystem - I. Density functional theory for the calculation of "anion-neutral" FTIR difference spectra of phylloquinone.* Vibrational Spectroscopy, 2006. **42**(1): p. 78-87.

91. Frisch, M.J., et al., *Gaussian 03, Revision C.02.* Gaussian 03, Revision D.01, 2004.

92. Iwaki, M. and S. Itoh, *Electron transfer in spinach photosystem I reaction center containing benzo-, naphtho- and anthraquinones in place of phylloquinone.* FEBS Letters, 1989. **256**(1–2): p. 11-16.

93. Iwaki, M. and S. Itoh, *Reaction of Reconstituted Acceptor Quinone and Dynamic Equilibration of Electron Transfer in the Photosystem I Reaction Center.* Plant and Cell Physiology, 1994. **35**(7): p. 983-993.

94. Moser, C.C., et al., *Nature of biological electron transfer.* Nature, 1992. **355**(6363): p. 796-802.

95. Moser, C., et al., *Biological electron transfer.* Journal of Bioenergetics and Biomembranes, 1995. **27**(3): p. 263-274.

96. Page, C.C., et al., *Natural engineering principles of electron tunnelling in biological oxidation-reduction.* Nature, 1999. **402**(6757): p. 47-52.

97. Moser, C.C., et al., *Length, time, and energy scales of photosystems*, in *Advances in Protein Chemistry*, C.R. Douglas, Editor. 2003, Academic Press. p. 71-109.

98. Itoh, S., M. Iwaki, and I. Ikegami, *Modification of photosystem I reaction center by the extraction and exchange of chlorophylls and quinones.* Biochim. Biophys. Acta., 2001. **1507**(1-3): p. 115-138.

99. Vos, M. and H. van Gorkom, *Thermodynamics of Photosystem I Studied By Electric Field Stimulated Charge Recombination.* Biochimica et Biophysica Acta, 1988. **934**: p. 293-302.

100. O'Malley, P.J., *Density functional calculated spin densities and hyperfine couplings for hydrogen bonded 1,4-naphthosemiquinone and phyllosemiquinone anion radicals: a model for the A1 free radical formed in Photosystem I.* Biochimica et Biophysica Acta (BBA) - Bioenergetics, 1999. **1411**(1): p. 101-113.

101. Hastings, G., et al., *Primary donor photo-oxidation in photosystem I: A re-evaluation of (P700(+)-P700) Fourier transform infrared difference spectra.* Biochemistry, 2001. **40**(43): p. 12943-12949.

102. Bender, S.L., et al., *The vibrational spectrum of the secondary electron acceptor, A1, in photosystem I.* The Journal of Physical Chemistry B, 2008. **112**(12): p. 3844-52.

103. Hastings, G., et al., *Excited state dynamics in photosystem I: Effects of detergent and excitation wavelength.* Biophysical Journal, 1995. **69**(5): p. 2044-2055.

104. Hastings, G., et al., *Universality of Energy and Electron-Transfer Processes in Photosystem-I.* Biochemistry, 1995. **34**(47): p. 15512-15522.

105. Johnson, T.W., et al., *Recruitment of a foreign quinone into the A_1 site of photosystem I. In vivo replacement of plastoquinone-9 by media-supplemented naphthoquinones in phylloquinone biosynthetic pathway mutants of Synechocystis sp. PCC 6803.* J. Biol. Chem., 2001. **276**(43): p. 39512-39521.

106. Barth, A., *Infrared spectroscopy of proteins.* Biochimica et Biophysica Acta (BBA) - Bioenergetics, 2007. **1767**(9): p. 1073-1101.

107. Breton, J., *Fourier transform infrared spectroscopy of primary electron donors in type I photosynthetic reaction centers.* Biochim. Biophys. Acta, 2001. **1507**(1-3): p. 180-193.

108. Pantelidou, M., P.R. Chitnis, and J. Breton, *FTIR Spectroscopy of Synechocystis 6803 Mutants Affected on the Hydrogen Bonds to the Carbonyl Groups of the PsaA Chlorophyll of P700 Supports an Extensive Delocalization of the Charge in P700+†.* Biochemistry, 2004. **43**(26): p. 8380-8390.

109. Breton, J., et al., *The binding sites of quinones in photosynthetic bacterial reaction centers investigated by light-induced FTIR difference spectroscopy: assignment of the Q_A*

vibrations in Rhodobacter sphaeroides using ^{18}O- or ^{13}C-labeled ubiquinone and vitamin K_1. Biochemistry, 1994. **33**(16): p. 4953-4965.

110. Trumpower, B., *Function of Quinones in Energy Conserving Systems*. 1982: Academic Press.

111. Ke, B., *The "Stable" Primary Electron Acceptor (Q_A) of Photosynthetic Bacteria*, in *Photosynthesis: Photobiochemistry and Photobiophysics*. 2001, Kluwer Academic Publishers: Dordrecht ; Boston. p. 101-110.

112. Ke, B., *The Secondary Electron Acceptor (Q_B) in Photosynthetic Bacteria*, in *Photosynthesis: Photobiochemistry and Photobiophysics*. 2001, Kluwer Academic Publishers: Dordrecht ; Boston. p. 111-128.

113. Mantele, W., *Reaction-induced infrared difference spectroscopy for the study of protein function and reaction mechanisms.* Trends Biochem Sci, 1993. **18**(6): p. 197-202.

114. Zscherp, C. and A. Barth, *Reaction-induced infrared difference spectroscopy for the study of protein reaction mechanisms.* Biochemistry, 2001. **40**(7): p. 1875-83.

115. Breton, J. and E. Nabedryk, *Protein-quinone interactions in the bacterial photosynthetic reaction center: Light-induced FTIR difference spectroscopy of the quinone vibrations.* Biochim. Biophys. Acta, 1996. **1275**(1-2): p. 84-90.

116. Thiel, W., *QM/MM Methodology: Fundamentals, Scope, and Limitations*, in *Multiscale Simulation Methods in Molecular Sciences*, J. Grotendorst, et al., Editors. 2009. p. 203-214.

117. Lamichhane, H.P. and G. Hastings, *Calculated vibrational properties of pigments in protein binding sites.* Proceedings of the National Academy of Sciences, 2011. **108**(26): p. 10526-10531.

118. Vreven, T., et al., *Combining quantum mechanics methods with molecular mechanics methods in ONIOM.* Journal of Chemical Theory and Computation, 2006. **2**(3): p. 815-826.

119. Gilli, G. and P. Gilli, *The Nature of the Hydrogen Bond. Outline of a Comprehensive Hydrogen Bond Theory*. IUCr Monographs in crystallography. 2009: Oxford University Press.

120. Scheiner, S., *Hydrogen Bonding: A Theoretical Perspective*. 1997: Oxford University Press.

121. Dannenberg, J.J., L. Haskamp, and A. Masunov, *Are hydrogen bonds covalent or electrostatic? A molecular orbital comparison of molecules in electric fields and H-bonding environments.* Journal of Physical Chemistry A, 1999. **103**(35): p. 7083-7086.

122. Sinnecker, S., M. Flores, and W. Lubitz, *Protein-cofactor interactions in bacterial reaction centers from Rhodobacter sphaeroides R-26: Effect of hydrogen bonding on the electronic and geometric structure of the primary quinone. A density functional theory study.* Physical Chemistry Chemical Physics, 2006. **8**(48): p. 5659-5670.

123. Case, D.A., et al., *The Amber biomolecular simulation programs.* Journal of Computational Chemistry, 2005. **26**(16): p. 1668-1688.

124. Mulliken, R., *Electronic Population Analysis on LCAO MO Molecular Wave Functions. I.* J. Chem. Phys., 1955. **23**(10): p. 1833-1840.

125. Foster, J.P. and F. Weinhold, *Natural hybrid orbitals.* Journal of the American Chemical Society, 1980. **102**(24): p. 7211-7218.

126. Reed, A.E., L.A. Curtiss, and F. Weinhold, *Intermolecular interactions from a natural bond orbital, donor-acceptor viewpoint.* Chemical Reviews, 1988. **88**(6): p. 899-926.

127. Weinhold, F., *Nature of H-bonding in clusters, liquids, and enzymes: an ab initio, natural bond orbital perspective.* Journal of Molecular Structure-Theochem, 1997. **398**: p. 181-197.

128. Martin, J.M.L. and C. Van Alsenoy, *GAR2PED*. 1995: University of Antwerp.

129. Bakowies, D. and W. Thiel, *Hybrid Models for Combined Quantum Mechanical and Molecular Mechanical Approaches.* J. Phys. Chem. A, 1996. **100**(25): p. 10580-10594.

130. Lin, H. and D.G. Truhlar, *QM/MM: what have we learned, where are we, and where do we go from here?* Theoretical Chemistry Accounts, 2007. **117**(2): p. 185-199.

131. Wadt, P.J.H.a.W.R., *Ab initio effective core potentials for molecular calculations. Potentials for the transition metal atoms Sc to Hg.* 1985. **82**(1): p. 270-283.

132. Agnieszka Halas, V.D., Pierre Sebban, Krzysztof Matlak, Józef Korecki, Jerzy Kruk, Kvˇetoslava Burda, *Chemical proprieties of the iron-quinone complex in mutated reaction centers of Rb. sphaeroides.* Hyperfine Interactions, 2012. **206**(1-3): p. 109-114

133. Orzechowska, A., et al., *Coupling of collective motions of the protein matrix to vibrations of the non-heme iron in bacterial photosynthetic reaction centers.* Biochimica Et Biophysica Acta-Bioenergetics, 2010. **1797**(10): p. 1696-1704.

134. Wraight, C.A. and M.R. Gunner, *The Acceptor Quinones of Purple Photosynthetic Bacteria—Structure and Spectroscopy*, in *The Purple Phototrophic Bacteria*, C. Hunter, et al., Editors. 2009, Springer. p. 379-405.

135. Chernev, P., et al., *Carboxylate Shifts Steer Interquinone Electron Transfer in Photosynthesis.* Journal of Biological Chemistry, 2011. **286**(7): p. 5368-5374.

136. Freindorf, M., et al., *Lennard-Jones parameters for the combined QM/MM method using the B3LYP/6-31+G*/AMBER potential.* J Comput Chem, 2005. **26**(12): p. 1270-1278.

137. Senthilkumar, K., et al., *Analysis of polarization in QM/MM modelling of biologically relevant hydrogen bonds.* Journal of the Royal Society Interface, 2008. **5**: p. S207-S216.

138. Nilsson, A., et al., *The hydrogen bond in ice probed by soft x-ray spectroscopy and density functional theory.* Journal of Chemical Physics, 2005. **122**(15).

139. Jeffrey, G., *An Introduction to Hydrogen Bonding*. Topics In Physical Chemistry. A series of advanced textbooks and monographs, ed. D. Truhlar. 1997, New York, Oxford: Oxford University Press.

140. Lamichhane, H., R. Wang, and G. Hastings, *Comparison of calculated and experimental FTIR spectra of specifically labeled ubiquinones.* Vibrational Spectroscopy, 2011. **55**(2): p. 279-286.

141. Grabowski, S.J., *Analysis of C = O center dot center dot center dot H-O interactions in organic crystal structures.* Tetrahedron, 1998. **54**(34): p. 10153-10160.

142. Grabowski, S.J., *A new measure of hydrogen bonding strength - ab initio and atoms in molecules studies.* Chemical Physics Letters, 2001. **338**(4-6): p. 361-366.

143. Grabowski, S.J., *Ab initio calculations on conventional and unconventional hydrogen bonds - Study of the hydrogen bond strength.* Journal of Physical Chemistry A, 2001. **105**(47): p. 10739-10746.

144. Parthasarathi, R. and V. Subramanian, *Characterization of Hydrogen Bonding: From van der Waals Interactions to Covalency*, in *Hydrogen Bonding—New Insights*, S. Grabowski, Editor. 2006, Springer: Dordrecht. p. 1-50.

145. Zhou, P.P. and W.Y. Qiu, *Red- and Blue-Shifted Hydrogen Bonds in the Cis-Trans Noncyclic Formic Acid Dimer.* Chemphyschem, 2009. **10**(11): p. 1847-1858.

146. Rozas, I., *On the nature of hydrogen bonds: an overview on computational studies and a word about patterns.* Physical Chemistry Chemical Physics, 2007. **9**(22): p. 2782-2790.

147. Umeyama, H. and K. Morokuma, *The Origin of Hydrogen Bonding. An Energy Decomposition Study.* Journal of the American Chemical Society, 1977. **99**(5): p. 1316-1332.

148. Reed, A.E., R.B. Weinstock, and F. Weinhold, *Natural population analysis.* Journal of Chemical Physics, 1985. **83**(2): p. 735.

149. Gilli, P., et al., *Covalent Nature of the Strong Homonuclear Hydrogen-Bond - Study of the O-H---O System by Crystal-Structure Correlation Methods.* Journal of the American Chemical Society, 1994. **116**(3): p. 909-915.

150. Ke, B., *The Bacterial Photosynthetic Reaction Center: Chemical Composition and Crystal Structure*, in *Photosynthesis: Photobiochemistry and Photobiophysics*. 2001, Kluwer Academic Publishers: Dordrecht; Boston. p. 47-62.

151. Ke, B., *The Stable Primary Acceptor Q_A and the Secondary Electron Acceptor Q_B,* in *Photosynthesis: Photobiochemistry and Photobiophysics*. 2001, Kluwer Academic Publishers: Dordrecht; Boston. p. 289-304.

152. Shopes, R.J. and C.A. Wraight, *The acceptor quinone complex of Rhodopseudomonas viridis reaction centers.* Biochimica et Biophysica Acta (BBA) - Bioenergetics, 1985. **806**(3): p. 348-356.

153. Hale, M.B., R.E. Blankenship, and R.C. Fuller, *Menaquinone is the sole quinone in the facultatively aerobic green photosynthetic bacterium Chloroflexus aurantiacus.* Biochimica et Biophysica Acta (BBA) - Bioenergetics, 1983. **723**(3): p. 376-382.

154. Warncke, K., et al., *Influence of Hydrocarbon Tail Structure on Quinone Binding and Electron-Transfer Performance at the Q(a) and Q(B) Sites of the Photosynthetic Reaction-Center Protein.* Biochemistry, 1994. **33**(25): p. 7830-7841.

155. McComb, J.C., R.R. Stein, and C.A. Wraight, *Investigations on the influence of headgroup substitution and isoprene side-chain length in the function of primary and secondary quinones of bacterial reaction centers.* Biochim Biophys Acta, 1990. **1015**(1): p. 156-71.

156. Noguchi, T. and C. Berthomieu, *Molecular Analysis by Vibrational Spectroscopy*, in *Photosystem II The Light Driven Water:Plastoquinone Oxidoreductase*, T. Wydrzynski and K. Satoh, Editors. 2005, Springer: Dordrecht. p. 367-387.

157. Breton, J., et al., *Binding sites of quinones in photosynthetic bacterial reaction centers investigated by light-induced FTIR difference spectroscopy: binding of chainless symmetrical quinones to the Q_A site of Rhodobacter sphaeroides.* Biochem., 1994. **33**(41): p. 12405-12415.

158. Lamichhane, H.P. and G. Hastings, *Calculated Vibrational Properties of Ubisemiquinones.* Computational Biology Journal, 2013. **2013**: p. 11.

159. Hucke, O., R. Schmid, and A. Labahn, *Exploring the primary electron acceptor (QA)-site of the bacterial reaction center from Rhodobacter sphaeroides. Binding mode of vitamin K derivatives.* Eur J Biochem, 2002. **269**(4): p. 1096-108.

160. Bandaranayake, K., et al., *Modeling The A_1 Binding Site In Photosystem I. Density Functional Theory For The Calculation Of "Anion – Neutral" FTIR Difference Spectra of Phylloquinone.* Vib. Spectrosc., 2006. **42**(1): p. 78-87.

161. Wheeler, R.A., *Quinones and quinoidal radicals in photosynthesis,* in *Theoretical Biochemistry-Processes and Properties of Biological Systems*, L.A. Eriksson, Editor. 2001, Elsevier. p. 655-690.

162. Parameswaran, S., R. Wang, and G. Hastings, *Calculation of the Vibrational Properties of Chlorophyll a in Solution.* The Journal of Physical Chemistry B, 2008. **112**(44): p. 14056-14062.

163. Breton, J., *Efficient exchange of the primary quinone acceptor Q_A in isolated reaction centers of Rhodopseudomonas viridis.* Proc. Natl. Acad. Sci. USA, 1997. **94**(21): p. 11318-11323.

164. Hadzi, D. and N. Sheppard, *Infra-red absorption spectra and the hydrogen bonding of some chelated hydroxyquinones.* Transactions of the Faraday Society, 1954. **50**(0): p. 911-918.

165. Bloom, H., L.H. Briggs, and B. Cleverley, *33. Physical properties of anthraquinone and its derivatives. Part I. Infrared spectra.* Journal of the Chemical Society (Resumed), 1959(0): p. 178-185.

166. Bellamy, L.J., *The infrared spectra of complex molecules*. 1980, London: Methuen.

167. Sakuragi, Y., et al., *Insertional inactivation of the menG gene, encoding 2-phytyl-1,4-naphthoquinone methyltransferase of Synechocystis sp PCC 6803, results in the incorporation of 2-phytyl-1,4-naphthoquinone into the A(1) site and alteration of the*

equilibrium constant between A(1) and F-x in photosystem I. Biochem., 2002. **41**(1): p. 394-405.

168. Woodbury, N.W., et al., *Radical-pair energetics and decay mechanisms in reaction centers containing anthraquinones, naphthoquinones or benzoquinones in place of ubiquinone.* Biochimica et Biophysica Acta (BBA) - Bioenergetics, 1986. **851**(1): p. 6-22.

169. Feldman, K.S., D.K. Hester Ii, and J.H. Golbeck, *A relationship between amide hydrogen bond strength and quinone reduction potential: Implications for photosystem I and bacterial reaction center quinone function.* Bioorganic & Medicinal Chemistry Letters, 2007. **17**(17): p. 4891-4894.